Summer 8-15-2023

Applications of observational seismology: insights into volcanic and near surface processes

Justin T. Wilgus

Justin T. Wilgus

Candidate

Earth and Planetary Sciences

Department

This dissertation is approved, and it is acceptable in quality and form for publication:

Approved by the Dissertation Committee:

Dr. Brandon Schmandt

Chair

Dr. Adam Ringler

Member

Dr. Karl Karlstrom

Member

Dr. Lindsay Lowe Worthington

Member

Dr. Julien Chaput

Member

APPLICATIONS OF OBSERVATIONAL SEISMOLOGY: INSIGHTS INTO VOLCANIC AND NEAR SURFACE PROCESSES

by

JUSTIN T. WILGUS

B.S. IN GEOLOGY, MINOR IN MATHEMATICS
NORTHERN ARIZONA UNIVERSITY, 2015

M.S., EARTH & PLANETARY SCIENCE
UNIVERSITY OF NEW MEXICO, 2018

DISSERTATION

Submitted in Partial Fulfillment of the
Requirements for the Degree of

Doctor of Philosophy
Earth and Planetary Sciences

The University of New Mexico
Albuquerque, New Mexico

August, 2023

Acknowledgements

I would first like to thank my advisor, Dr. Brandon Schmandt, for giving me this opportunity, and always motivating my progress. I owe a huge thanks to the research scientists at the United States Geological Survey Albuquerque Seismological Laboratory, Dr. Adam Ringler, Dr. Robert Anthony, and Dr. David Wilson for providing me the opportunity to conduct research with their group, and introducing me to new fields of seismology while simultaneously encouraging me to pursue my interests. My time as a graduate student was enriched with numerous intellectually stimulating collaborations. In particular, I am grateful to have had the opportunity to work on projects alongside Dr. Chengxin Jiang, Dr. Ross Maguire, and Dr. Karl Karlstrom. I thank those on my committee not yet named, Dr. Lindsay Lowe Worthington, and Dr. Julien Chaput for providing valuable guidance and support.

I am indebted to the many people who were a part of the seismology group during my time at UNM, particularly, Dr. Chengxin Jiang, Dr. Ross Maguire, Dr. Han Zhang, Dr. Margaret Glasgow, Dr. Evans Onyango, and Collin Brandl for their constant willingness to impart conceptual knowledge and discuss science with rigor. While the focus and approach to science from the aforementioned talented researchers is quite variable, each of them have demonstrated to me what it means to be a scientist and imparted the scientific ethos.

To my family and friends, you have experienced this journey first hand and have trudged with me on this road of happy destiny supporting me throughout, thank you. In particular, I would like to acknowledge my late father, Thomas Wilgus, who provided me

my first mineral collection as a young child and inspired my first contemplations of the natural world. This experience set in motion my trajectory toward becoming an Earth scientist. I acknowledge my mother, Peggy Newby, for nurturing my curiosities and always encouraging my pursuits. I am extremely grateful to my aunt Maureen, for her unconditional support and always believing in me. I am appreciative of my friend and fellow scientist Dr. Tyler Diggans for being an inspiring individual and for long talks during long drives in the midst of our graduate studies. I also owe a big thanks to the BMX community, especially Justin Schwanke and Steve Woodward for being good friends and providing much needed reprieve from the academic grind and scientific pursuits.

Finally, I would like to thank my wonderful wife Kelly, who I could not have undertaken this journey without, for her consistent love and support and for being the best teammate a man can ask for.

-Justin Wilgus

Applications of observational seismology: insights into volcanic and near surface processes

by

Justin T. Wilgus

B.S. in Geology, minor in Mathematics
Northern Arizona University, 2015

M.S., Earth & Planetary Science
University of New Mexico, 2018

Ph.D., Earth & Planetary Sciences, University of New Mexico, 2023

ABSTRACT

The field of observational seismology has made tremendous progress in the past two decades. This progress has been multi-faceted in form, but significant contributions emanated from 1) increases in both the quality and the quantity of seismic data 2) advances in computational power 3) advances in algorithmic capability, including machine learning. In this dissertation I report on three distinctly different seismic applications made possible by the aforementioned progress and discuss the insights these applications have provided in understanding volcanic and near surface processes of the Earth.

In the first chapter titled, *"Shear Velocity Evidence of Upper Crustal Magma Storage Beneath Valles Caldera"* I present the first local Vs tomographic images of the Valles Caldera magmatic system from ambient noise Rayleigh dispersion using a dense

(∼750 m mean spacing) transect (∼71 km length) of nodal seismographs. An ∼6 km wide low-Vs anomaly (Vs < 2.1 km/s) is located at ∼3–10 km depth. Assuming magma in textural equilibrium, the new tomography suggests that melt fractions up to ∼17%–22% may be present within the upper crustal depth range where previously erupted rhyolites were stored. This work was peer reviewed and published in *Geophysical Research Letters* and is available for open access digital download.

In the second chapter titled, *"Seasonality and spatial variability in shallow velocity structure (dv/v) at the Albuquerque Seismic Laboratory using a Repeating Impulsive Source"* I make use of a novel impulsive repeating source to measure shallow velocity structure (d*v/v*) over multiple years and investigate small-scale spatial variability of d*v/v* across a small-aperture (∼500 m) array of high quality posthole seismometers and two deep (90 and 188 m) borehole seismometers at the Albuquerque Seismic Laboratory (ASL). A consistent and clearly resolvable seasonal d*v/v* oscillation with an amplitude of ∼0.2% is broadly present on all ASL borehole and array stations. Through some simple logical deductions, a hydrological source mechanism is determined to be a likely candidate. However, the presence of small-scale spatial variability in d*v/v* indicates measurements are sensitive to structure on the order of 100's of meters. I further demonstrate such sensitivity has the potential to obscure smaller amplitude shorter time scale signals, and highlight the importance of spatiotemporal analysis of d*v/v*. Work from this chapter has been submitted for peer review.

In the third and final chapter titled, "*Background Seismic Noise Levels Among the Caribbean Network and the Role of Station Proximity to Coastline*" I calculate power

spectral density over > 15 years to examine seismic background noise within the 0.05-300 s period range from the nine-station Caribbean seismic network (CU) distributed throughout the Caribbean region. I document wide variability in noise levels among the stations and describe the most discernable first order signals observed. One of the most prominent signals occurs in the 0.75-3 s band where power levels are systematically elevated and decay as a function of proximity to coastline. A simple surface wave amplitude decay model fits the observed decay well with geometric spreading being the most important factor for stations near the coast (< ~ 50 km). Furthermore, this relationship is absent in the 4-8 s range more typical of globally observed secondary microseism. This dichotomy suggests that 0.75–3 s power arises from nearshore wave action and locally overwhelms more distant and spatially distributed secondary microseism generation. Regardless of source, application of this basic model indicates that a power reduction of ~25 dB can be achieved by simply installing the seismometer 25 km away from the coastline. Work from this chapter has also been submitted for peer review.

Table of contents

1 Shear velocity evidence of upper crustal magma storage beneath Valles Caldera

Authors and affiliations

Justin Wilgus[1]*

Brandon Schmandt[1]

Ross Maguire[1,2]

Chengxin Jiang[3]

Julien Chaput[4]

[1]University of New Mexico, Department of Earth & Planetary Sciences, Albuquerque, NM, USA

[2]University of Illinois Urbana-Champaign, Department of Geology, Urbana, IL, USA

[3]The Australian National University, Research School of Earth Sciences, Acton, ACT, Australia

[4]University of Texas at El Paso, Department of Geological Sciences, El Paso, TX, USA

∗Corresponding author

1.1 Abstract

Valles Caldera was formed by large rhyolitic eruptions at ∼1.6 and 1.23 Ma and it hosts post-caldera rhyolitic deposits as young as ∼69 ka, but the contemporary state of the magmatic system is unclear. Local seismicity beneath Valles Caldera is rare and shear-velocity (Vs) structure has not been previously imaged. Here, we present the first local Vs tomography beneath Valles Caldera using ambient noise Rayleigh dispersion from a ∼71 km transect of nodal seismographs with mean spacing of ∼750 m. An ∼6 km wide

low-Vs anomaly (Vs < 2.1 km/s) is located at ~3-10 km depth within the 1.23 Ma caldera's ring fracture. Assuming magma in textural equilibrium, the new tomography suggests that melt fractions up to ~17–22% may be present within the upper crustal depth range where previously erupted rhyolites were stored.

1.2 Introduction

Understanding the current state and evolution of caldera-forming magmatic systems is an important challenge because these systems exhibit diverse life-cycles with a wide variety of hazardous eruptive scenarios (Cashman & Giordano, 2014; Wilson et al., 2021). Valles Caldera was formed by two rhyolitic eruptions that each deposited >300 km^3 dense rock equivalent at ~1.6 and ~1.23 Ma, respectively (Goff et al., 2014; Cook et al., 2016; Wu et al., 2021; Nasholds and Zimmerer, 2022). It is often considered the type example of a resurgent caldera with a central dome, Redondo Peak, that was uplifted within ~54 Kyr of the last caldera-forming eruption and peripheral post-caldera rhyolite flows following the contour of its ring fracture (Figure 1; Smith and Bailey, 1968; Philips et al., 2007; Kennedy et al., 2012). The clarity of its geological record of caldera-forming processes contrasts with the uncertain contemporary state of the underlying magmatic system.

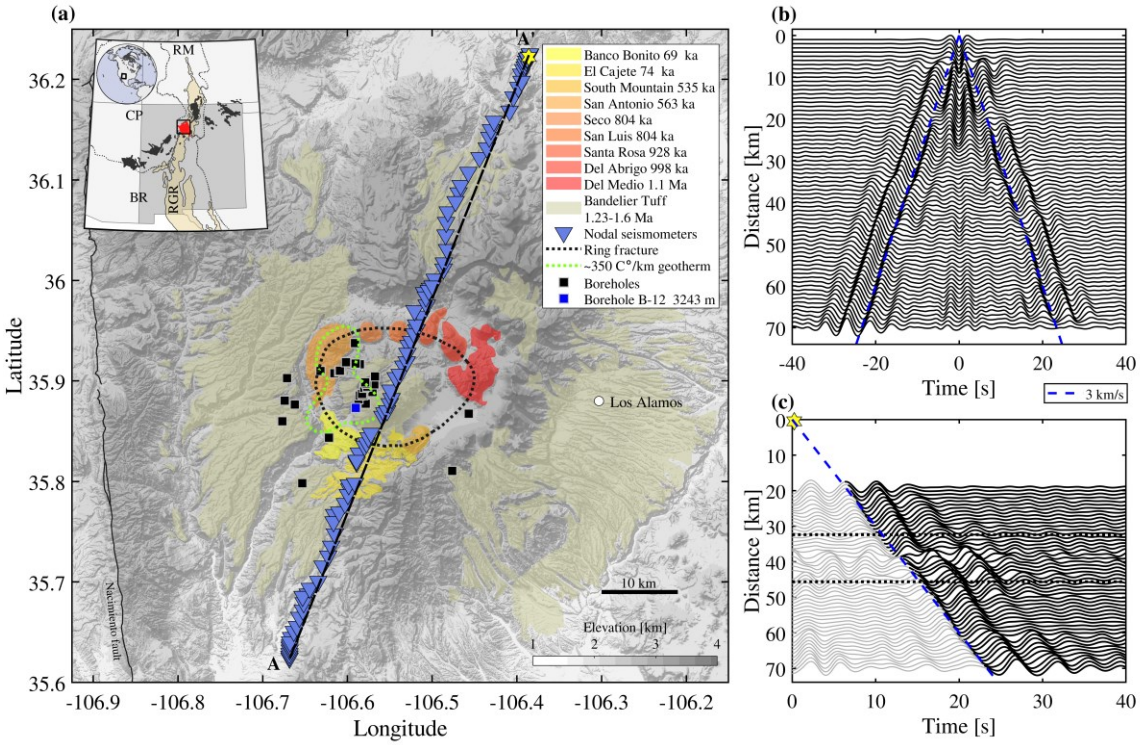

Figure 1. Study area map and example data. a) A topographic map centered on Valles Caldera is shown with semi-transparent fill indicating major rhyolitic outflows colored by time of eruption. Blue triangles are nodal seismographs. A black dotted line shows the surficial trace of the ring fracture from the 1.23 Ma eruption. The green dotted line encloses the area with ≥350° C/km geothermal gradient (Morgan et al., 1996) and squares are borehole locations. Borehole B-12 is the deepest at ~3.2 km (Nielson & Hulen, 1984). A yellow hexagram shows the virtual source used in panel c. Line, A-A', delineates the tomographic cross section. The left inset shows regional physiographic provinces: Colorado Plateau, Basin and Range, Rocky Mountains, and Rio Grande Rift. Semi-transparent tan fill shows the RGR. Solid black fill shows Cenozoic volcanic fields of the Jemez lineament. Solid red fill shows the Jemez volcanic field which includes Valles Caldera and the black square outlines the extent of the main figure. b) Noise cross correlations are shown filtered from 3 to 9 s and stacked at a distance interval of 1 km. c) A virtual source gather is shown using a northern station and 3–5 s bandpass filter. Black dotted lines denote the 1.23 Ma caldera's ring fracture.

Post-caldera volcanism primarily occurred between ~1.23 and 0.5 Ma and the subsequent quiescence was interrupted by eruption of the ~74 ka El Cajete pyroclastic deposits and ~69 ka Banco Bonito rhyolite flow near the southwestern moat of the

caldera (Philips et al., 2007; Zimmerer et al., 2016; Nasholds & Zimmerer, 2022). Petrologic evidence suggests that the Banco Bonito lavas were generated by renewed intrusion of more mafic melt (Wolff & Gardner, 1995). The potential occurrence of more recent magma recharge is unresolved. A lack of contemporary seismicity beneath Valles Caldera may indicate a stable cooling reservoir or primarily ductile deformation due to high crustal temperatures (Sanford et al., 1979; House & Roberts, 2020; Nakai et al., 2017). Boreholes drilled for geothermal exploration and basic science document high geothermal gradients of up to ∼350–450 °C/km just west of the caldera's center (Figure 1; Morgan et al., 1996). Most boreholes within the caldera encountered high-temperature alteration but a dearth of magmatic fluids suggesting a shrinking hydrothermal system (Nielson & Hulen, 1984; Goff & Gardner, 1994). Broader analysis of shallow hydrothermal fluids within and surrounding Valles Caldera indicates ongoing transport of mantle-derived helium consistent with input of mafic melts at depth (Goff & Janik, 2002; Blomgren et al., 2019).

Seismic imaging provides insight into the contemporary abundance of magma in the upper crust beneath Valles Caldera. Early P-wave studies indicated low P-velocity (Vp) and elevated attenuation beneath the caldera (Ankeny et al., 1986; Roberts et al., 1991, 1995). Teleseismic P-wave data from the 1993–1994 Jemez Tomography Experiment (JTEX) enhanced resolution within the caldera and revealed a low-Vp anomaly between ∼5 and 20 km depth in the shape of a vertically elongated ellipsoid with a Vp reduction of −23% (Steck et al., 1998). Following JTEX, there was a long hiatus in data collection for local imaging. Denser arrays and application of newer seismic

methods such as ambient noise surface wave tomography could add valuable S-velocity (Vs) constraints with complementary sensitivity to melt, improve depth-resolution, and better facilitate comparison of Valles Caldera to other systems that may be in a similar life-cycle stage (e.g., Schmandt et al., 2019).

Here, we present the first local Vs tomography beneath Valles Caldera by applying ambient noise Rayleigh wave tomography to data from a new dense seismic transect (Figure 1). Short-period Rayleigh wave dispersion constrains absolute Vs in the middle to upper crust and the mean seismograph spacing of ∼0.75 km provides the ability to recover local variations in structure along the ∼71-km transect. The new Vs tomography results are used to estimate the potential depth interval and concentration of magma beneath Valles Caldera.

1.3 Data and methods

1.3.1 Data

Continuous seismic data were recorded with 97 three-component Magseis-Fairfield nodal seismometers. The stations were deployed along a ∼71 km NNE striking linear transect across Valles Caldera (Figure 1) with a spacing of ∼750 m and operated between 29 September, 2019, and 9 November, 2019. The nodal seismographs were coupled to the ground with stakes but not buried to minimize environmental impact. Ten seismographs tipped during deployment, presumably due to wildlife interactions based on frequent observations of elk and cattle. Three of the tipped stations had >10 days of data that were recovered by identifying the day that inter-station noise correlations abruptly changed. Tipped nodes are noted in Appendix 1.A (Table S1).

1.3.2 Ambient noise correlations

Ambient noise cross-correlation functions were calculated from ambient seismic noise following Bensen et al. (2007). The data were down-sampled to 10 Hz, bandpass filtered from 0.02 to 2 Hz, normalized in the time domain using a running absolute mean, and then whitened before cross-correlation. Correlations were computed for 4-hr half-overlapping time windows throughout the continuous data (e.g., Seats et al., 2012) and then all correlations for each station pair were linearly stacked to preserve phase (Yang et al., 2023). We focus on the vertical-vertical (ZZ) component cross-correlations which show clear fundamental mode Rayleigh waves on the positive and negative lag portions of the symmetric cross correlations (Figure 1b).

1.3.3 Phase velocity dispersion

Phase velocity dispersion curves were calculated using the automated frequency-time analysis (FTAN) method (Levshin et al., 1972; Bensen et al., 2007). We focus on 3–9 s periods that are sensitive to the upper and middle crust (Figure S1 in Appendix 1.A). Below 3 s period clear fundamental mode Rayleigh waves were not observed. Beyond 9 s period the ~71-km long transect provides few measurements with inter-station spacing greater than our minimum of 1.5 wavelengths. To boost the signal-to-noise ratio as well as to reduce the potential effects of inhomogeneous noise source distribution, we averaged the positive and negative portions of the cross-correlation functions. We retained measurements with phase velocities between 1 and 4.6 km/s, signal-to-noise

ratio > 5, and wavelengths > 1.5, resulting in 2,749 total dispersion curves available for phase velocity tomography (Figure S2 in Appendix 1.A).

1.3.4 Phase velocity tomography

A damped least-squares method was used to invert inter-station phase velocity dispersion measurement for phase velocity along the transect for periods between 3 and 9 s (e.g., Wilgus et al., 2020). At 4 s period there are ∼1,300 inter-station phase velocity measurements used for tomography. This number decreases with increasing period as the 1.5 wavelength requirement becomes a larger fraction of array length (Figure S3 in Appendix 1.A). The inversion was conducted with straight rays on a 0.5 km grid along linear transect A-A' shown in Figure 1. To reduce the influence of potential outliers among the dispersion measurements, a two-stage inversion approach was used in which measurements with travel time residuals beyond two standard deviations after the first inversion were removed and then the inversion was repeated (e.g., Wang et al., 2017).

1.3.5 Shear velocity inversion and modelling

Phase velocity dispersion curves from 3 to 9 s period were extracted for 144 locations along the transect to invert for Vs as a function of depth from the surface. We closely followed the workflow of Wilgus et al. (2020) using a Bayesian Markov chain Monte Carlo (BMMC) approach to obtain an ensemble of Vs models capable of fitting the dispersion measurements (Shen et al., 2013). The subsurface Vs structure is represented by a total of 9 parameters, consisting of 7 b-splines for Vs in the middle to upper crust, a depth transition to an underlying half-space at 20–23 km, and Vs in the half-space. To

accommodate potentially strong heterogeneity in the upper crust and diminishing resolution with depth, the prior distribution is wider in the upper crust and narrows with depth (Figure S1 and Table S2 in Appendix 1.A). Phase velocity sensitivity kernels show that 90% of the sensitivity for the longest period Rayleigh wave, 9 s, is located above 21 km depth. Consequently, the parameterization transitions from 7 b-splines to a half-space within a depth range of 20-23 km (Figure S1 in Appendix 1.A). The BMMC inversion explores the model space, iteratively predicting dispersion (p_i), and evaluating the fit to the observed dispersion (d_i) with a reduced Chi-square misfit equation $\chi^2 = n^{-1} \sum_{i=1}^{n} \sigma_i^{-2}(d_i - p_i)^2$, where σ is uncertainty and n is the number of discrete periods. A total of 2 million iterations were used at each point along the transect. The best 2,000 models at each location are used as the posterior distribution and the mean of the ensemble is used for constructing the final Vs profile. All forward calculations of phase velocity were conducted with software from Computer Programs in Seismology (Herrmann, 2013) using empirical crustal rock scaling relationships between Vs, Vp, and density (Brocher, 2005).

Multiple estimates of phase velocity uncertainty were tested in the Vs inversions. We chose to use a fixed value of 25 m/s, which results in a mean Chi-squared misfit of 1.7 (Figure S4 in Appendix 1.A). An alternate approach using bootstrap resampling and repeated phase velocity tomography (e.g., Jiang et al., 2018) resulted in smaller uncertainties and a greater mean χ^2 misfit of 14.8. Results based on different uncertainty choices show that the geometry of major features of the model is stable but small variations in the amplitude of velocity anomalies are present (Figure S5 in

Appendix 1.A). For instance, using the smaller uncertainties from the bootstrap approach results in a slightly lower minimum Vs of ~1.95 km/s rather than ~2.0 km/s.

1.3.6 Teleseismic P-wave relative delay times

The dense spacing of the nodal seismograph array provides an opportunity to observe teleseismic P-wave residual times as a simple metric of consistency with prior P-wave studies and consistency between any major Vp and Vs anomalies. However, the brief deployment did not provide many high-quality events. One of the clearest teleseismic P-waves observed when most nodes were operating is shown in Figure 2. The event occurred in Japan and the P-wave approaches Valles Caldera from the northwest. The seismograms were bandpass filtered from 0.25 to 0.75 Hz and aligned based on travel time predictions for the AK135 velocity model (Kennett et al., 1995). Seismograms with signal-to-noise amplitude ratios < 3 were removed. Relative alignment of the seismograms with multi-channel cross correlation was used to identify Vp anomalies sampled by steeply incident P-waves (VanDecar & Crosson, 1990). Since there is ~1.8 km topographic relief along the transect, we applied elevation corrections assuming an upper crustal Vp of 5.5 km/s based on estimates from controlled source and earthquake travel time tomography (Ankeny et al., 1986).

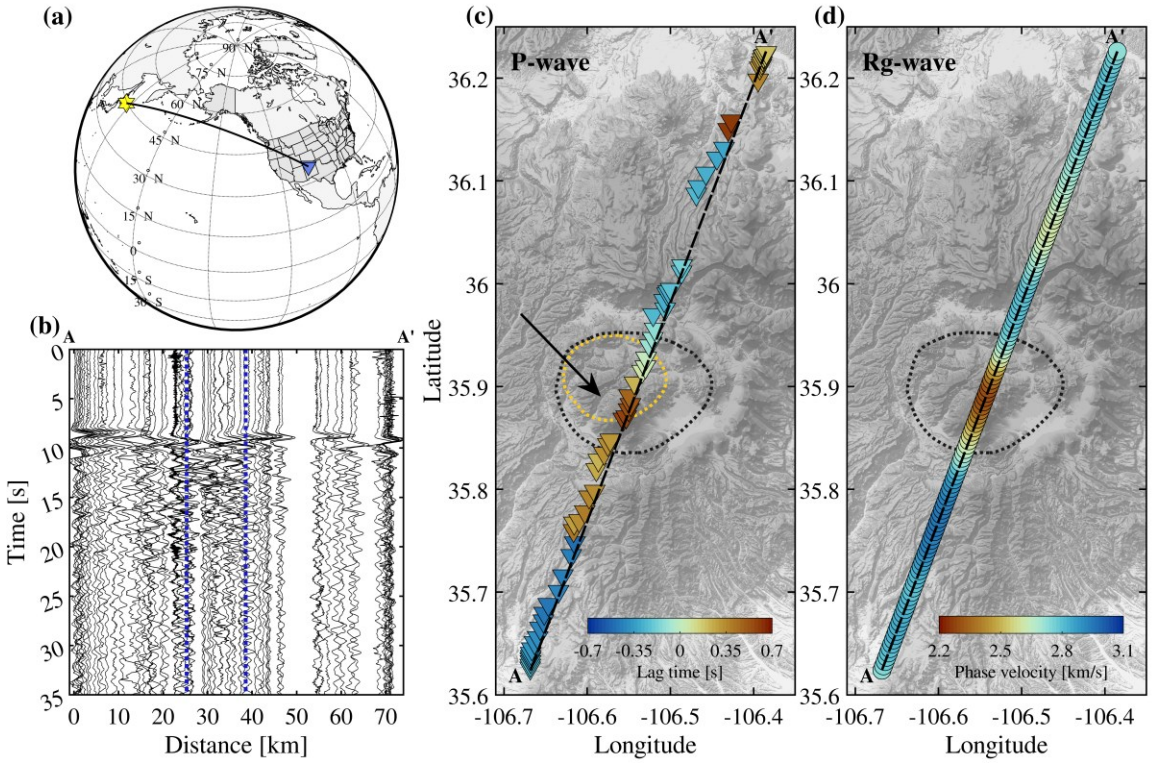

Figure 2. Comparison of teleseismic P-wave lag times and 3–5 s Rayleigh wave phase velocities. a) The map shows the M5.7 earthquake location (yellow hexagram) and the Valles transect (blue triangle). b) Waveforms are shown across the Valles transect (A-A') filtered from 0.25 to 0.75 Hz. Blue dotted lines denote the 1.23 Ma ring fracture. c) P-wave lag times corrected for topography. A black arrow corresponds to the incoming azimuth of the P-wave. Orange dotted line encloses Vp anomaly <–10% at 7.5 km depth (Steck et al., 1998). Missing nodes were either not recording during the event or had signal-to-noise amplitude ratios <3. d) Period averaged (3–5 s) phase velocity is plotted along A-A'.

1.4 Results

1.4.1 Phase velocity pseudo cross-section

The depth of peak sensitivity for Rayleigh wave phase velocity increases with period such that plotting the phase velocities beneath each point along the transect provides a pseudo cross-section perspective on local crustal structure (Figure 3b). The most prominent feature of the pseudo cross-section is a low-velocity anomaly for periods between ~3 and 5 s beneath the Redondo Peak resurgent dome, with the lowest

velocity found for ∼4 s period (Figures 2d and 3c). Beneath the central caldera across a width of ∼6–8 km within ring fracture, 3–5 s phase velocities are ∼12%–15% lower than the array mean, ∼2.3–2.4 km/s (Figure 2d and 3c). The magnitude of the low-velocity anomaly makes it visible in virtual source gathers of noise correlations as a deflection in the Rayleigh wave arrival as it crosses the central caldera within the ring fracture (Figure 1c). Phase velocity tomography resolution tests demonstrate that a prominent low-velocity anomaly within the caldera's ring fracture is resolvable with the available data coverage, but the magnitude of the velocity anomaly would be slightly underestimated (Figures S6 and S7 in Appendix 1.A). A test with an input anomaly of −20% in phase velocity across a 6 km width resulted in a recovered minimum velocity of −17.5% (Figure S6 in Appendix 1.A). Other phase velocity features include low velocities (∼2.5 km/s) at 3–4 s period on the northern flank of the caldera (∼45–55 km transect distance) and high velocities (∼3.1 km/s) at 3–4.5 s on the southern flank of the caldera (∼15–23 km transect distance; Figure 3b).

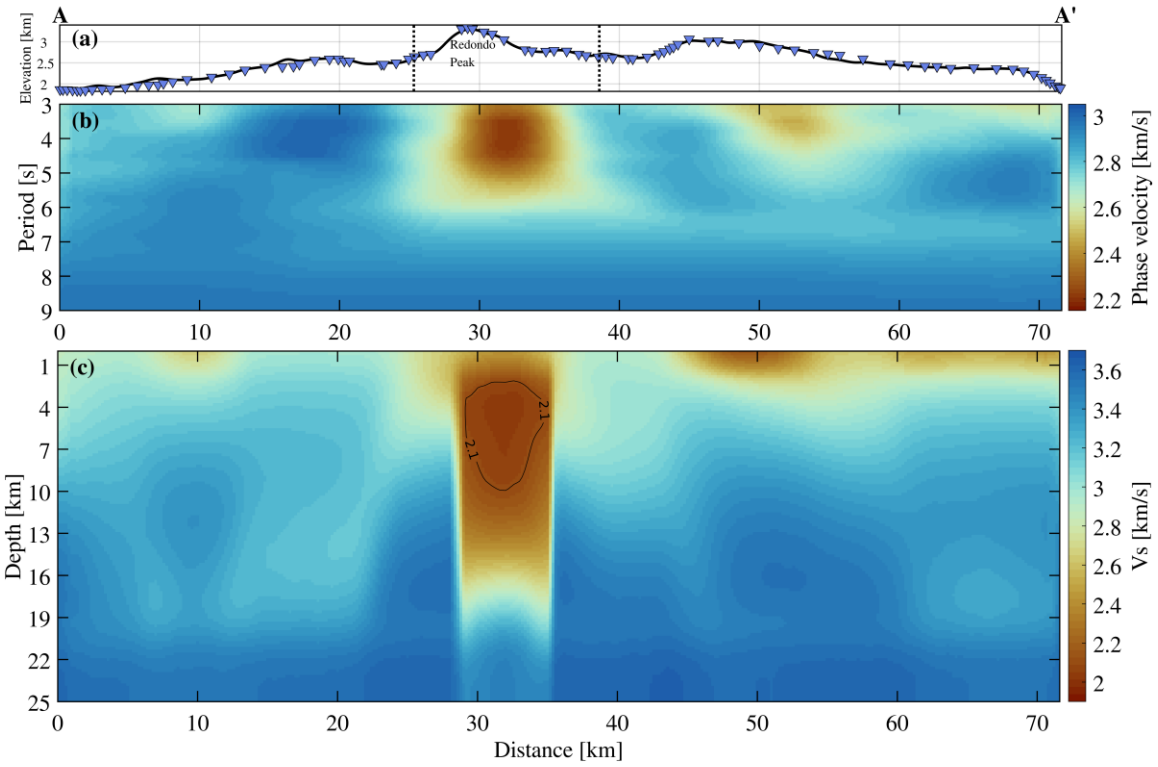

Figure 3. Tomographic cross-sectional (A-A') images of Valles Caldera. a) Smoothed topography along A-A' with 3x vertical exaggeration. Redondo Peak (labeled) is the highest elevation point of the resurgent dome. Blue triangles are seismograph locations and dotted lines show locations of the 1.23 Ma ring fracture associated with eruption of the upper Bandelier tuff (Tshirege member). b) Phase velocity as a function of period (3–9 s) is shown along the transect. c) Shear velocity is shown as a function of distance along the transect and depth beneath the surface with no vertical exaggeration.

1.4.2 Shear velocity cross-section

Inversion for Vs provides constraints on absolute Vs as a function of depth. Extremely low Vs (< 2.1 km/s) is found from ~3-10 km depth across a width of ~6 km within the 1.23 Ma caldera's ring fracture (Figure 3c). The low-velocity anomaly within the Vs < 2.1 km/s contour corresponds to an ~32% Vs reduction compared to the mean across the array. The anomaly's location under the Redondo Peak resurgent dome is slightly offset from the area of highest geothermal gradients, however most boreholes were drilled on

the west side of Redondo Peak, whereas the nodal array crossed closer to the center of the dome (Figure 1). The highest χ^2 misfit values (>4) are situated on either side of the low-Vs anomaly (Figure S4 in Appendix 1.A), suggesting that phase velocities near the edges of the anomaly are difficult to fit with locally 1D velocity structure. Aside from the low-velocity anomaly beneath Redondo Peak, there is a low-velocity anomaly with Vs of ∼2.2–2.5 km/s on the northern flank of the caldera (transect distance of ∼45–55 km), but unlike the central caldera anomaly its depth extent is restricted to the uppermost ∼2 km (Figure 3c, Figure S8 in Appendix 1.A).

1.4.3 Teleseismic P-wave lag times

P-wave travel time lags of up to ±0.65 s were measured for a clearly recorded teleseismic earthquake (Figure 2c). A deflection in the P-wave arrival can be seen in the waveforms recorded within the caldera's ring fracture (Figure 2b). Delayed arrivals, indicative of low Vp at depth, are located on the Redondo Peak resurgent dome within the Valles Caldera ring fracture (Figure 2b). The location of the most delayed arrivals is consistent with previous P-wave studies that used seismographs with larger inter-station spacing but distributed over the area of the caldera rather than in one transect (Roberts et al., 1991; Steck et al., 1998). The along-transect distance of the most delayed arrivals, ∼0.5–0.65 s, coincides with the area of highest geothermal gradients (Morgan et al., 1996). More moderate lag times of ∼0.3 s extend south from Redondo Peak to ∼10 km beyond the southern edge of the caldera (Figure 2c). The broad width of the ∼0.3 s delays is consistent with a deeper origin located west of the nodal transect based on the ∼315° back-azimuth of this event (Figure 2c).

1.5 Discussion

The new Rayleigh wave tomography advances insights into local Vs structure within and surrounding Valles Caldera. The primary result is strongly reduced Vs beneath the resurgent dome, Redondo Peak. A secondary low-Vs anomaly, ∼2.2–2.5 km/s, located in the uppermost 2 km on the northern flank of the caldera is more likely related to the history of volcanic deposition in the area (Figure 3c). Beginning in the mid-Miocene there was intermediate-to-mafic volcanic activity on the north side of the caldera and the resulting extrusive rock deposits may cause lower Vs in the uppermost crust that contrasts with the southern flank of the caldera (Gardner et al., 1986; Goff et al., 2011). The central caldera low-Vs anomaly and its potential implications for the contemporary state of the magmatic system are the focus for the remainder of the discussion.

Within the caldera the lowest Vs volume is concentrated between ∼3 and 10 km depth over a width of ∼6 km within the 1.23 Ma ring fracture, where Vs is ∼2.0–2.1 km/s (Figure 3c). The relative Vs anomaly within that volume is −32%. Prior teleseismic P-wave tomography estimated a relative velocity anomaly of −23% within a more vertically-elongated ellipsoidal anomaly (Steck et al., 1998). Reflectors previously identified by P-wave coda migration at ∼4 km and ∼9−14 km below the surface may represent the vertical boundaries of the magma reservoir, but the upper reflector may alternatively be related to the contact between tuff deposits and the underlying basement rock (Aprea et al., 2002). The availability of absolute Vs in the upper to middle crust from this study provides valuable new constraints for estimating the origin of the

low-velocity anomaly. Given the Vs anomaly's location under the resurgent dome and that its minimum velocities are located between ~3 and 10 km depth, it cannot be explained by unconsolidated caldera fill. The depth range of the anomaly overlaps petrologically estimated storage depths of erupted rhyolites, ~2.5–9 km (Spell & Kyle, 1989; Wilcock et al., 2013; Boro et al., 2020). So, we proceed to interpret silicate partial melt and magmatic volatiles as probable contributors to the low-velocity anomaly.

We first consider a base scenario in which melt fraction is estimated assuming a composition like that of the ~69 ka Banco Bonito rhyolite flow (Table S3 in Appendix 1.A) and that partial melt in the subsurface today is in textural equilibrium. Then we proceed to discuss uncertainties that could lead to over- or under-estimation of the melt fraction. To predict Vs as a function of the melt fraction, we used the theoretical model of Berryman (1980) for an elastic medium with ellipsoidal fluid inclusions (e.g., Paulatto et al., 2019). Elastic properties of the solid were calculated with Perple_X assuming bulk composition of the Banco Bonito rhyolite, pressure of 170 MPa (~5 km depth), and a temperature of 700°C (Connolly, 2009). The velocity reduction due to partial melt depends on the assumed aspect ratio of intergranular melt pockets and aspect ratios of ~0.1–0.15 are expected for textural equilibrium (Takei, 2002). In this scenario, Vs of 2–2.1 km/s would correspond to melt fractions of 17%–22% (Figure S9 in Appendix 1.A). We consider textural equilibrium a reasonable assumption because the system has not erupted since ~69 ka and it hosts little seismicity, so any deformation and magmatic recharge are expected to be slowly evolving processes.

Uncertainties in seismic imaging and the multi-phase structure of the magma reservoir could bias the estimated melt fractions. This study benefits from a dense local array, but simplifying assumptions include a 2D phase velocity inversion and straight ray paths. Resolution tests using these assumptions indicate that ∼85% of the input velocity anomaly amplitude could be recovered for a low-velocity anomaly like that imaged beneath Redondo Peak (Figures S6 and S7 in Appendix 1.A). A surface wave tomography resolution study using 3D synthetic waveforms (e.g., Maguire et al., 2022a) would provide a more realistic assessment but it is not considered feasible within the scope of this study. Insights from 3-D full wave synthetic tests conducted by Maguire et al. (2022a) suggest that conventional surface wave travel time tomography is likely to underestimate the true magnitude of Vs reduction in crustal magma reservoirs, but the problem is more subdued for magma reservoirs that are large with respect to the inter-station spacing. In this study, the velocity anomaly of interest is ∼6 km wide in the upper crust and the mean inter-station spacing is <1 km so we do not expect severe underestimation.

If the seismic properties are influenced by magmatic volatiles that could bias our interpretation of the melt-fraction toward over-estimation. Valles magmas may have several percent dissolved volatiles based on past eruptions (Boro et al., 2020; Waelkens et al., 2022). As magma cools in the upper crust buoyant volatiles may accumulate in a thin low-velocity layer atop the magma reservoir (e.g., Seccia et al., 2011). Such a scenario is plausible at Valles Caldera given that boreholes encountered high geothermal gradients up to 3.2 km deep (Figure 1) but did not reach magmatic fluids or

recently cooled intrusions (Nielson & Hulen, 1984; Goff & Gardner, 1994), so some volatiles could be trapped beneath a low-permeability boundary (De Siena et al., 2017; Vanorio et al., 2005). Resolution of a potential layer of magmatic volatiles atop a silicate melt reservoir may be possible with higher frequency Vp/Vs imaging, such as that conducted at Campi Flegrei, because lower Vp/Vs is expected for a trapped volume of exsolved volatiles compared to silicate melt (Calò & Tramelli, 2018; Chiarabba & Moretti, 2006). However, the paucity of seismicity beneath Valles Caldera hinders the ability to conduct similar imaging. Comparison of teleseismic P-wave tomography and Rayleigh tomography is complicated by differing resolution, but the existing results do not suggest a low Vp/Vs anomaly since the Vs reduction (−32%) is greater than the Vp reduction (−23%) reported by Steck et al. (1998). A dominant role for exsolved volatiles in creating the low-velocity anomaly further seems unlikely because the high geothermal gradients in Valles Caldera are consistent with continued presence of melt (Nielsen & Hulen, 1984; Morgan et al., 1996).

Comparison of the Vs structure beneath Valles Caldera to that of other active silicic volcanic fields suggests an active magmatic system. The Laguna del Maule volcanic complex, which has hosted many Holocene rhyolite eruptions, exhibits similar Vs characteristics with a minimum Vs of ∼2.0 km/s at ∼4 km depth based on ambient noise Rayleigh wave tomography (Wespestad et al., 2019). Beneath Yellowstone Caldera the minimum Vs of ∼2.15 km/s at ∼3–8 km depth is comparable to Valles Caldera (Maguire et al., 2022b), but the width of Yellowstone's upper crustal anomaly is up to ∼60 km in comparison to the ∼6 km width imaged here. Long Valley Caldera's seismically imaged

reservoir appears deeper with a top at ~8 km and an underlying Vs anomaly extending to ~20 km depth with a minimum Vs of ~2.5 km/s (Flinders et al., 2018; Nakata & Shelly, 2018). Valles Caldera's Vs structure is more like the examples of Laguna del Maule and Yellowstone where the depth interval of the low-Vs anomaly largely overlaps typical pre-eruptive rhyolite storage depths of ~4–10 km (Bachmann & Bergantz, 2008). Given the 2D geometry of our study we refrain from detailed estimates of the 3D volume of magma beneath Valles Caldera, but a simple approximation of a cylindrical volume with radius of 3 km and depth interval of 7 km would enclose most of the low-Vs anomaly. An ~20% melt fraction within the cylinder would correspond to ~40 km^3 of magma. Only a fraction of this volume (~10%–25%, e.g., Annen et al., 2008) would need to be mobilized to fuel eruptions analogous to those that produced the ~4 km^3 El Cajete pyroclastic deposits from ~74 ka or the ~6.8 km^3 Banco Bonito rhyolite flow from ~69 ka (Wolff et al., 2011; Zimmerer et al., 2016; Nasholds & Zimmerer, 2022).

Evidence for upper crustal magma storage beneath Valles Caldera highlights challenges for hazard monitoring and research. Regional scale geophysical studies show that seismicity is locally absent beneath Valles Caldera (Nakai et al., 2017) and the adjacent Rio Grande Rift deforms slowly with an extension rate of ~0.1 mm/year (Berglund et al., 2012). Unlike similar settings in the United States such as Yellowstone Caldera or Long Valley Caldera, Valles Caldera does not have continuous open-access seismic or ground-based geodetic data. There is a local seismic network concentrated on the eastern flank of the caldera operated by Los Alamos National Laboratory (House & Roberts, 2020), but the data are not openly available and more spatially balanced

coverage would be advantageous for detecting microseismicity beneath the caldera. Additionally, due to the lack of ground-based geodetic instruments, it is unclear whether the apparent lack of seismogenic deformation at Valles Caldera is accompanied by slower or ductile strain.

1.6 Conclusion

We have conducted the first local Vs tomography beneath Valles Caldera using ambient noise Rayleigh tomography with a dense linear array. A prominent low-Vs anomaly is focused within the 1.23 Ma caldera's ring fracture. It exhibits a Vs reduction of ∼32% and absolute Vs of ∼2–2.1 km/s at depths of ∼3–10 km coinciding with the depths of rhyolite storage for past eruptions. The upper crustal Vs reductions in the magma reservoir beneath Valles Caldera are similar or more severe than those at systems with more abundant evidence of seismicity or surface deformation. Our results indicate the potential importance of improved hazard monitoring capacity at Valles Caldera and, more generally, affirm that even seismically quiescent volcanic fields should be regarded as potential hosts of magma in the upper crust.

1.7 Acknowledgements

We acknowledge that the data for this research were collected on the unceded indigenous lands of the Pueblo and Ute peoples. We also acknowledge Santa Fe National Forest and Valles Caldera National Preserve, especially Research Coordinator Robert Parmenter, for facilitating land access for seismic data collection. Field workers are thanked for their efforts in collecting quality data. Fraser Goff, Peter Roberts, and Tobias Fischer engaged in helpful discussions throughout the study. This manuscript also benefited from helpful reviews by Luca De Siena and Arne Spang. This research was supported by NSF Grants EAR-2113315 (B. Schmandt) and EAR-2113367 (J. Chaput). Some of the seismic equipment used in the study was provided by the IRIS PASSCAL Instrument Center and all the raw seismic data are archived at the IRIS Data Management Center; both facilities are supported through the Seismological Facilities for the Advancement of Geoscience (SAGE) Award of the NSF under Cooperative Support Agreement EAR-1851048.

1.8 Data and resources

The ambient noise cross-correlation functions and inter-station phase velocities used for the tomography are openly archived (https://zenodo.org/record/7466411). The raw seismic data for network 4E in 2019 are openly available from the IRIS Data Management Center (Schmandt, 2019; https://doi.org/10.7914/SN/4E_2019).

References

Ankeny, L. A., Braile, L. W., & Olsen, K. H. (1986). Upper crustal structure beneath the Jemez Mountains volcanic field, New Mexico, determined by three-dimensional simultaneous inversion of seismic refraction and earthquake data. Journal of Geophysical Research: Solid Earth, 91(B6), 6188-6198. https://doi.org/10.1029/JB091iB06p06188

Annen, C., Pichavant, M., Bachmann, O., & Burgisser, A. (2008). Conditions for the growth of a longlived shallow crustal magma chamber below Mount Pelee volcano (Martinique, Lesser Antilles Arc). *Journal of Geophysical Research: Solid Earth*, *113*(B7). https://doi.org/10.1029/2007JB005049

Aprea, C. M., Hildebrand, S., Fehler, M., Steck, L., Baldridge, W. S., Roberts, P., ... & Lutter, W. J. (2002). Three-dimensional Kirchhoff migration: Imaging of the Jemez volcanic field using teleseismic data. Journal of Geophysical Research: Solid Earth, 107(B10), ESE-11. https://doi.org/10.1029/2000JB000097

Bachmann, O., & Bergantz, G. (2008). The magma reservoirs that feed supereruptions. *Elements*, *4*(1), 17-21. https://doi.org/10.2113/GSELEMENTS.4.1.17

Bensen, G. D., Ritzwoller, M. H., Barmin, M. P., Levshin, A. L., Lin, F., Moschetti, M. P., Shapiro, N.M., & Yang, Y. (2007). Processing seismic ambient noise data to obtain reliable broad-band surface wave dispersion measurements. Geophysical Journal International, 169(3), 1239-1260. https://doi.org/10.1111/j.1365-246X.2007.03374.x

Berglund, H. T., Sheehan, A. F., Murray, M. H., Roy, M., Lowry, A. R., Nerem, R. S., & Blume, F. (2012). Distributed deformation across the Rio Grande rift, Great Plains, and Colorado Plateau. Geology, 40(1), 23-26. https://doi.org/10.1130/G32418.1

Berryman, J. G. (1980). Long-wavelength propagation in composite elastic media II. Ellipsoidal inclusions. *The Journal of the Acoustical Society of America*, *68*(6), 1820-1831. https://doi.org/10.1121/1.385172

Blomgren, V. J., Crossey, L. J., Karlstrom, K. E., Fischer, T. P., & Darrah, T. H. (2019). Hot spring hydrochemistry of the Rio Grande rift in northern New Mexico reveals a distal geochemical connection between Valles Caldera and Ojo Caliente. *Journal of Volcanology and Geothermal Research*, *387*, 106663. https://doi.org/10.1016/j.jvolgeores.2019.106663

Boro, J. R., Wolff, J. A., & Neill, O. K. (2020). Anatomy of a recharge magma: Hornblende dacite pumice from the rhyolitic Tshirege Member of the Bandelier Tuff, Valles Caldera, New Mexico, USA. *Contributions to Mineralogy and Petrology*, *175*(10), 1-26. https://doi.org/10.1007/s00410-020-01725-w

Brocher, T. M. (2005). Empirical relations between elastic wavespeeds and density in the Earth's crust. Bulletin of the seismological Society of America, 95(6), 2081-2092. https://doi.org/10.1785/0120050077

Calò, M., & Tramelli, A. (2018). Anatomy of the Campi Flegrei caldera using enhanced seismic tomography models. *Scientific reports*, *8*(1), 1-12. https://doi.org/10.1038/s41598-018-34456-x

Cashman, K. V., & Giordano, G. (2014). Calderas and magma reservoirs. *Journal of Volcanology and Geothermal Research*, *288*, 28-45. https://doi.org/10.1016/j.jvolgeores.2014.09.007

Chiarabba, C., & Moretti, M. (2006). An insight into the unrest phenomena at the Campi Flegrei caldera from Vp and Vp/Vs tomography. *Terra Nova*, *18*(6), 373-379. https://doi.org/10.1111/j.1365-3121.2006.00701.x

Connolly, J. A. D. "The Geodynamic Equation of State: What and How." *Geochemistry, Geophysics, Geosystems* 10, no. 10 (2009). https://doi.org/10.1029/2009GC002540.

Cook, G. W., Wolff, J. A., & Self, S. (2016). Estimating the eruptive volume of a large pyroclastic body: the Otowi Member of the Bandelier Tuff, Valles caldera, New Mexico. *Bulletin of Volcanology*, *78*(2), 1-11. https://doi.org/10.1007/s00445-016-1000-0

De Siena, L., Chiodini, G., Vilardo, G., Del Pezzo, E., Castellano, M., Colombelli, S., ... & Ventura, G. (2017). Source and dynamics of a volcanic caldera unrest: Campi Flegrei, 1983–84. Scientific reports, 7(1), 1-13. https://doi.org/10.1038/s41598-017-08192-7

Flinders, A.F., Shelly, D.R., Dawson, P.B., Hill, D.P., Tripoli, B., Shen, Y., 2018. Seismic evidence for significant melt beneath the Long Valley Caldera, California, USA. Geology 46 (9), 799–802. https://doi.org/10.1130/G45094.1

Gardner, J. N., Goff, F., Garcia, S., & Hagan, R. C. (1986). Stratigraphic relations and lithologic variations in the Jemez volcanic field, New Mexico. Journal of Geophysical Research: Solid Earth, 91(B2), 1763-1778. https://doi.org/10.1029/JB091iB02p01763

Goff, F., & Gardner, J. N. (1994). Evolution of a mineralized geothermal system, Valles Caldera, New Mexico. *Economic Geology*, *89*(8), 1803-1832. https://doi.org/10.2113/gsecongeo.89.8.1803

Goff, F., Gardner, J. N., Reneau, S. L., Kelley, S. A., Kempter, K. A., & Lawrence, J. R. (2011). Geologic map of the Valles caldera, Jemez Mountains, New Mexico. New Mexico Bureau of Geology and Mineral Resources Geologic Map, 79(scale 1), 50. [Scholar]

Goff, F., & Janik, C. J. (2002). Gas geochemistry of the Valles caldera region, New Mexico and comparisons with gases at Yellowstone, Long Valley and other geothermal systems. *Journal of volcanology and geothermal research*, *116*(3-4), 299-323. https://doi.org/10.1016/S0377-0273(02)00222-6

Goff, F., Warren, R. G., Goff, C. J., & Dunbar, N. (2014). Eruption of reverse-zoned upper Tshirege member, Bandelier Tuff from centralized vents within Valles caldera, New Mexico. Journal of Volcanology and Geothermal Research, 276, 82– 104. https://doi.org/10.1016/j.jvolgeores.2014.02.018

Herrmann, R. B. (2013). Computer programs in seismology: An evolving tool for instruction and research. Seismological Research Letters, 84(6), 1081– 1088. https://doi.org/10.1785/0220110096

House, L., & Roberts, P. (2020). Seismicity Monitoring in North-Central New Mexico by the Los Alamos Seismic Network. Seismological Research Letters, 91(2A), 593-600. https://doi.org/10.1785/0220190208

Jiang, C., Schmandt, B., Farrell, J., Lin, F. C., & Ward, K. M. (2018). Seismically anisotropic magma reservoirs underlying silicic calderas. *Geology*, *46*(8), 727-730. https://doi.org/10.1130/G45104.1

Kennedy, B., Wilcock, J., & Stix, J. (2012). Caldera resurgence during magma replenishment and rejuvenation at Valles and Lake City calderas. *Bulletin of volcanology*, *74*(8), 1833-1847. https://doi.org/10.1007/s00445-012-0641-x

Kennett, B. L., Engdahl, E. R., & Buland, R. (1995). Constraints on seismic velocities in the Earth from traveltimes. *Geophysical Journal International*, *122*(1), 108-124. https://doi.org/10.1111/j.1365-246X.1995.tb03540.x

Levshin, A. L., Pisarenko, V. F., & Pogrebinsky, G. A. (1972). On a frequency-time analysis of oscillations. In Annales de geophysique (Vol. 28, pp. 211– 218). Centre National de la Recherche Scientifique. Retrieved from https://oceanrep.geomar.de/id/eprint/46865

Maguire, R., Schmandt, B., Chen, M., Jiang, C., Li, J., & Wilgus, J. (2022a). Resolving continental magma reservoirs with 3D surface wave tomography. Geochemistry, Geophysics, Geosystems, e2022GC010446.https://doi.org/10.1029/2022GC010446

Maguire, R., Schmandt, B., Li, J., Jiang, C., Li, G., Wilgus, J., & Chen, M. (2022b). Magma accumulation at depths of prior rhyolite storage beneath Yellowstone Caldera. Science, 378(6623), 1001-1004. https://doi.org/10.1126/science.ade0347

Morgan, P. A. U. L., Sass, J. H., & Jacobsen, R. (1996). Heat flow in VC-2A and VC-2B, and constraints on the thermal regime of the Valles caldera, New Mexico. [Scholar]

Nakai, J. S., Sheehan, A. F., & Bilek, S. L. (2017). Seismicity of the rocky mountains and Rio Grande Rift from the EarthScope transportable array and CREST temporary seismic networks, 2008–2010. Journal of Geophysical Research: Solid Earth, 122(3), 2173– 2192. https://doi.org/10.1002/2016JB013389

Nakata, N., & Shelly, D. R. (2018). Imaging a crustal low-velocity layer using reflected seismic waves from the 2014 earthquake swarm at Long Valley Caldera, California: The magmatic system roof? *Geophysical Research Letters*, *45*(8), 3481-3488. https://doi.org/10.1029/2018GL077260

Nasholds, M. W., & Zimmerer, M. J. (2022). High-precision 40Ar/39Ar geochronology and volumetric investigation of volcanism and resurgence following eruption of the Tshirege Member, Bandelier Tuff, at the Valles caldera. *Journal of Volcanology and Geothermal Research*, *431*, 107624. https://doi.org/10.1016/j.jvolgeores.2022.107624

Nielson, D. L., & Hulen, J. B. (1984). Internal geology and evolution of the Redondo dome, Valles caldera, New Mexico. Journal of Geophysical Research: Solid Earth, 89(B10), 8695-8711. https://doi.org/10.1029/JB089iB10p08695

Paulatto, M., Moorkamp, M., Hautmann, S., Hooft, E., Morgan, J. V., & Sparks, R. S. J. (2019). Vertically extensive magma reservoir revealed from joint inversion and quantitative interpretation of seismic and gravity data. *Journal of Geophysical Research: Solid Earth*, *124*(11), 11170-11191. https://doi.org/10.1029/2019JB018476

Phillips, E. H., Goff, F., Kyle, P. R., McIntosh, W. C., Dunbar, N. W., & Gardner, J. N. (2007). The 40Ar/39Ar age constraints on the duration of resurgence at the Valles caldera, New Mexico. *Journal of Geophysical Research: Solid Earth*, *112*(B8). https://doi.org/10.1029/2006JB004511

Roberts, P. M., Aki, K., & Fehler, M. C. (1991). A low-velocity zone in the basement beneath the Valles Caldera, New Mexico. Journal of Geophysical Research: Solid Earth, 96(B13), 21583-21596. https://doi.org/10.1029/91JB02048

Roberts, P. M., Aki, K., & Fehler, M. C. (1995). A shallow attenuating anomaly inside the ring fracture of the Valles Caldera, New Mexico. Journal of volcanology and geothermal research, 67(1-3), 79-99.https://doi.org/10.1016/0377-0273(94)00100-U

Sanford, A. R., Olsen, K. H., & Jaksha, L. H. (1979). Seismicity of the Rio Grande rift. Rio Grande Rift: Tectonics and Magmatism, 14, 145-168. https://doi.org/10.1029/SP014p0145

Schmandt, B. (2019). Valles 3C node transect [Dataset]. International Federation of Digital Seismograph Networks. https://doi.org/10.7914/SN/4E_2019

Schmandt, B., Jiang, C., & Farrell, J. (2019). Seismic perspectives from the western US on magma reservoirs underlying large silicic calderas. Journal of Volcanology and Geothermal Research, 384, 158-178. https://doi.org/10.1016/j.jvolgeores.2019.07.015

Seats, K. J., Lawrence, J. F., & Prieto, G. A. (2012). Improved ambient noise correlation functions using Welch' s method. *Geophysical Journal International*, *188*(2), 513-523. https://doi.org/10.1111/j.1365-246X.2011.05263.x

Seccia, D., Chiarabba, C., De Gori, P., Bianchi, I., & Hill, D. P. (2011). Evidence for the contemporary magmatic system beneath Long Valley Caldera from local earthquake tomography and receiver function analysis. *Journal of Geophysical Research: Solid Earth*, *116*(B12). https://doi.org/10.1029/2011JB008471

Shen, W., Ritzwoller, M. H., Schulte-Pelkum, V., & Lin, F. C. (2013). Joint inversion of surface wave dispersion and receiver functions: a Bayesian Monte-Carlo approach. *Geophysical Journal International*, *192*(2), 807-836. https://doi.org/10.1093/gji/ggs050

Smith, R. L., & Bailey, R. A. (1968). Resurgent cauldrons. https://doi.org/10.1130/MEM116-p613

Spell, T. L., & Kyle, P. R. (1989). Petrogenesis of Valle Grande Member rhyolites, Valles Caldera, New Mexico: Implications for evolution of the Jemez Mountains

Magmatic System. *Journal of Geophysical Research: Solid Earth*, *94*(B8), 10379-10396. https://doi.org/10.1029/JB094iB08p10379

Steck, L. K., Thurber, C. H., Fehler, M. C., Lutter, W. J., Roberts, P. M., Baldridge, W. S., ... & Sessions, R. (1998). Crust and upper mantle P wave velocity structure beneath Valles caldera, New Mexico: results from the Jemez teleseismic tomography experiment. Journal of Geophysical Research: Solid Earth, 103(B10), 24301-24320. https://doi.org/10.1029/98JB00750

Takei, Y. (2002). Effect of pore geometry on VP/VS: From equilibrium geometry to crack. *Journal of Geophysical Research: Solid Earth*, *107*(B2), ECV-6. https://doi.org/10.1029/2001JB000522

VanDecar, J. C., & Crosson, R. S. (1990). Determination of teleseismic relative phase arrival times using multi-channel cross-correlation and least squares. *Bulletin of the Seismological Society of America*, *80*(1), 150-169. https://doi.org/10.1785/BSSA0800010150

Vanorio, T., Virieux, J., Capuano, P., & Russo, G. (2005). Three-dimensional seismic tomography from P wave and S wave microearthquake travel times and rock physics characterization of the Campi Flegrei Caldera. *Journal of Geophysical Research: Solid Earth*, *110*(B3). https://doi.org/10.1029/2004JB003102

Waelkens, C. M., Stix, J., Eves, E., Gonzalez, C., & Martineau, D. (2022). H2O and CO2 evolution in the Bandelier Tuff sequence reveals multiple and discrete magma replenishments. *Contributions to Mineralogy and Petrology*, *177*(1), 1-23. https://doi.org/10.1007/s00410-021-01866-6

Wang, Y., Lin, F. C., Schmandt, B., & Farrell, J. (2017). Ambient noise tomography across Mount St. Helens using a dense seismic array. Journal of Geophysical Research: Solid Earth, 122(6), 4492-4508. https://doi.org/10.1002/2016JB013769

Wespestad, C. E., Thurber, C. H., Andersen, N. L., Singer, B. S., Cardona, C., Zeng, X., et al. (2019). Magma reservoir below Laguna del Maule volcanic field, Chile, imaged with surface-wave tomography. Journal of Geophysical Research: Solid Earth, 124(3), 2858– 2872. https://doi.org/10.1029/2018JB016485

Wilcock, J., Goff, F., Minarik, W. G., & Stix, J. (2013). Magmatic recharge during the formation and resurgence of the Valles Caldera, New Mexico, USA: evidence from quartz compositional zoning and geothermometry. *Journal of Petrology*, *54*(4), 635-664. https://doi.org/10.1093/petrology/egs078

Wilgus, J., Jiang, C., & Schmandt, B. (2020). A middle crustal channel of radial anisotropy beneath the northeastern Basin and range. *Tectonics*, *39*(7), e2020TC006140. https://doi.org/10.1029/2020TC006140

Wilson, C. J., Cooper, G. F., Chamberlain, K. J., Barker, S. J., Myers, M. L., Illsley-Kemp, F., & Farrell, J. (2021). No single model for supersized eruptions and their magma bodies. Nature Reviews Earth & Environment, 2(9), 610-627. https://doi.org/10.1038/s43017-021-00191-7

Wolff, J. A., Brunstad, K. A., & Gardner, J. N. (2011). Reconstruction of the most recent volcanic eruptions from the Valles caldera, New Mexico. *Journal of Volcanology*

and Geothermal Research, *199*(1-2), 53-68. https://doi.org/10.1016/j.jvolgeores.2010.10.008

Wolff, J. A., & Gardner, J. N. (1995). Is the Valles caldera entering a new cycle of activity? Geology, 23(5), 411-414. https://doi.org/10.1130/0091-7613(1995)023%3C0411:ITVCEA%3E2.3.CO;2

Wu, J., Cronin, S. J., Rowe, M. C., Wolff, J. A., Barker, S. J., Fu, B., & Boroughs, S. (2021). Crustal evolution leading to successive rhyolitic supereruptions in the Jemez Mountains volcanic field, New Mexico, USA. Lithos, 396, 106201. https://doi.org/10.1016/j.lithos.2021.106201

Yang, X., Bryan, J., Okubo, K., Jiang, C., Clements, T., & Denolle, M. A. (2023). Optimal stacking of noise cross-correlation functions. Geophysical Journal International, 232(3), 1600– 1618. https://doi.org/10.1093/gji/ggac410

Zimmerer, M. J., Lafferty, J., & Coble, M. A. (2016). The eruptive and magmatic history of the youngest pulse of volcanism at the Valles caldera: Implications for successfully dating late Quaternary eruptions. Journal of Volcanology and Geothermal Research, 310, 50-57. https://doi.org/10.1016/j.jvolgeores.2015.11.021

Appendix

1.A Supplementary figures

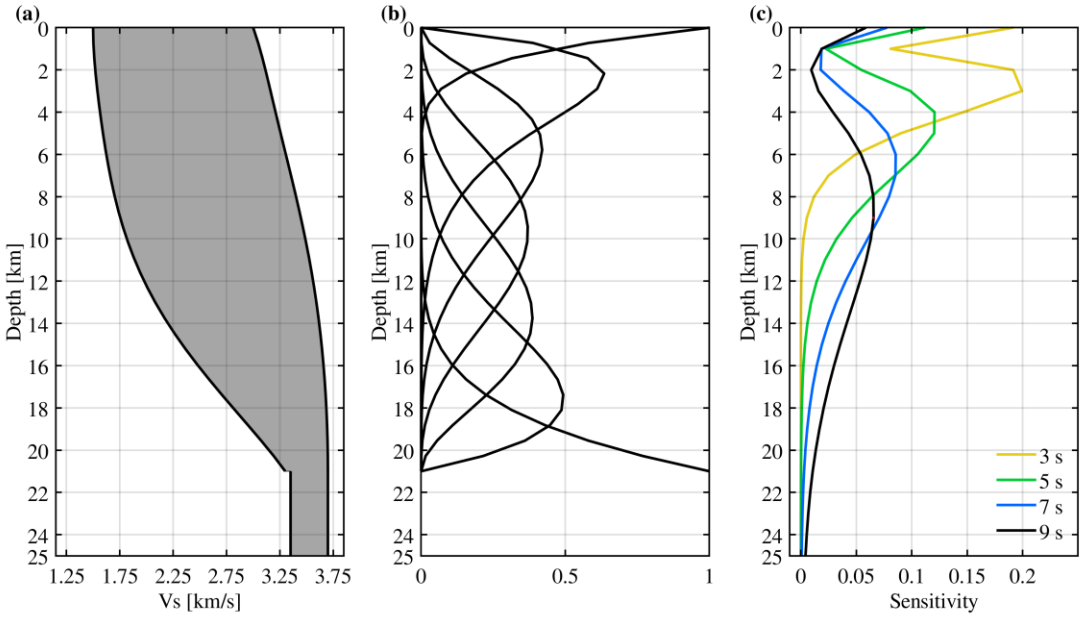

Figure S1. Vs search range, model parameterization, and example sensitivity kernels. a) A uniform prior Vs distribution was used within search range indicated by gray shading. b) The shape of the 7 b-spline functions used to parameterize the middle to upper crust is shown with solid black lines. The plots in a and b use a depth to half-space of 21 km. That depth was allowed to vary from 20-23 km in the inversion. C) Phase velocity sensitivity to Vs structure at periods of 3, 5, 7, and 9s calculated from the mean Vs profile (Figure 3) using SensKernel-1.0 (Levshin et al., 1989). Note that the BMMC inversion does not use these kernels; it accounts for nonlinearity by repeated forward modeling. The example kernels are shown here to help illustrate the typical sensitivity of the phase velocity measurements.

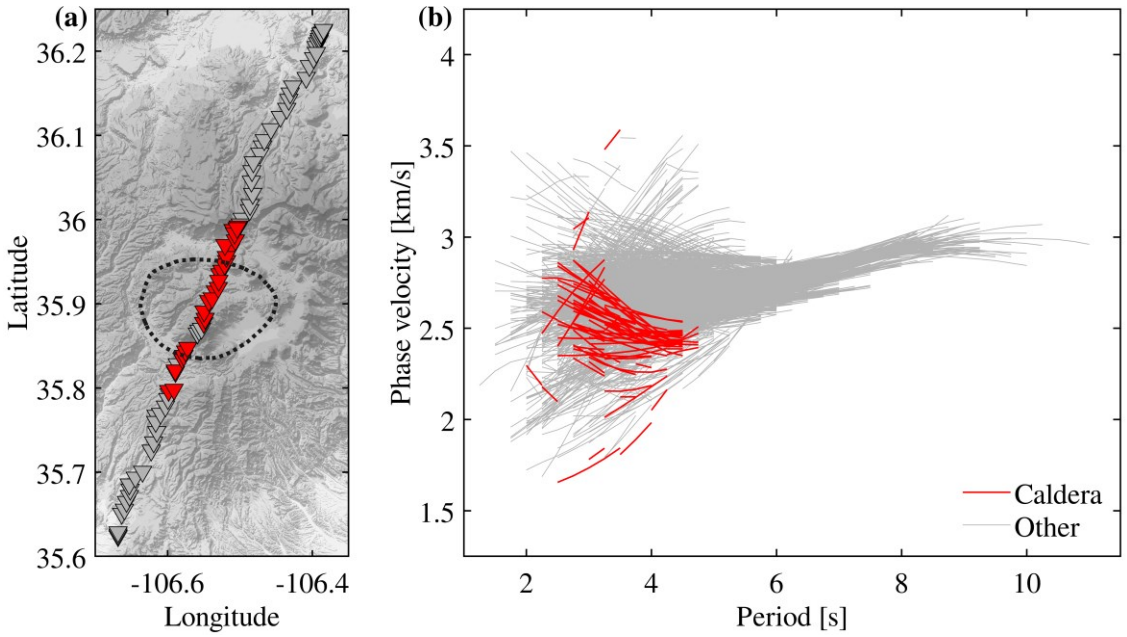

Figure S2. Phase velocity dispersion curves for all interstation paths and those confined within the topographically defined caldera. a) Topographic map showing all nodal seismographs (gray triangles) and those whose source and receiver are both within the topographic caldera (red triangles). b) Dispersion curves for all interstation paths (gray) and those whose source and receiver are both within the topographic caldera (red) as shown in a.

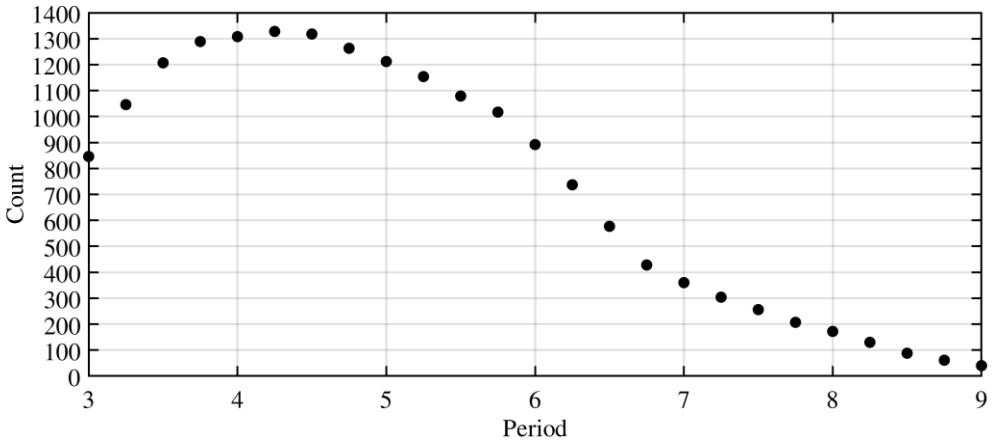

Figure S3. Number of interstation phase velocity measurements used at each period for phase velocity tomography along the transect.

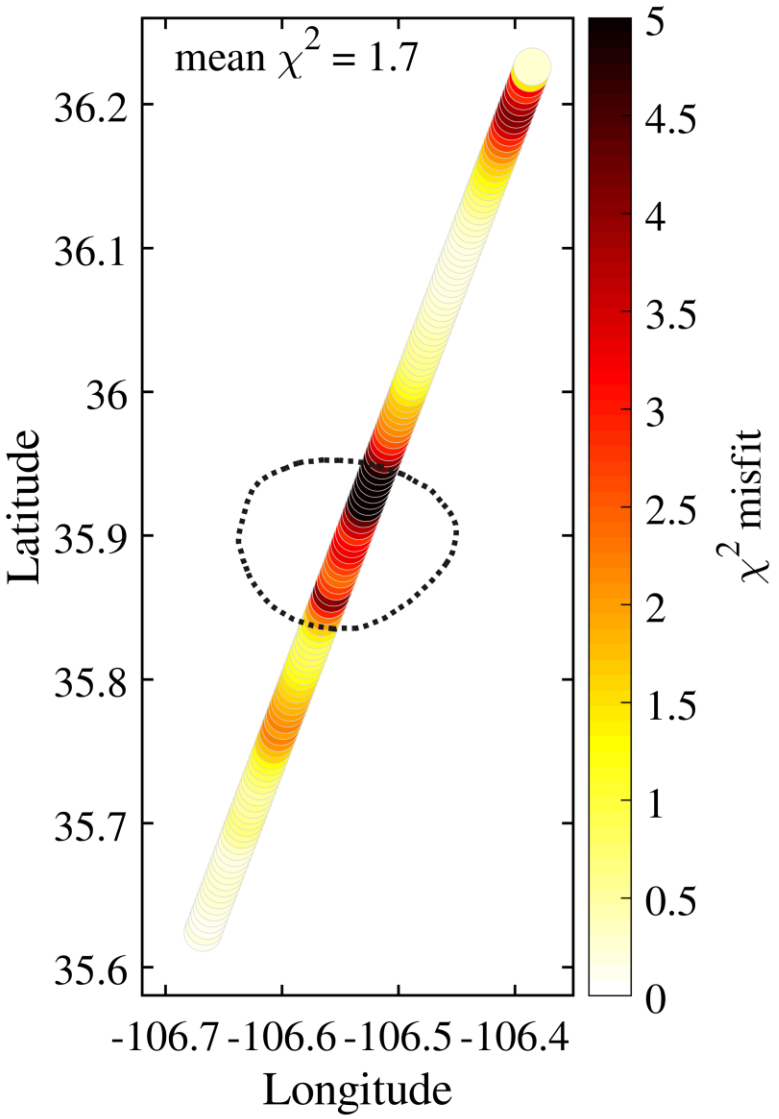

Figure S4. Map of average χ^2 misfits from the posterior distribution at each Vs inversion location. The mean χ^2 of all locations, 1.7, is given in the plot.

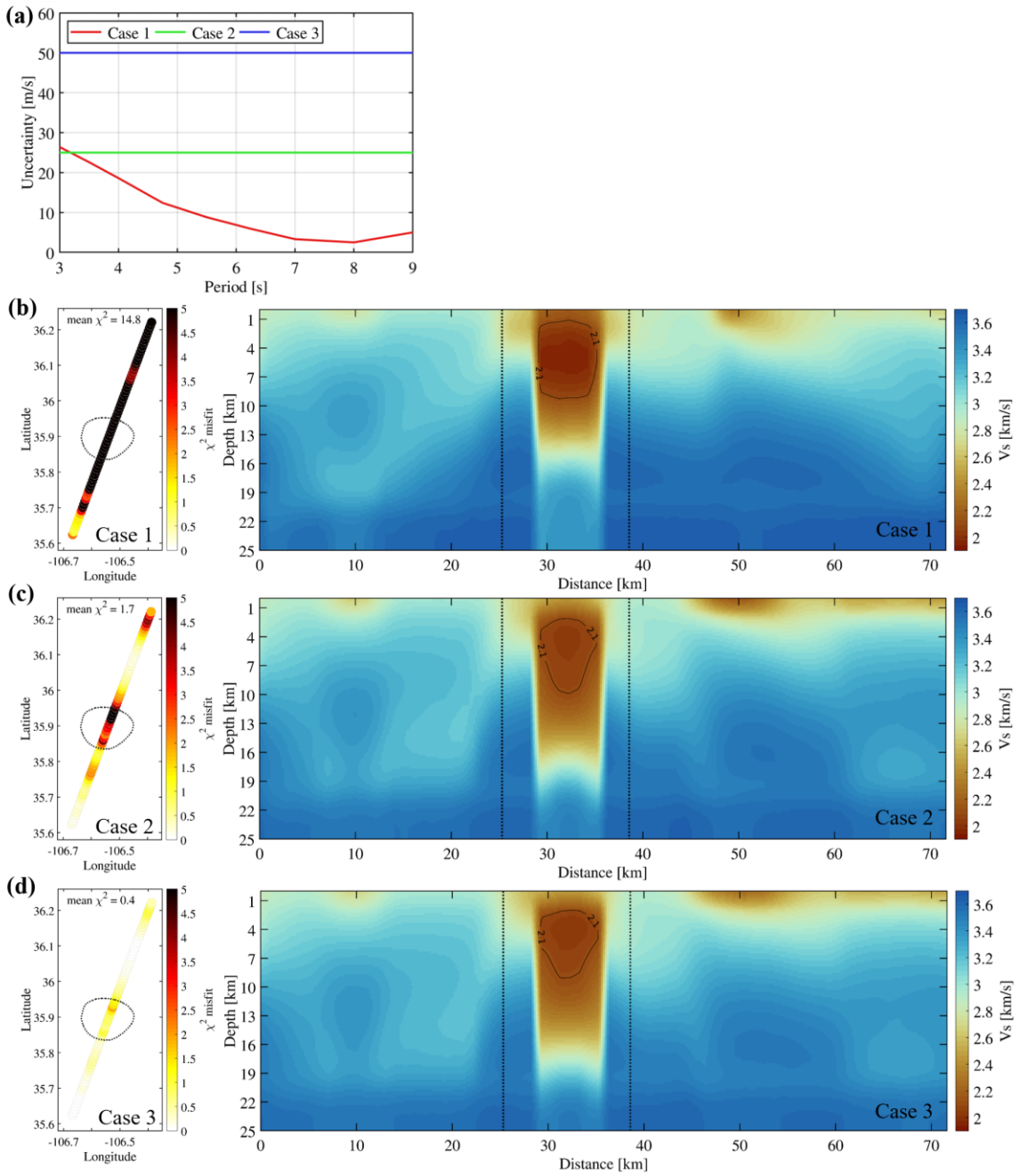

Figure S5. Uncertainty test cases and their BMMC inversion results. a) Uncertainties for each of the three cases. Case 1 uses uncertainties from bootstrap resampling of the phase velocity results and repeated inversions with the bootstrap samples. Case 2 uses a fixed 25 m/s uncertainty at all periods, which is the case presented in the main text. Case 3 uses a fixed 50 m/s uncertainty range. b) Misfit map and Vs cross section for case 1. c) same as b but for case 2. b) same as c but for case 3. Dotted lines in misfit maps and Vs cross section show the 1.25 Ma caldera's ring fracture.

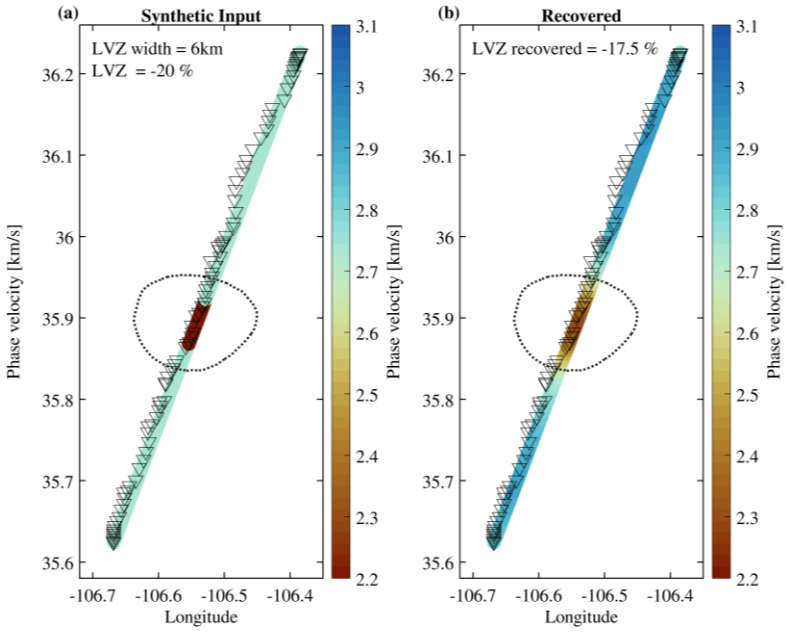

Figure S6. Phase velocity resolution test with strongly reduced velocities within the ring fracture of the caldera. a) The input structure includes a 6-km wide low-velocity anomaly with 4-s Rayleigh wave phase velocity reduced by 20%. For reference, the observationally estimated phase velocity anomaly at 4 s period is ~15% so this test is using a more severe anomaly. b) The recovered phase velocities from the inversion of synthetic data show that a peak velocity reduction of –17.5% is recovered. Thus, ~85% of the magnitude of the input anomaly was recovered

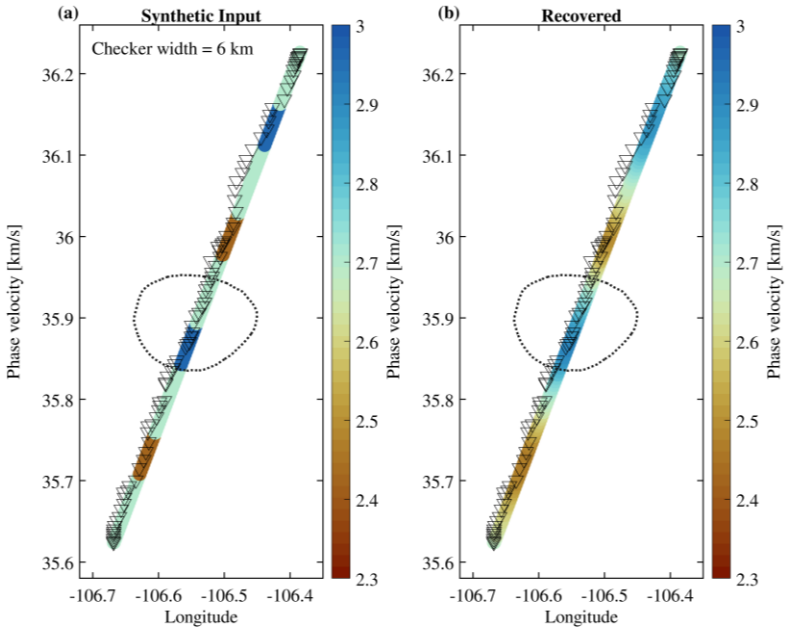

Figure S7. Phase velocity resolution test at 4 s period with alternating positive and negative velocity anomalies surrounded by neutral velocities. a) The input structure contains 10% velocity anomalies that are 6-km wide and separated by equal-widths of neutral velocities. b) All four input anomalies are recovered with slightly reduced magnitudes, but the anomalies within the interior of the transect are better resolved than those closer to the edges.

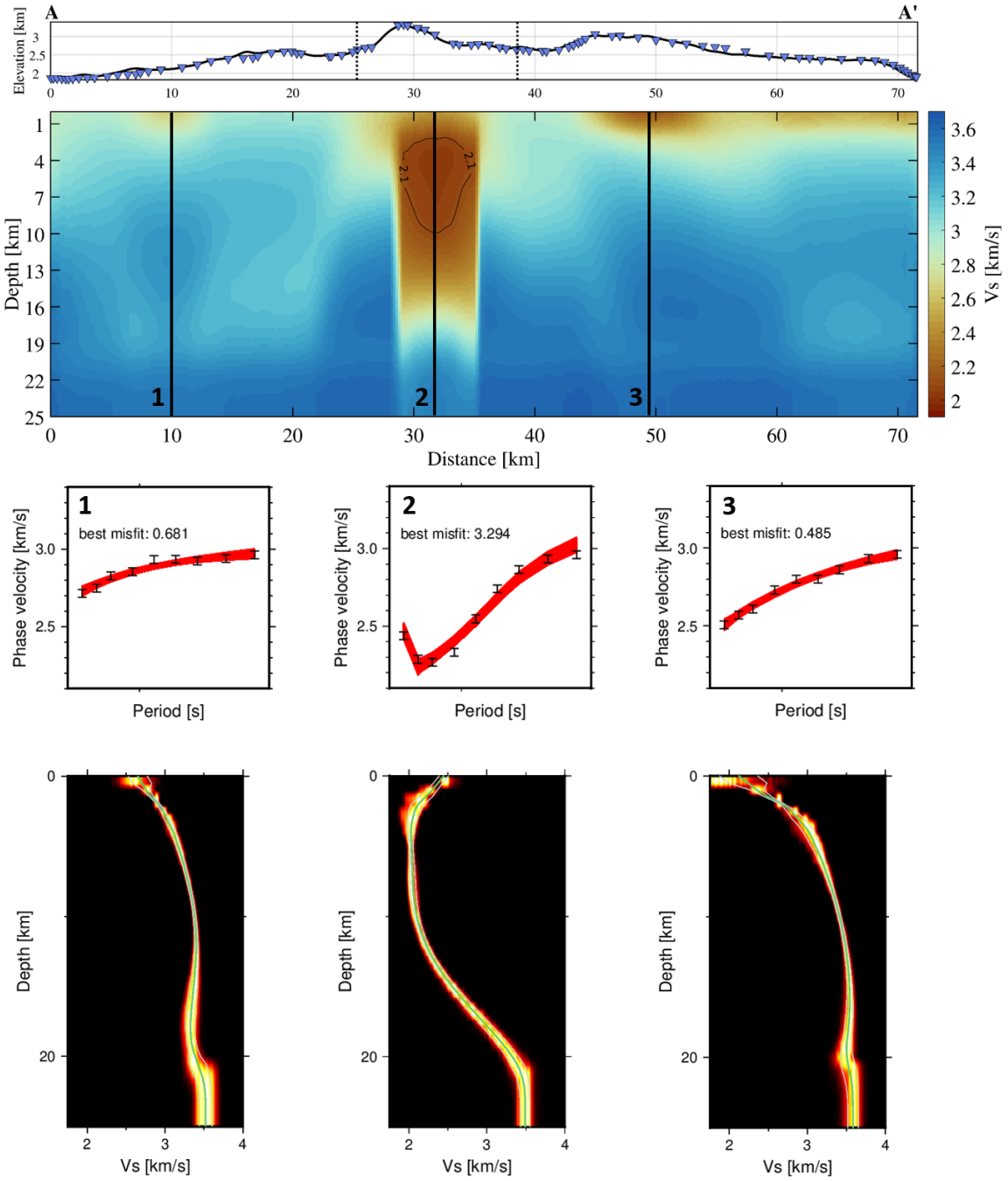

Figure S8. Phase velocity dispersion predictions and Vs profiles of the 2,000 best BMMC models at three points along the transect. The three points are shown and labeled on the Vs cross-sectional image from figure 3 in the top row. The middle row shows dispersion observations and uncertainties (black) and prediction ensembles (red) for each point. Corresponding 1D Vs profiles as a function of depth are shown in the bottom row. Green line is the mean of the posterior distribution.

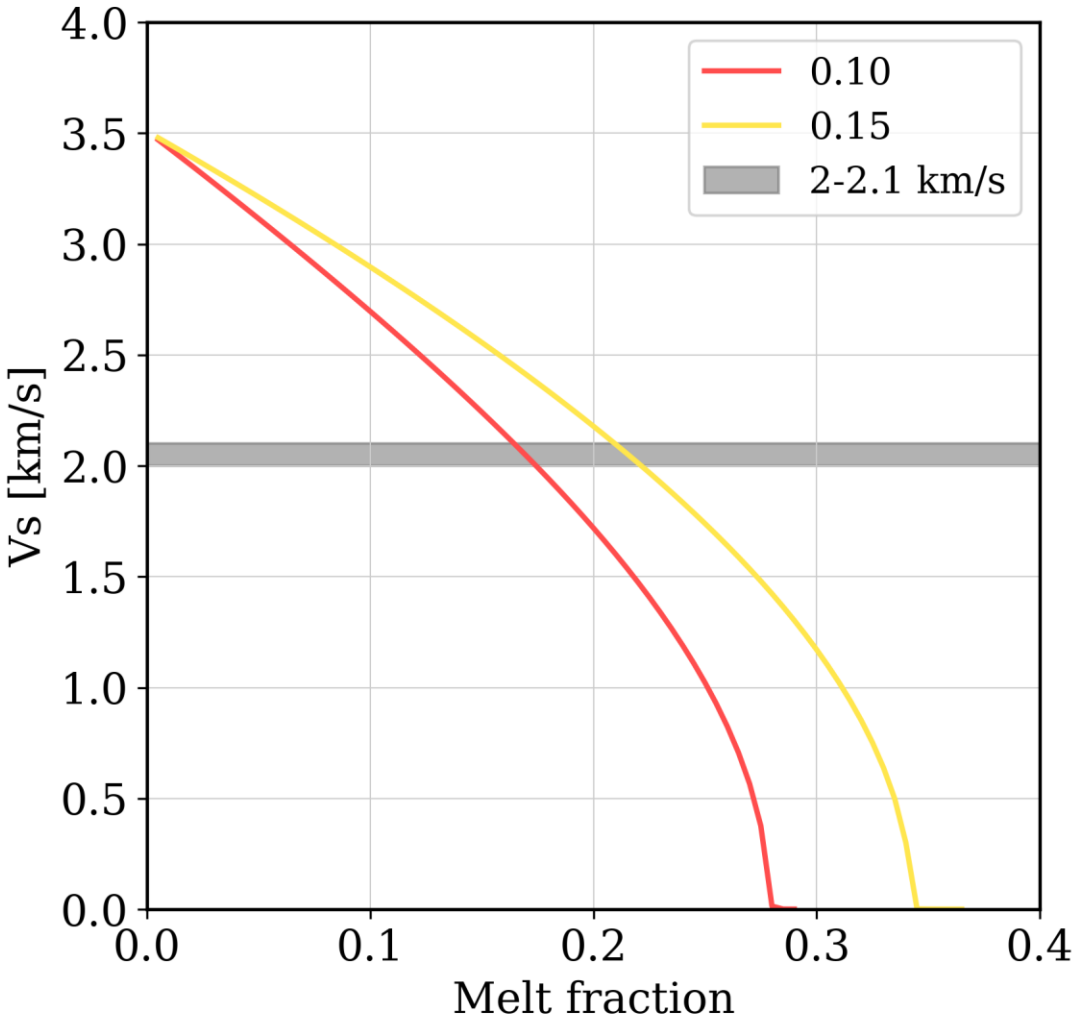

Figure S9. Vs as a function of melt fraction over aspect ratios indicative of textural equilibrium, 0.1 to 0.15. Solid phase Vs values were determined using the ~69 ka Banco Bonito rhyolite composition at 170 MPa (~5 km depth), and 700 C°. A density of 2.2 kg/m^3 and bulk modulus of 9 GPa were assumed for the melt phase.

1.B Supplementary tables

Station name	Latitude	Longitude	Approximate day of tip
28	35.89744	-106.5471	Before 10-10-2019
33	35.93139	-106.5132	Before 10-10-2019
37*	35.97542	-106.5064	10-30-2019
1011	35.86139	-106.563	Before 10-10-2019
1015	35.87358	-106.5505	Before 10-10-2019
1017*	35.88239	-106.548	10-20-2019
1019	35.92355	-106.5313	Before 10-10-2019
1020	35.93081	-106.5302	Before 10-10-2019
1024*	35.96445	-106.5131	10-20-2019
1027	35.99831	-106.4988	10-10-2019

Table S1. List of stations that tipped at some point during deployment. Stations with asterisk recorded >10 days of data that were used for ambient noise cross correlations. The other tipped stations were not included in our analysis.

Spline #	Lower bound	Upper bound
1	1.50	3.00
2	1.50	3.10
3	1.60	3.25
4	1.70	3.55
5	1.95	3.65
6	2.90	3.70
7	3.30	3.70

Table S2. Prior velocity range for each b-spline parameter in BMMC inversion.

Oxide	Weight%
SiO2	74.2
Al2O3	13.24
Fe2O3	1.82
MgO	0.67
CaO	1.49
Na2O	3.85
K2O	4.36

Table S3. Weight percent bulk major oxide compositions from Banco Bonito, the youngest dated rhyolite flow at Valles Caldera (Fig. 1; Spell and Kyle, 1989).

References

Levshin, A.L., Yanovskaya, T.B., Lander, A.V., Bukchin B.G., Barmin, M.P., Ratnikova L.I., Its E.N. (1989). Seismic Surface Waves in Laterally Inhomogeneous Earth. (Ed. V.I.Keilis-Borok), Kluwer Publ. House, Dordrecht/Boston/ London [Scholar]

Spell, T. L., & Kyle, P. R. (1989). Petrogenesis of Valle Grande Member rhyolites, Valles Caldera, New Mexico: Implications for evolution of the Jemez Mountains Magmatic System. Journal of Geophysical Research: Solid Earth, 94(B8), 10379-10396. https://doi.org/10.1029/JB094iB08p10379

2 Seasonality and spatial variability in shallow velocity structure (dv/v) at the Albuquerque Seismic Laboratory using a Repeating Impulsive Source

Authors and affiliations

Justin Wilgus[1,2]*

Adam Ringler[1]

Brandon Schmandt[2]

Robert Anthony[1]

Dave Wilson[1]

Ryan Stairs[2]

[1]U.S. Geological Survey, Albuquerque Seismological Laboratory, Albuquerque, NM, USA

[2]University of New Mexico, Department of Earth & Planetary Sciences, Albuquerque, NM, USA

∗Corresponding author

2.1 Abstract

Fractional changes in arrival times of late arriving seismic coda can provide details of time-dependent changes in relative velocity structure of the Earth (d*v/v*) and can often provide insights into evolving tectonic and environmental processes. Despite the significant contributions that measurements of d*v/v* have provided in understanding shallow subsurface processes, work focused on characterizing spatial variability and uncertainties associated with these measurements is uncommon. Here we make use of a repeating, impulsive source to assess lateral and vertical spatial variability of d*v/v*

measurements across a small-aperture (∼500 m) array, of posthole and borehole seismometers at the Albuquerque Seismological Laboratory (ASL). We use the moving window cross spectrum method to measure d*v/v* within the 4 to 12 Hz coda energy of the source. A consistent seasonal d*v*/*v* oscillation of ∼0.2% amplitude occurs at all stations with the minimum in winter and maximum in late summer, which we propose is linked to concentration of annual precipitation during the late summer. Among the sensors in the small-aperture array, we find d*v/v* amplitude variability of ∼0.1% at 1 standard deviation, half the seasonal d*v/v* oscillation amplitude of ∼0.2%. Thus, the seasonal oscillations are in phase across the array, but small-scale local structure may substantially modulate their amplitudes. Slight differences in the seasonal oscillation found at two of the sites may be linked to heterogeneous stratigraphy, which suggests d*v/v* measurements at frequencies of ∼4-12 Hz are sensitive to receiver side structural variations over ∼100 m scale laterally and with depth. These results serve to inform future studies of spatiotemporal variations in d*v/v*.

2.2 Introduction

Measurements of fractional changes of arrival times in late arriving seismic energy (coda), sometimes referred to as coda wave interferometry, often assume that coda is composed of the summation of randomly scattered waves (Aki, 1969; Aki & Chouet, 1975) and that changes in subsurface velocity structure are spatially homogenous (Snieder et al., 2002; Snieder, 2006). These assumptions lead to a fundamental relation underlying coda wave interferometry studies: that a change in arrival time (*t*) is directly correlated to the negative of a velocity (*v*) change, d*t/t* = -d*v/v*.

Monitoring changes in velocity structure through time (d*v/v*) can provide insight into how stress, strain, and poroelastic properties like pore pressure vary in Earth's shallow subsurface. More specifically, variations in d*v/v* have been correlated to discrete tectonic and volcanic events, groundwater fluctuations, and oscillatory environmental forcing from rainfall, snowpack, surface temperature, atmospheric pressure, and permafrost cycles (Obermann & Hillers, 2019). However, the study of d*v/v* is a relatively young field of seismologic research and questions remain as to how these causal mechanisms would manifest in a d*v/v* signal and how local geologic structure around the seismometers might influence measurements of d*v/v*.

Some of the earliest d*v/v* studies investigated the potential to monitor changes in stress (Reasenberg and Aki, 1974; Poupinet et al., 1984) and subsequent controlled experiments further demonstrated the feasibility of this approach (Gret et al., 2006; Silver et al., 2007; Niu et al., 2008). Since the mid-2000s, with the advent of seismic ambient noise interferometry as a continuous source (Lobkis and Weaver, 2001; Snieder, 2004; Shapiro and Campillo, 2004), d*v/v* measurements have been increasingly used to provide insight into stress and strain changes due to tectonic and volcanic processes. For example, Brenguier et al., (2008) associated a sharp d*v/v* decrease during the September 9, 2004 Mw6 Parkfield earthquake and its subsequent long-term recovery with coseismic and postseimic stress changes. Rivet et al., (2011) extended the use of d*v/v* from ambient noise interferometry to infer strain state. In that study, a decrease in d*v/v* was interpreted to result from nonlinear deformation in the

continental crust during a slow slip event in Mexico. Finally, using repeating earthquakes Hotovec-Ellis et al., (2022) identified d*v/v* cycles coincident with surface observed episodic collapse of the volcanic edifice at Kilauea volcano. Ultimately, d*v/v* measurements were suggested to be capable of monitoring magmatic inflation and deflation cycles (volumetric strain) over ~2 months during the 2018 event. The literature on monitoring tectonic and volcanic processes in the crust with d*v/v* is extensive, we simply survey these few examples as a demonstration.

Despite the potential insight d*v/v* can provide into crustal processes, these measurements must be interpreted carefully because there are many potential influences. They are often dominated by independent seasonal oscillations in both active tectonic (e.g., Hillers et al., 2015; Liu et al., 2020; Li et al., 2021) and volcanic (e.g., Sens-Schönfelder and Wegler, 2006; Hotovec-Ellis et al., 2014; Donaldson et al., 2019) settings. These seasonal oscillations can be so strong that they must be systematically removed to resolve tectonic signals of interest (e.g., Tsai et al., 2011; Clements and Denolle, 2018; Wang et al., 2019; Feng et al., 2021). However, seasonal oscillations also provide unique information about temporal variations in near near-surface material properties. Seasonal oscillations of d*v/v* have been used to infer poroelastic variation of shallow structure in response to fluctuations of groundwater (e.g., Sens-Schönfelder and Wegler, 2006; Hillers et al., 2014; Clements and Denolle, 2018; Clements and Denolle, 2023) and precipitation (e.g., Hillers et al., 2014; Wang et al., 2017; Feng et al., 2021). Additionally, these seasonal oscillations in d*v/v* may arise through other environmental forces including surface loading from rainfall (Froment et al., 2013; Obermann et al.,

2014) and snowpack (Hotovec-Ellis et al., 2014, Donaldson et al., 2019), as well as surface temperature changes (Meier et al., 2010; Hillers et al., 2015) and changes in atmospheric pressure (Silver et al., 2007; Niu et al., 2008; Gradon et al., 2021). The ability for d*v/v* to provide useful insights into both surface and deeper crustal processes is contingent upon correct interpretation of the causal physical processes responsible for the d*v/v* signal. This is often difficult due to uncertainties that can arise from temporal overlap (superposition) of numerous seasonal signals, potential phase delays associated with physical processes (i.e. diffusion rate), frequency dependent spatial sensitivity of scattered waves, atmospheric and tectonic environment of the study region, and seasonal stability of the source (Wang et al, 2020).

Sources used for d*v/v* studies can be repetitive controlled sources (Silver et al., 2007, Gret et al., 2006), repetitive natural sources like highly similar earthquakes (Poupinet et al., 1984, Hotovec-Ellis et al., 2022), and ambient seismic noise processed into empirical Green's functions at regular intervals (Campillo and Paul, 2003; Lecocq et al., 2014). Ambient noise is particularly well suited as it does not require a discrete ballistic source and its continuous activity allows for increased temporal resolution of d*v/v*. However, some complexity can arise when using ambient seismic noise as a source. The Green's functions from cross correlations can be sensitive to changes in the ambient noise source distribution (Stehly et al., 2006), changes in the frequency content (Zhan and Clayton, 2013), and instrument timing issues (Hable et al., 2018). Although coda may be less sensitive to noise source distributions than direct arrivals (Froment et al., 2010). An ideal d*v/v* source would be consistent in amplitude, have a fixed spatial

location, repeat frequently over long periods of time, and exhibit coherent long-duration coda upon arrival. Some recent studies use opportunistic cultural sources that approach these preferable source characteristics to measure d*v/v* (Pinzon-Rincon et al., 2021; Sheng et al., 2022; Stairs et al., 2023). Such sources may effectively mitigate uncertainties associated with traditional source studies and allow for more detailed constraints on spatial variability of dv/v measurements.

The spatial extent of d*v/v* observations is controlled by sensitivity of scattered waves in the late arriving coda and the interstation distance over which ambient noise cross correlation is conducted. In a simplified tectonic setting, scattered wave sensitivity focuses near the source and receiver (Obermann et al., 2013; Mayor et al., 2014; Margerin et al., 2016) and in applications of d*v/v* the variability between stations can, in part, be attributed to localized sensitivity to structure. In some cases, measurements of d*v/v* can vary widely between adjacent stations (Meier et al., 2010; Li et al., 2021; Bonilla & Ben-Zion, 2021; Rodríguez Tribaldos, & Ajo-Franklin, 2021). Large interstation distances ~10s of km, typical of long-term broadband deployments, can exacerbate variability or may average out local changes from structure (Meier et al., 2010). Such variability has prompted a shift toward single station analysis with autocorrelation or cross-component correlation, which serves to focus sensitivity by collocating the source and receiver (e.g., Wegler and Sens-Schönfelder, 2007; Ueno et al., 2012; Kim and Lekic, 2019; De Plaen et al., 2019; Donaldson et al., 2019; Feng et al., 2021; Clements and Denolle, 2023). However, autocorrelation can increase the signal-to-noise ratio of higher frequency energy. Consequently, dv/v measurements from autocorrelation likely have

higher contributions of body wave scattering, which is sensitive to different structure (Barajas et al., 2022) and may be optimal at different frequencies than surface wave scattering measured in more conventional source-receiver studies (Kim and Lekic, 2019; Donaldson et al., 2019; Clements and Denolle, 2023).

In this study, we measure d*v/v* over multiple years to investigate small-scale spatial variability of d*v/v* across a small-aperture (<600 m) array of posthole seismometers and two deep (90 and 188 m) borehole seismometers at the Albuquerque Seismic Lab (ASL; Figure 1). As opposed to using more common active and passive sources, we use the coda of a fixed location, impulsive, repeating, cultural source which provides important simplifications that serve to mitigate extraneous signals and uncertainty in d*v/v*. Ultimately, we seek to quantify the consistency of d*v/v* measurements between nearby similarly installed high-quality sensors observing a highly repetitive controlled source to determine the relative influences of small-scale geologic structure and sensor installation.

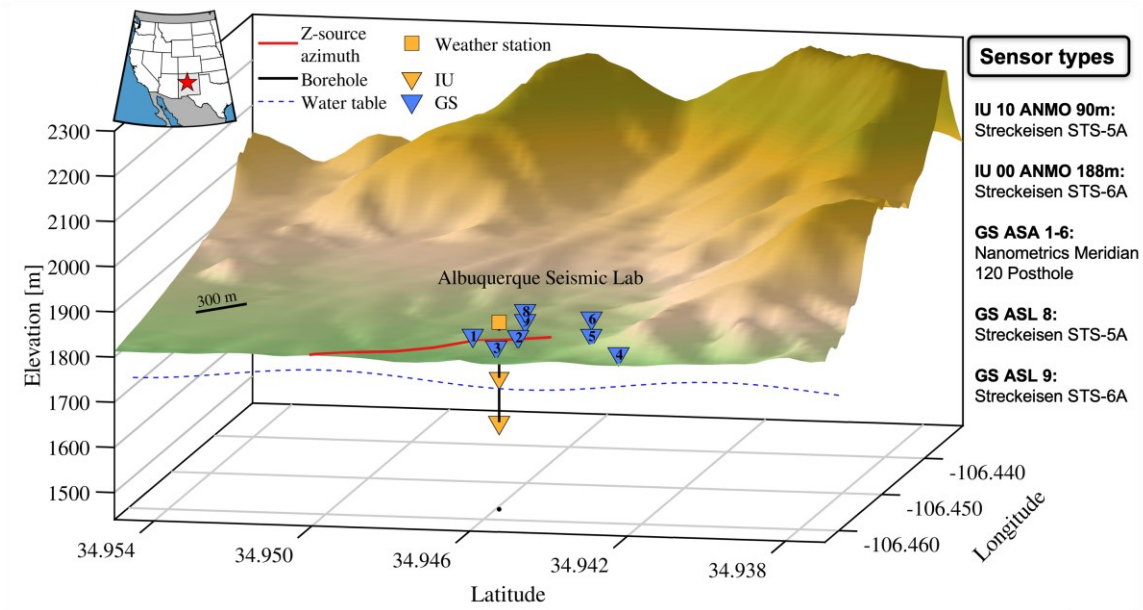

Figure 1. Topographic map showing sensor locations used in this study at the Albuquerque Seismic Laboratory. Orange markers are sensors that are part of the Global Seismographic Network (GSN) Station ANMO which includes two borehole seismometers: an STS-5 at 90 m and STS-6 188 m depth and a weather station (square) located on the surface. Blue triangles are small-aperture array stations each installed at ~2.6 m depth, with names ASA1 through ASA6, ASL8, and ASL9 numbered accordingly. Red line shows path and azimuth of Z-machine source signal used in this study. Blue dashed line shows depth (~90 m) to water table. Seismic sensor types are listed to the right.

2.3 Data

The ASL is situated in central New Mexico, on the eastern flank of the Albuquerque Basin (Figure 1; Connel, 2001). Fractured granite and shallow (<10 m at ASL) alluvium are the dominant rock type in the vadose zone near ASL as revealed by borehole and near surface posthole stratigraphy (Anthony et al., 2020). Water table depth can vary widely but is ~90 m deep. The study area is relatively tectonically quiescent (Astiz et al., 2014; Nakai et al., 2017), which helps to avoid spurious signals that arise from frequent seismicity and/or large events causing anomalous deformation and changes in stress which can obscure baseline d*v/v* measurements (Brenguier et al., 2008; Brenguier et al.,

2016; Donaldson et al., 2019). Notably, the ASL was sited in 1960 due to exceptionally low-noise levels around 1 Hz (Moore et al., 2018) and the laboratory continues to have relatively low-noise levels across most of the seismic spectrum (5 Hz to < 1 mHz) compared to the rest of the United States (Anthony et al., 2022b; Ringler et al., 2020).

Numerous high-quality broadband stations operate at the ASL. The Global Seismographic Network (GSN) station ANMO has been continuously recording data since 1989, however World Wide Standardized Seismographic Network (WWSSN) records for this station date back to the 1960s. In the modern configuration, station ANMO has two borehole sensors: a primary sensor (location code: 00) at 188 m depth and a secondary (location code: 10) sensor at 90 m (Figure 1). In 2017, in preparation for the deployment of USArray Transportable Array in Alaska (Busby and Aderhold, 2020), ASL8 and ASL9 were identically installed in two co-located (1.77 m apart; Anthony et al., 2022c) 2.6 m cased postholes that were hammer drilled into granite. In 2019, ANMO was supplemented with a small-aperture (< 600 m), 6-element broadband seismic array with station names ASA1 to ASA6 (Anthony et al., 2020). Identical to ASL8 and ASL9, each array element is installed in a 2.6 m cased posthole emplaced in weathered granite. In this study, we consider data from these 10 seismic stations recorded at 100 samples-per-second data for the ASA stations and 40 sample-per-second data for all others.

To measure changes in dv/v we make use of a unique, impulsive repeating seismic source emanating from the Sandia National Laboratories Z pulsed powered facility (https://www.sandia.gov/media/zpinch.htm; Matzen et al., 2005; Sinars et al.,

2020). The Z-machine is a high-frequency electromagnetic wave generator with the purpose of creating extreme pressures and temperatures in a small sample assembly. Each Z-machine pulse is capable of outputting ∼22 MJ total energy release within a nearly impulsive ∼90 ns time window (Jones et al., 2014; Sinars et al., 2020). Stairs et al., (2023) demonstrate that each shot generates a ∼4-12 Hz seismic signal of several seconds duration that is readily recorded on the small-aperture array of seismometers 12.5 km away at ASL. Although Z-machine shot energy can vary depending on the experiment (Sinars et al., 2020), events of roughly -1.6M_L are typical and seismic waveform characteristics remain very similar between shots (Figures 2,3, Stairs et al., 2023). About 2 shots per week are typical (Stairs et al., 2023), though we note a decrease of seismic detections in the fall of 2021 (Figure 2, Figure S2 in Appendix 2.A). The Z-machine source signal provides important simplifications over the more commonly used active and passive sources used to measure d*v/v*: 1) the source location is known and constant and 2) the source will not suffer from the noise wavefield contamination which effectively removes the possibility of any extraneous contribution to the d*v/v* signal.

Additionally, we use continuously recorded 1 sample-per-second ANMO weather station data (location code: 50; figure 1) to track environmental factors that are known to impact d*v/v* observations, such as precipitation (channel code: LRI), temperature (channel code: LKO), and absolute barometric pressure (channel code: LDO). These co-located weather data combined with high-fidelity seismic data that record the Z-machine seismic signal on a near-identically installed small-aperture array of stations,

create a unique opportunity that to track seasonality and small-scale spatial variability of dv/v.

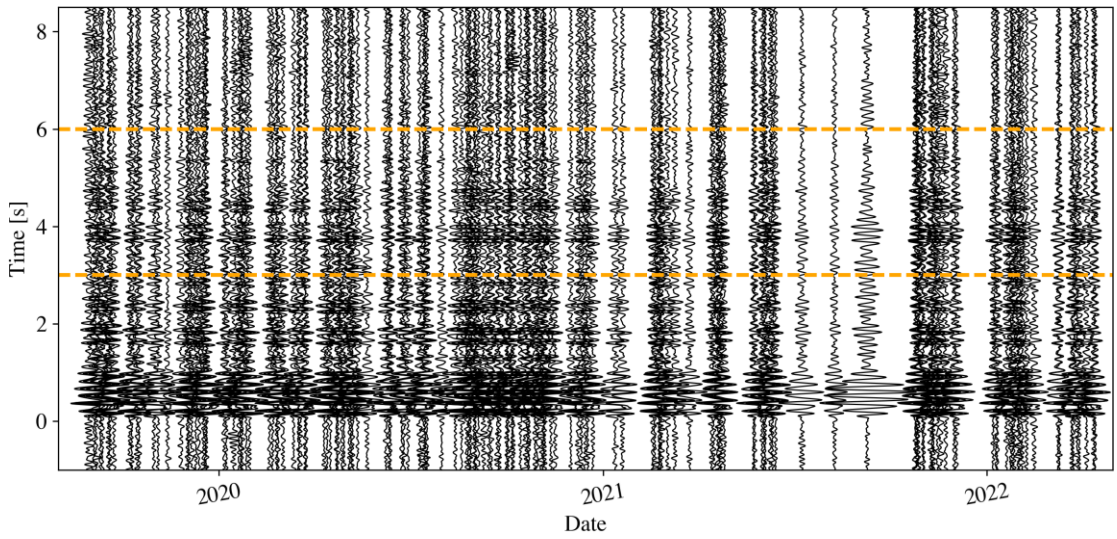

Figure 2. Z-shot records from the radial component of ASA6 in the 4 to 12 Hz frequency band as a function of time. Dashed orange lines show the 3 s window used to measure delay times.

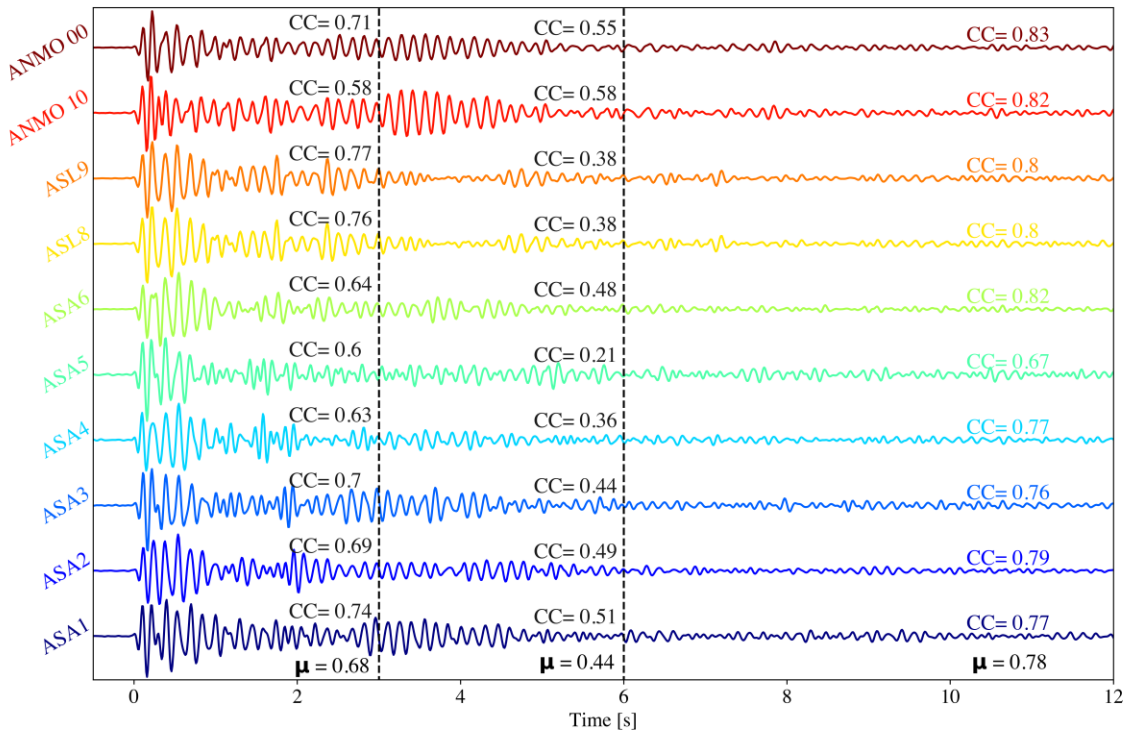

Figure 3. Normalized stacks of quality controlled radial component Z-machine events between 2019-08-28 and 2022-04-14 for each station. These station stacks were used as the reference during MWCS d*v/v* measurement. Dashed black lines bound the 3 s window used to measure delay times. Each station reference stack is color coded. Colored cross-correlation coefficients (CC) are from quality controlled individual Z-machine trace coefficient averages through time within a 17 s window starting a few seconds before initial peak arrival and reflect self-similarity of Z-shots for a given station. Black colored values are mean CC between reference stacks within a 0-3 s window (labeled left of 3s) and a 3-6 s (labeled left of 6s) and reflect comparative interstation waveform similarity of the ballistic and coda arrivals respectively. Respective averages (**μ**) are given for each set of CC values at the bottom of the plot.

2.4 Methods

We first compiled a catalogue of Z-machine events using a template matching method whereby cross correlation is conducted with a template against continuous timeseries data. Prior to template matching, we remove the instrument response from all seismic data for each time window, rotate the horizontal channels into radial (R) and transverse

(T) components using the known Z-machine location, and apply a 4 to12 Hz bandpass filter. Cross correlation is conducted during template matching and the maximal cross correlation coefficient (CC) is retained for each window. Stairs et al., (2023) found that the R component demonstrated higher SNR and waveform similarity than the vertical (Z) and T components. We generally follow the template matching approach of Stairs et al., (2023) focusing event detections to the secondary ANMO sensor (location code: 10). However, to further optimize the number of detections and avoid any temporal gaps we focus on only the R component and use multiple high-quality Z-machine detections from Stairs et al., (2023) as templates rather than a 3-component subset average. Cross correlation coefficients (CC) > 0.5 are considered a detection. False detections were mitigated with 1) manual inspection and removal of detections with highly dissimilar waveform characteristics or anomalous amplitudes and 2) quality control of waveform similarity at each station by culling average Z-machine detection CC < -1σ, where σ is 1 standard deviation. Template matching was conducted between January 2014 to April 2022 and identified 1,369 Z-machine shots.

To assess waveform similarity and obtain a secondary quality control metric we calculate the mean (CC) of each Z-machine detection trace with all other Z-machine detection traces for every ASL sensor used in this study (Figure 3). Because accurate measurement of d*v/v* requires a high level of coherence we further cull Z-machine detection traces with CC averages < -1σ for each station. The remaining traces are then aligned using multi-channel cross correlation at each station (VanDecar & Crosson, 1990; Figure S2 in Appendix 2.A). To ensure alignment on the first arrival, alignment is

conducted twice. The initial alignment window broadly includes most of the Z-shot duration while the second alignment window is smaller and focuses on only the first few phases of the signal arrival.

The aligned Z-machine shot traces are then used to construct a daily 90-day moving window average of Z-machine events (Figure S2 in Appendix 2.A). This creates daily sub-stacks of Z-machine events for each of the 10 seismic stations. We retain only daily sub-stacks that include at least 10 high-fidelity Z-machine shots. Thus, for each station we have a 1-sample-per-day timeseries of event stacks, however gaps exist during time periods that contain few Z-machine shots (Figure S2 in Appendix 2.A).

We compare stacks of the culled and aligned timeseries data from each sensor to characterize the ballistic and coda arrivals of the Z-machine seismic source signal across the ASL stations (Figure 3). The small-aperture array allows for further characterization of the Z-machine seismic source with array processing. Through frequency-wavenumber (f-k) analysis the relative power, back azimuth, and apparent velocity of the ballistic and coda arrivals can be determined (e.g., Capon, 1969; Schweitzer et al., 2002). We follow the f-k analysis approach from Anthony et al., (2020) using a 0.5 s window with 90% overlap on stacks of all Z-machine events for each ASA station (Figure 4). Plotting the stacks of the Z-machine source signal at their respective distance from the Z-machine and roughly fitting a linear moveout allows for determination of a simple, yet independent, estimate of the apparent velocity of the ballistic arrival (Figure S1 in Appendix 2.A).

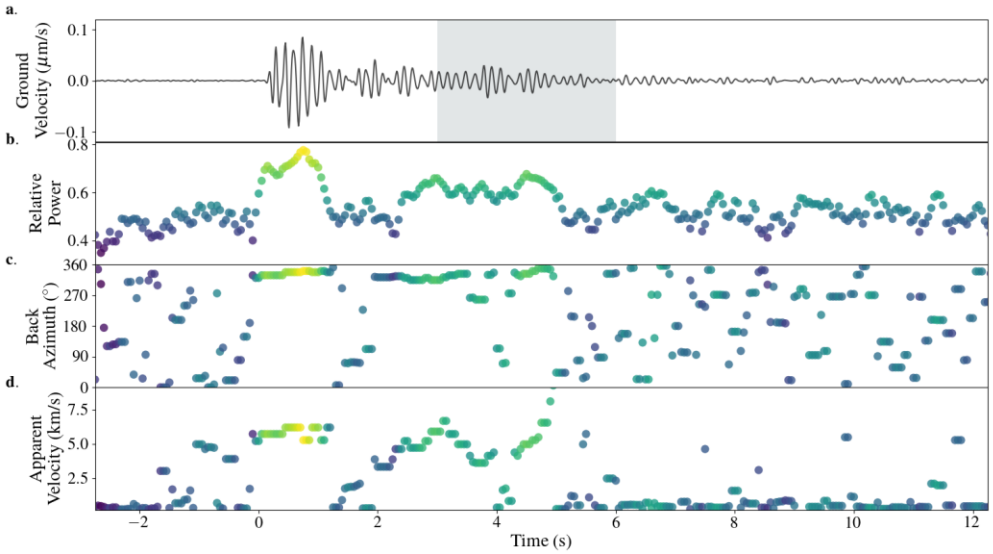

Figure 4. Array processing results from f-k analysis on stacks of all Z-machine events for each ASA station. a) Radial component stack of all Z-machine seismic signal trace from station ASA6. Gray shaded region bounds the 3-6 s coda window used for analysis and shown in figures 2 and 3. b) Relative power across ASA array stations. Stacking brought trace amplitudes to near-zero values, so for array processing purposes we added random noise before the first arrival. The colorbar tracks power amplitude. c) Back azimuth, and d) Apparent velocity of the Z-machine seismic signal through time across the ASL small-aperture array. Colors in c and d are adopted from b to more clearly correlate power for a given Back azimuth and apparent velocity.

Numerous methods exist to measure velocity perturbations through time of late arriving coda (Yuan et al., 2021). Here we follow the widely used Moving Window Cross Spectrum (MWCS) method of Clarke et al., (2011) as implemented in the software package MSNoise (Lecocq et al., 2014). We adopt the quality control metrics of coherence, error, and delay time from Jiang et al., (2019). Figure 5 illustrates an example of this process for a single event. Key MWCS equations from Clarke et al., (2011) used in the creation of Figure 5 are noted in the figure caption. Each daily d*v/v* measurement requires a current Z-machine trace as well as a reference stack which we

choose to be a stack of all the aligned and quality-controlled events for each individual station (Figure 3). Although the ballistic arrival of the sources across each station are similar with a mean CC of 0.68, they are different enough in the late arriving coda, 0.44, that a shared reference stack might average out destructively and diminish the late arriving coda signal or constructively interfere to create a non-physical signal. We choose a window of 3 s starting 3 s after peak arrival as this captures the bulk of uninterrupted coda arrivals (Figures 2 and 3). The measurements are conducted within the entire 4 to 12 Hz frequency band using a 2 s sliding window with a 0.25 s step size. We further cull final daily delay times that do not meet the criteria of coherence > 0.65, error < 0.1, and delay time < 0.1. We follow the same workflow for the Z-component to analyze particle motion of the initial direct arrival for ANMO (location code: 10), the station on which detections were conducted. ASA stations began recording at the end of 2019 which bounds our comparative d*v/v* analysis to just over 2 years (Figure 2).

To estimate spatial uncertainty of our results we calculate a simple bootstrap resampling. We first resample the d*v/v* measurements for each day using an index of integers randomly generated between 1 and 10 (the size of the sample, 10 stations) allowing for repetition. Taking the mean of the resampling for each day creates a new d*v/v* timeseries. This process is iterated to create a posterior distribution of 1000 timeseries. Iteration values above 1000 showed negligible change in uncertainty. The daily σ of the posterior distribution provides uncertainty constraints on spatial variability through time and is plotted alongside dv/v results. This approach assumes a gaussian distribution based on central limit theorem. The average spatial uncertainty through

time is determined with, $\frac{\sum_{i=1}^{n} |(\mu_i + \sigma_i) - \mu_i|}{n}$ where, μ is the mean, and σ is one standard deviation of the posterior distribution for a given day in the timeseries.

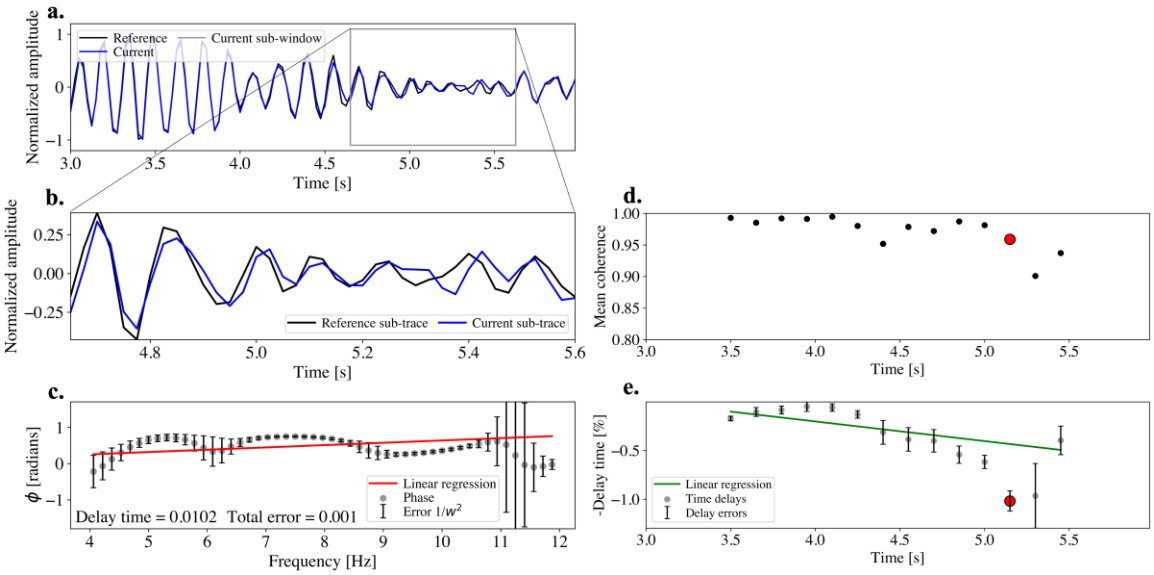

Figure 5. Example of how delay time is measured for a single Z-machine shot (2017-03-01, green line in Figure 6) on the ANMO 10 radial component. a) Reference stack and current traces within the 3s measurement window. Grey box shows one incremental step of the moving sub-window. b) Expanded view of timeseries within sub-widow shown in a. c) Unwrapped phase displacement (ϕ) across the 4-12 Hz frequency range (grey dots). Red line is linear regression fit to ϕ. The slope of the linear regression is the delay time for the sub-window and is calculated with a weighted least-squares inversion, eq. A6 in Clarke et al., (2011). Delay time is given in the figure and represented as a large red dot in e. Error bars are determined with $1/w^2$ where w is the weight from eq. A5 in Clarke et al., (2011). Y-axis is windowed to show slope, the largest error not shown is ~3 ϕ. The total error for the sub-window is determined with the rule of propagation errors eq. A7 in Clarke et al., (2011) which is given in the figure and shown in the delay error bar on large red dot in e. d) Mean coherence of sub-windows. Coherence is calculated with eq. A3 in Clarke et al., (2011) and is a measure of similarity between current and reference sub-traces. Red dot is mean coherence between sub-traces shown in b. e) Moving sub-window delay times (grey dots) and their respective total errors. Green line is linear regression to measurements that meet quality control criterion. The slope of the linear regression is again calculated with a least-squares inversion using time delay errors as weights, eq. A11 in Clarke et al, (2011). Red dot and associated error reflect values from sub-trace shown in c. The slope of green line is the final measurement of dv/v for the day. This process is iterated daily to create final dv/v timeseries.

2.5 Results

The initial peak arrival of the Z-machine source moves across the ASL from an azimuth consistent with the Z-machine location and an apparent velocity of ~5.5-6.5 km/s (Figure 4, Figure S1 in Appendix 2.A). The velocity is generally consistent with a P-wave turning in competent granite (Vernon et al., 1998) and roughly agrees with an absolute local crustal P-wave velocity estimate of 5.45 km/s from array processing of a local earthquake (Anthony et al., 2020; Figure S1 in Appendix 2.A). Particle motion behavior of the initial peak arrival is also indicative of a P-wave arrival (Figure S3 in Appendix 2.A). Particle motions of the coda, which consist of scattered waves, are complex and do not display a clear pattern that could be readily associated with any particular wave type (Figure S3 in Appendix 2.A). However, this complexity may be expected because scattered waves arrive over a range of azimuths, angles, and times (Aster et al., 1990). Stacks of Z-machine shots at each station show clear and consistent arrivals up to ~6 s after the initial peak arrival (Figures 2, 3, S2 in Appendix 2.A). Waveform similarity between individual Z-machine events on each station is high with a mean CC value of ~0.78 (Figure 3). However, similarity of waveforms between stations are lower for the ballistic arrival (0-3 s) and significantly lower for the coda arrivals (3-6 s), with mean CC values of 0.68 and 0.44 respectively. Array power of the ballistic arrival is ~ 0.7 - 0.8 in the first 1 s window of arrival while the coda window (3-6 s) has an array power of ~ 0.45 to 0.68 (Figure 4b).

Cyclical variations in amplitude and arrival times in the 90-day moving average of events on 5 years of ANMO 10 data are a first order indicator of seasonality within the

late arriving coda (Figure 6). This seasonality is quantified with d*v/v* measurements revealing clear seasonal oscillations ranging from -0.2 to 0.2 % with maxima during summer between July and September and minima during winter between January and March, over the span of 5 years. The pattern of seasonality is similar to the results of Stairs et al., (2023) but a few months delayed in phase. The stricter MWCS quality control and shorter coda time window (3-6 s rather than 1-6s) used in this study could be contributing factors to this difference. Additionally, the difference could be due to the different time periods used to construct the MWCS reference and/or long-term averaging over 20 years rather than analyzing 5 years during which Z-machine shots were consistent in time, amplitude, and waveform similarity (Figure 6).

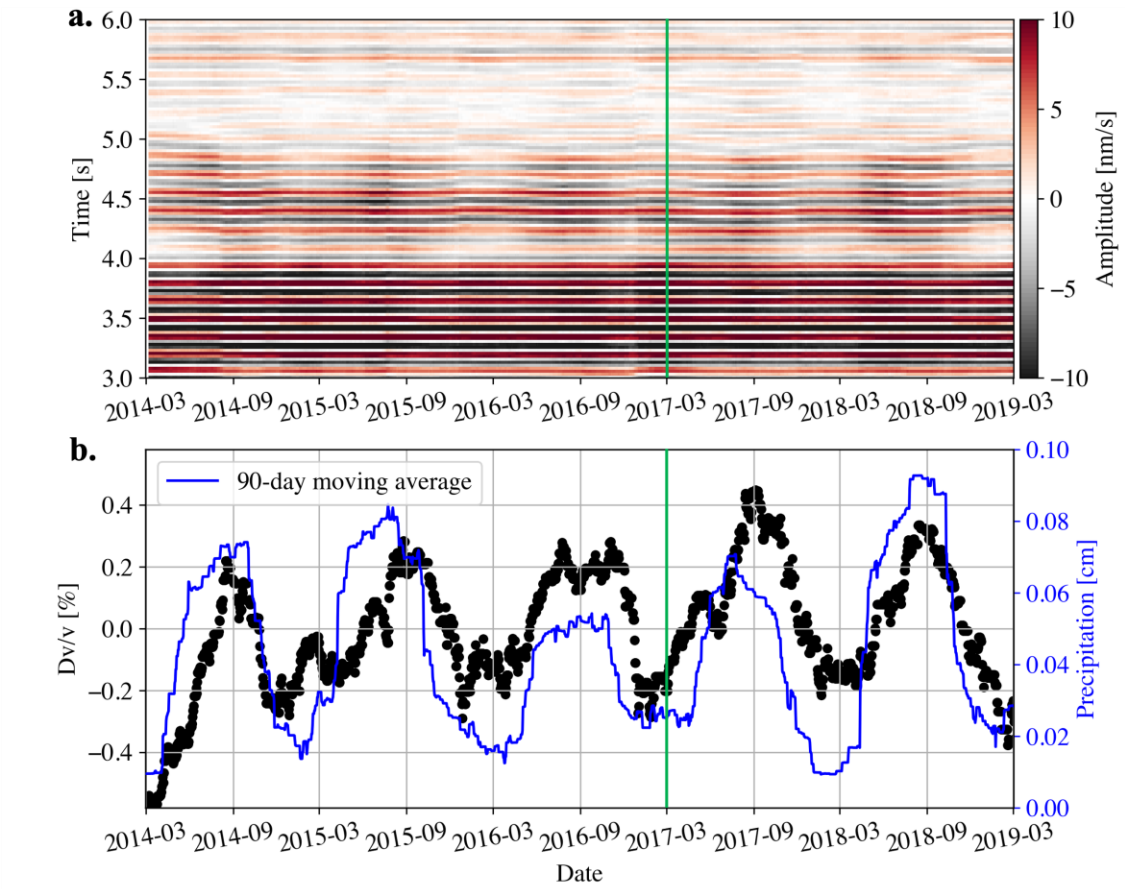

Figure 6. Velocity changes through time at ANMO 10. a) Daily 90-day moving window stacks of quality-controlled traces. Systematic seasonal amplitude and arrival time changes can be seen in the late arriving coda. b) Velocity variations through time (d*v*/*v*) compared to precipitation. Clear seasonality in d*v*/*v* is present and corresponds with changes in arrival time and amplitude visible in seismograms shown in a. The 90-day moving average precipitation is from the ANMO weather station (blue line) and is well correlated with d*v*/*v*. Green line on 2017-03-01 corresponds to the MWCS measurement example shown in Figure 5.

Comparison of d*v*/*v* for all ASL stations from 2019 to 2022 reveals a consistent seasonal oscillation pattern that matches the magnitude, minima, and maxima found for the 10 location code sensor of ANMO (Figure 7). Subtracting the mean of all d*v*/*v* timeseries from each station provides constraints on the spatial variability across ASL. Distributions are roughly centered around zero and have sigma values roughly ≤ 0.1%

(Figure 8). This suggests there is no bias in the distribution of a particular station, but there are small scale changes between stations that vary with time (Figure 7). A correlation matrix of the dv/v signals for each station reveals that ANMO 10 and ASA4 have some of the lowest correlation values and interestingly, with a CC of 0.36, are not well correlated with each other. The low correlations of ANMO 10 and ASA4 are also reflected in their average dv/v correlation values over all stations, 0.56 and 0.57 respectively, which is below the average of 0.67 for the entire correlation matrix. Average spatial uncertainty through time is 0.02 %.

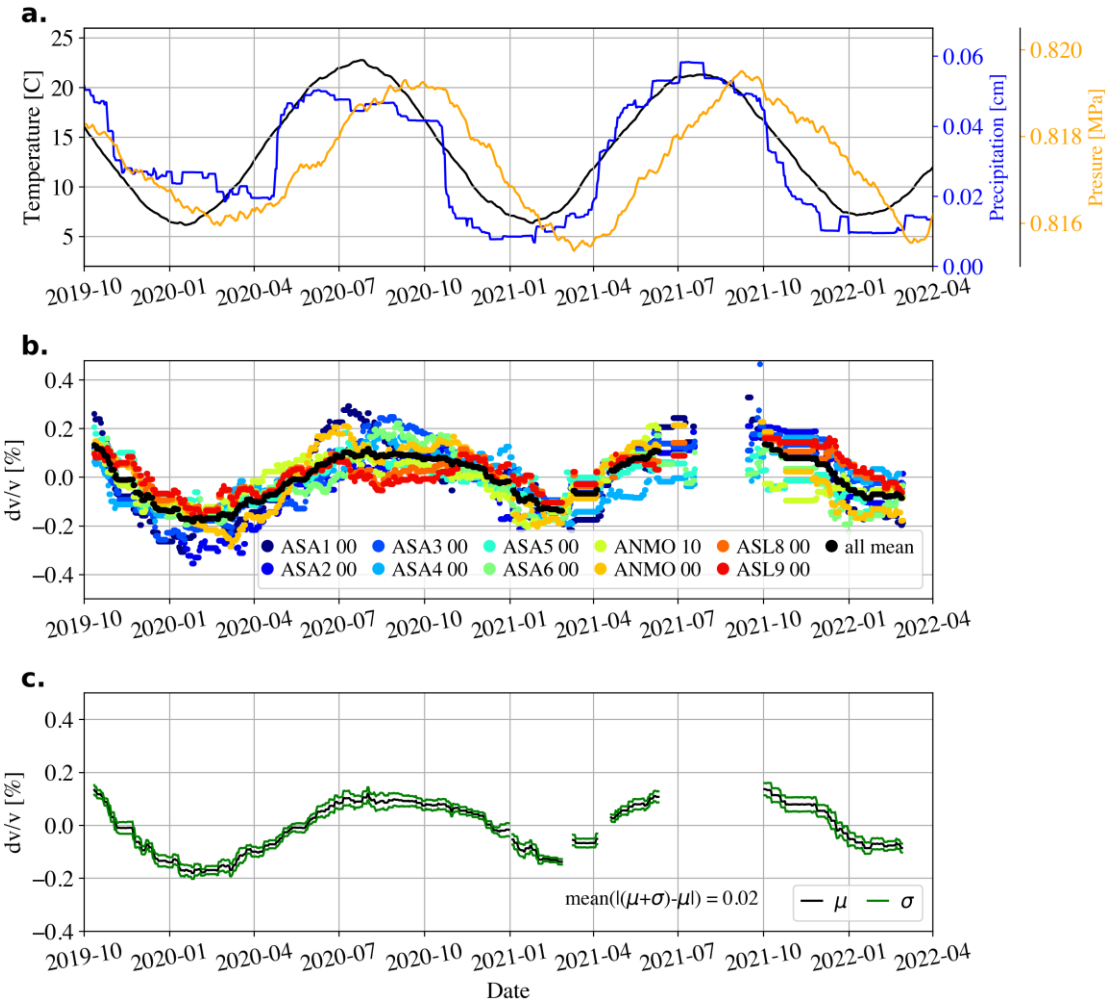

Figure 7. Comparison of velocity changes through time for ASA stations 1 through 8. a) 90 day moving average of precipitation at ASL. b) Velocity variations through time (d*v*/*v*) from the radial component for all ASA array stations. c) Uncertainty of spatial variability from a bootstrap resampling of all measurements in b.

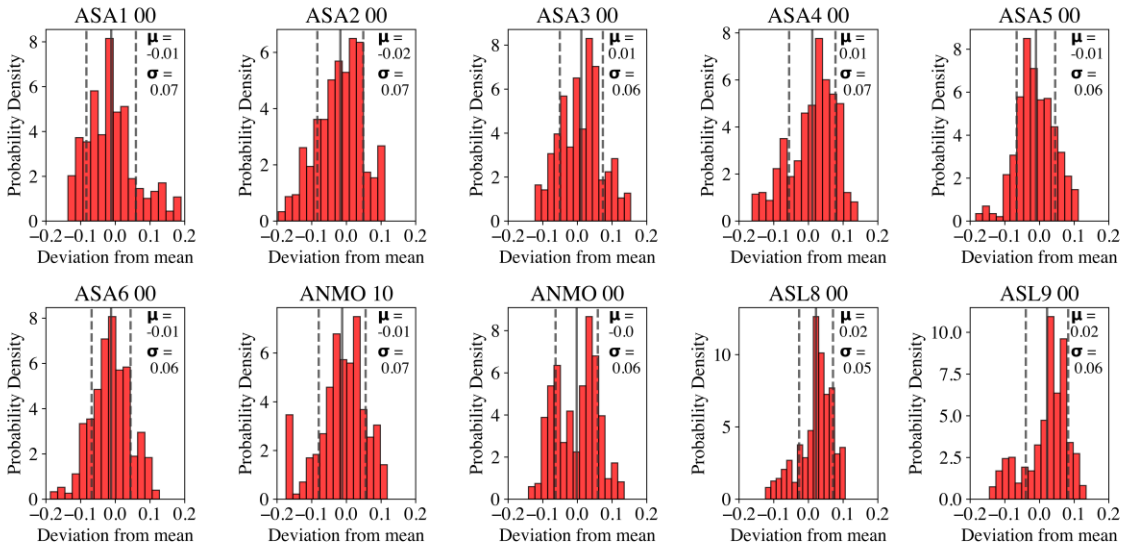

Figure 8. Histogram distributions showing statistics and spatial variability of d*v/v* measurements at each station. Each subplot shows how each station deviates from mean d*v/v* of all stations. The mean (**μ**) and standard deviation (***σ***) are labeled and depicted as solid and dashed lines respectively.

2.6 Discussion

2.6.1 Seismic source and coda

Seismic coda wave observations are primarily sensitive to structure near the source and receiver (e.g., Obermann et al., 2013). Here, we use a single repeating source and small aperture (~600 m) array of receivers. Given the proximity of the receivers, we assume similar geologic and stratigraphic structure, namely a vadose zone dominated by fractured granite, that would respond similarly to poroelastic effects and/or seasonal environmental forcings. Yet, we also acknowledge the potential existence of smaller scale variations that could play an important role in explaining waveform variability within the small aperture array (Figure 3). Z-machine shot recordings show high waveform similarity (mean CC ~0.78) between shots for a given station but lower

interstation waveform similarity for the ballistic and coda arrivals (mean CC ~0.68 and 0.44 respectively). This difference suggests that, while the shot-to-shot characteristics of the late arriving coda change through time due to seasonal oscillations, the waveforms also change over the spatial scale of the ASL array. Considering the fixed source location, we attribute the lower interstation coda CC values to slight variability in receiver side structure between stations on the order of ~100s of meters.

To begin to understand the spatial sensitivity of our d*v/v* measurement and the implications of our results we must first understand the nature of the seismic source signal. Given a dense array of sensors and the presence of a large signal, measurements of d*v/v* can sometimes be made on direct arriving seismic signals if the absolute timing of the source is well-constrained (Mordret et al., 2020). However, sensitivity kernels of direct arrivals are different than those of coda arrivals. As previously stated, scattered waves are highly sensitive to local structure near the source and the receiver, which makes them advantageous when analyzing small-scale spatial variability of d*v/v*. Additionally, scattered waves follow complex paths and consist of both body and surface waves (Obermann et al., 2013; Yuan et al., 2021) making determination of the dominant wave type of the coda wave energy difficult. In the context of spatial variability of d*v/v* understanding relative surface and body wave contributions to Z-machine coda may have little significance but considering this distinction and how it might manifest in *dv/v* signals is important in identification of plausible causes of the seasonal *dv/v* oscillations.

Surface waves are dispersive, so higher frequencies sample shallower crust. The sensitivity of surface wave dominated coda peaks in the shallow crust near the free surface (Obermann et al., 2013; Oakley et al., 2021). Within frequencies typical of ambient noise source based d*v/v* studies (∼0.05 -1.5 Hz) Yuan et al., (2021) find that depending on lag times, surface waves can often dominate coda. However, using ambient noise autocorrelations, which are sensitive to higher frequencies, Kim and Lekic (2019) deduce a strong contribution to the coda from body waves. At 8 Hz, the central frequency of our range, Rayleigh wave sensitivity peaks at ∼35 m depth (e.g., Fores et al., 2018). Assuming simple isotropic structure, Love waves at this frequency would be even more sensitive to shallower < 35 m structure. This contrasts with the ∼0.05-2 Hz frequency band commonly used in ambient noise cross correlation d*v/v* studies, which are sensitive to deeper structure.

Velocities determined from array analysis and relative moveout, along with particle motion behavior (Figure S3 in Appendix 2.A) indicate the initial impulsive Z-machine seismic arrival is a P-wave. Furthermore, several lines of evidence suggest that 4 to 12 Hz energy within the 3-6 s window we use in our *dv/v* analysis is predominantly comprised of scattered body waves as opposed to surface waves. First, we note both lower CC values in the 3-6 s window at each station (Figure 3) and lower array power in this window compared to the initial P-wave arrival (Figure 4b). This contrasts with Anthony et al. (2020), where 1 to 15 Hz surface wave energy from a local earthquake was found to be more coherent across the ASL array than earlier body wave arrivals. Second, array processing indicates that the 3-6 s window contains widely varying

apparent velocities across the array in a range of 5 to 9 km/s (Figure 4d). This is substantially higher than the surface wave velocities (< 4 km/s) previously inferred from local explosions (Anthony et al., 2022c) and cultural noise sources across the ASL array. Third, if the 3-6 s window were dominated by surface wave energy, we would expect exceptional sensitivity to shallow crustal structure surface (Obermann et al., 2013; Oakley et al., 2021) and therefore depth dependent *dv/v* changes at the 90 and 188 m deep ANMO sensors compared to the surface array. However, neither ANMO sensor records *dv/v* measurements that are anomalous from the surface array elements (Figure 8). Lastly, particle motion analysis within the 3-6 s window is inconsistent with surface wave energy (Figure S3 in Appendix 2.A).

2.6.2 Seasonal signal

The magnitude of seasonal signals (0-to-peak) in d*v/v* from coda waves can vary between 0.01 % (Wang et al., 2017) to upwards of 8% (James et al., 2019) depending on the near surface lithology (including water content) and environmental conditions (e.g., freeze-thaw-cycles). Simple thermoelastic and hydrologic models approximate magnitudes of ~ 0.05 % but have known inadequacies associated with poor constraints on Murnaghan's elastic constants in geologic materials (Tsai 2011; Clements and Denolle 2023). Lab studies show magnitudes of ~ 0.1% (Dai et al., 2013) while typical ranges from observational work (excluding studies that are likely recording a liquid-solid phase transition which would have an outsized effect on dv/v, i.e. James et al., (2019) exhibit magnitudes of ~ 0.05-0.2 % (Hillers et al., 2015; Feng et al., 2021; Li et al., 2021;

Mordret et al., 2016; Liu et al., 2020; Oakley et al., 2001). These magnitudes may be underestimates (Yuan et al., 2021) but relative to observational work the ~ 0.2% magnitude seasonal signal in our results is strong.

In tectonically active regions sharp changes in d*v/v* have been attributed to earthquake shaking (e.g., Yang et al., 2022) and volcanic deformation (e.g., Hotovec-Ellis et al., 2022). The neotectonic quiescence of the ASL site relative to the surrounding region (Nakai et al., 2017) rules out a tectonic source. Additionally, clear annual periodicity of the d*v/v* signal suggests an environmental source mechanism. Seasonal fluctuations in environmental processes associated with hydrologic, and thermoelastic processes have been identified as likely candidate mechanisms (Ben-Zion & Leary 1986, Meier et al., 2010). Modeling has identified hydrologic induced stresses would play a larger role than thermoelastic stresses in some environments (Tsai et al., 2011). A less commonly invoked seasonal source mechanism is barometric pressure (Gao et al., 2000, Yang et al., 2019).

Relationships between environmental forcings, their effect on mechanical properties of shallow subsurface structure, and the sensitivity of scattered waves to these changes are complex. A thorough discussion on how they might manifest in a d*v/v* signal are outside of the scope of this paper. Nonetheless, we briefly discuss some first order relationships to deductively explore characteristics and potential origins of the seasonal oscillation in the d*v/v* signal. However, it is possible the oscillation could in fact be a superposition of numerous mechanisms (Clements and Denolle, 2023).

2.6.2.1 Barometric pressure

Lab experiments of crustal rocks have found small stress sensitivities on the order of 1 nPa (Birch, 1960), that decays rapidly with depth. This along with assumed minimal forcing atmospheric pressure variation (∼1 kPa) could enact on crustal rocks, has perhaps kept barometric pressure largely omitted from discussion on origins of seasonal d*v/v* signals. More recent in situ borehole measurements have found stress sensitivity to be much higher 2 x 10^{-7}/Pa (Yang et al., 2019) than lab studies. Even so, the magnitude of travel time delays they find (which are directly related to d*v/v*) are only half the magnitude of our seasonal signal and d*v/v* estimates that have been attributed to atmospheric pressure variation can be an order of magnitude smaller (Gradon et al., 2021). Furthermore, the high rigidity of granite may reduce sensitivity to changes in pressure (Anthony et al., 2022a; Tanimoto and Wang 2020) and in some settings pressure has been found to not play a significant role (Hillers et al., 2014). Because pressure induced stress variations propagate at the speed of a shear wave (Hillers et al., 2015) we should expect near zero phase lag. We find this true in our results (Figure 7). However, the sign is opposite of what might be expected (Silver et al., 2007).

2.6.2.2 Surface temperature

ASL is situated in an arid region where large temperature differentials could exacerbate effects of thermoelastic stresses. This is an important consideration as near surface structure accommodate large thermoelastic stresses (Doody et al., 2018). Average temperature at ASL peaks at ∼22 C during the summer month of August and reach a minimum of ∼6.5 C during the winter month of January ∼1 month ahead of the d*v/v*

signal (Figure 7). This phase lag is within range of the expected ~20-40 day lag (Hillers et al., 2015, Tsai et al., 2011). However, the ~20-40 day lag prediction is dependent on surface waves. A significant body wave contribution, as might be the case, to the d*v/v* measurements could negate this prediction. The depth to which thermoelastic stresses and strains can directly affect material (penetration depth) is wavelength dependent (Hillers and Ben-Zion, 2011, Prawirodirdjo, et al., 2006, Meier et al., 2010). Annual penetration depths of surface temperature vary based on geologic setting. Some studies demonstrate strong attenuation of the thermal affect between 18-80 m (Isaksen et al., 2000; Chapman and Harris, 1993) which should be within range of daily penetration depths. Using a simple conduction model and thermal diffusivity of granite 0.012 cm^2/s (Robertson, 1988), Doody et al., (2018) show that surface temperature variations at the diurnal wavelength are almost entirely attenuated at 40 m depth. However, within a significant body wave contribution paradigm, and considering the 148 meters of material between the 40 m temperature attenuation depth and the 188 m borehole seismometer a simple and direct connection to thermoelastic strain is perhaps unlikely. Modeling the effect of thermoelastic strain on d*v/v* at ASL using the approach from Tsai, (2011) reveals the upper limit 0-to-peak amplitudes to be <= ~0.07 %, nearly 3 times smaller than the amplitude of the observed signal (Figure S4 in Appendix 2.A). Furthermore, if temperature were a dominant driver, we might expect amplitude of the d*v/v* signal to incrementally diminish with depth yet, amplitudes generally agree at the posthole and both the 90 and 180 m borehole sensors (Figure 7). A simple test of the

influence of surface temperature would be to search for diurnal variations (Richter et al., 2014), which is not possible with the supra-daily Z-machine resolution.

2.6.2.3 Precipitation

New Mexico receives 40% of its annual rainfall during monsoon season June 15th through September 30th (Bowen, 1996). Although precipitation can be intense and temporally sporadic, 90-day average of peak precipitation is highly correlated to peak increases in d*v/v* (Figures 6 and 7). There are two hydrologic mechanisms that could contribute to a seasonal signal 1) poroelastic effects and 2) surface loading.

Groundwater levels are often used as an analog for the filling and evacuating of water in pore space (Clements and Denolle, 2018). Although some groundwater wells in in the vicinity of the source and ASL exhibit seasonal recharge-depletion patterns many do not (Bemen et al., 2019). Lack of such a pattern might be expected at a site with complex diffusivity and aquifer depletion or recharge patterns. This could be the case at the ASL, which is situated on the edge of the Albuquerque Basin above fractured granite (Connell, 2001). Seasonality in ground water levels can also be obscured by pumping, drought, and stratigraphic dynamics such as whether the aquifer is confined or not. Therefore, we use precipitation as a hydrologic analog which has demonstrated a reasonable approximation in other settings (Feng et al., 2021; Hillers et al., 2014; Illien et al., 2021).

Modelling how hydrologic fluctuations affect d*v/v* has yielded reasonable fits to observations in both magnitude and phase (Tsai et al., 2011; Sens-Schönfelder & Wegler, 2006; Liu et al., 2020) and it has become common to interpret changes in d*v/v*

within this paradigm (Clements, et al., 2018; Hillers et al., 2014; Almagro et al., 2021). Within a simple aquifer system and assuming surface wave dominated coda, mechanism 1) would fill pore space with water, increase pore pressure and diminish grain contact thereby reducing d*v/v* and mechanism 2) would exert a forcing from a load in the form of accumulation of water in the shallow subsurface which would increase d*v/v*.

Our results show positive correlation: precipitation increases as d*v/v* (and therefore overall seismic velocity) increases. This pattern corresponds to the signal expected with hydrologic loading (Hotovec-Ellis et al., 2014). The low permeability of solid Granite relative to a typical sedimentary basin rock would lead to low diffusivity. Slow diffusion rates could allow for accumulation of meteoric water in the shallow, sediment and fractured granite dominated, subsurface during intense precipitation events. Lenses of water ~7-30 m thick were observed at 70-120 m depths and were documented in the original well logs. Transient lenses of these types at shallower depths could serve as a catchment to facilitate such loading. Furthermore, when modelling the effects of thermoelastic strain, and both hydrologic and loading mechanisms on d*v/v,* Tsai, (2011) identified loading as the most physically reasonable. The positively correlated d*v/v* trend is opposite of what is typically seen when compared to a hydrologic analog in effective percolation settings (Hillers et al. 2014; Feng et al., 2021; Clements and Denolle, 2018). The vadose zone at ASL mostly consists of fractured granite, and strong variability in the roughly estimated 90 m average depth to groundwater level (Figure 1) suggests complex diffusivity and complex aquifer dynamics. Pore space structure can influence poroelastic properties (Shapiro et al., 2015, Pimienta

et al., 2021). Knight et al., (1998) showed that in a patchy saturation environment body wave velocity can increase with saturation. Seismic based studies have also demonstrated positive correlation between body waves and groundwater levels (Garambois et a., 2019; Kim and Lekic, 2019). As previously stated, 4-12 Hz body waves would be more sensitive to deep material at or below the 90 m groundwater depth than surface waves and because there is likely a large body wave contribution to our d*v/v* measurements we consider mechanism 2) a plausible seasonal source. One other possibility in the framework of mechanism 2) could be a percolation regime that supports an almost exact 6-month lag time between precipitation events and groundwater recharge which could be reasonable given a dominantly fractured granite vadose zone and a relatively deep water table. Although there remains ambiguity as to the true origin of the seasonal signal our deductions lead us to prefer a hydrological mechanism driven dominantly by either load or poroelastic variation.

Because loading would have a near instantaneous effect a simple test would be to search for correlation of major precipitation events with d*v/v* excursions. Unfortunately, the Z-machine does not provide sub-daily resolution and is therefore not a great candidate for such a test. Ambient seismic noise may not be as sensitive to the 8 Hz range, but the strong seasonal signal may persist at such frequencies (Illien et al., 2021).

2.6.3 Spatial variability

Some studies have successfully resolved strong seasonal oscillations in d*v/v* using ambient noise cross correlations between sensors with interstation distances > 100 km (Mordret et al., 2018). Analyzing the effect of interstation distance Meier et al., (2010) found that the smallest interstation distances in their study, between 0 and 20 km, produced the clearest seasonal signal. Whereas, Liu et al., (2020) found the shortest interstation distance stations of ∼20 km had the highest variability. Here we extend this line of thought and consider spatial variability between stations with an aperture range of 0.002 – 0.6 km. The small-aperture array of high-quality near-surface sensors at ASL, and the presence of a strong seasonal d*v/v* oscillation on all sensors emanating from a known impulsive repeating cultural source allows for meaningful spatiotemporal analysis.

The consistency in site deployment and location (1.77 m apart) of stations ASL8 and 9 provide a unique opportunity to compare d*v/v* signals while effectively removing the influence of spatial variability. Comparison of the d*v/v* timeseries from these stations are highly similar (Figure 9) with a CC of 0.96 (Figure 10) demonstrating stability of the processing and methodology and providing a benchmark to analyze results from other stations at ASL with larger interstation distances in the context of spatial variability.

Generally, the strong seasonal oscillation in d*v/v* shows spatial consistency on all stations and is strikingly similar among the sensors at ASL (Figure 7). Yet, upon

correlation some systematic variations are revealed that are not likely to arise from measurement of d*v/v* (Figure 9).

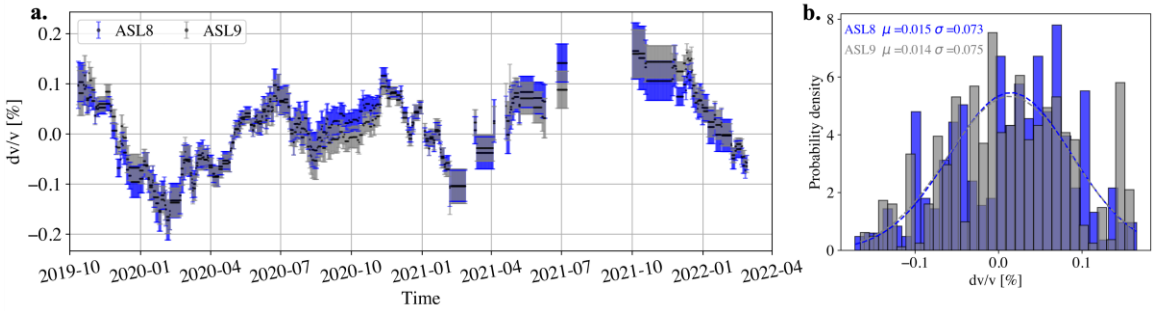

Figure 9. Comparison of d*v/v* measurements for station ASL8 and ASL9. a) Measurements of d*v/v* over 2 years for stations ASL8 (blue) and ASL9 (grey). Error bars are measurement uncertainties calculated during the MWCS step (Clarke et al., 2011). b) Histograms comparing d*v/v* distributions of ASL8 and ASL9. Dashed lines are root mean squared best fit lines. Mean and 1-sigma values are labeled in upper left corner.

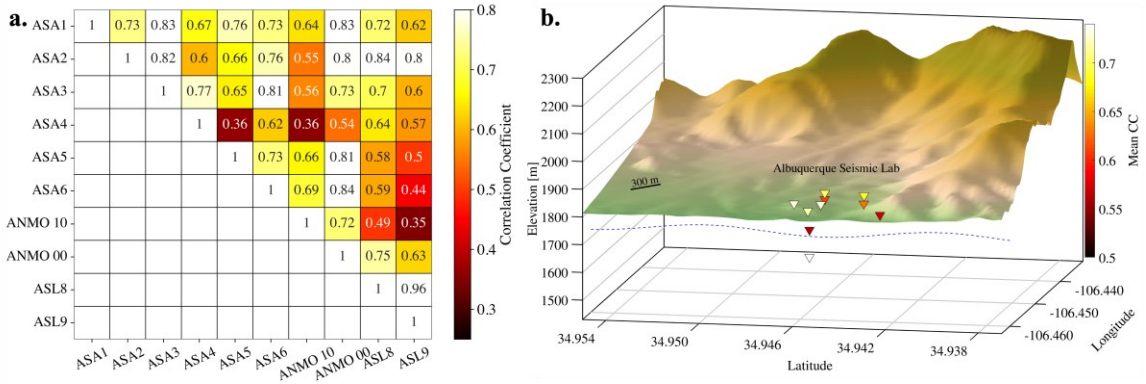

Figure 10. Correlation coefficients of d*v/v* signals from values shown in Figure 7b. a) Correlation matrix for all stations and b) Average station correlations plotted spatially.

From July to November of 2020 both stations ASL8 and ASL9 show an ~ -0.1 % divergence away from the seasonal d*v/v* oscillation which exceeds the .02% average spatial uncertainty (Figure 7c) from bootstrap resampling and is at -1σ in spatial variability (Figure 7). Sensors ASL8 and ASL9 sites are both deployed in ~2.6 m postholes and although the sensors are a different type of instrument (Streckeisen STS-5a and STS-

6) there is no reason to believe that differences in sensor type could be responsible for such an excursion.

Stations ANMO 10 and ASA4 have the lowest mean correlation coefficients while ANMO 00 has the highest (Figure 10). Stratigraphic notes taken during the drilling of the ANMO boreholes indicate ANMO 00 is emplaced within competent granite while ANMO 10 is emplaced in weathered granite within a ∼30 m thick lens of groundwater that is not present at the 188 m depth. The fact that ANMO 10 is directly emplaced in a cased borehole surrounded by groundwater might account for its lower correlation to d*v/v* at other sites. Site ASA4 is the most stratigraphically different of all the posthole stations. It was deployed below a large granite boulder (Anthony et al., (2020), their Figure 2). ASA4 is also the furthest away from the other stations and around the bend of a small hill (Figure 1). Relative to the presumed maximum depth sensitivity of 4-12 Hz scattered waves (∼35 m), 2.6 m is shallow. However, it is well documented that the shallowest material can play a disproportionately large role in the observed signal (Aster et al., 1991). So, it appears that our d*v/v* measurements are sensitive to slight structural variations on the order of 100's of meters laterally. This spatial scale would record ∼ ¼ of the P-wave wavelength which is 687.5 m when using our estimated 5.5 km/s at our central frequency of 8 Hz.

While spatial uncertainty is sometimes shown (Qiu et al., 2020) they are not typically analyzed. This may be due to the assumption that uncertainties are relatively small relative to large divergences in d*v/v* that are temporally coincident with known tectonic and environmental events. That a seemingly spurious 0.1% excursion in d*v/v*

(Figure 9), a magnitude of what is often found in d*v/v* studies, can occur independent of any known source is noteworthy in the context of reliable identification of physical events correlated within dv/v signals.

These results may share overlap with potential d*v/v* studies that use cultural sources such as roads and trains due to the overlap in the frequency range and their independence of annual seasonal variations (Riahi and Gerstoft, 2015; Diaz et al, 2017; Mi et al., 2022; Sheng et al., 2022). The average spatial uncertainty through time of 0.02 % is within range of uncertainties from posterior distribution values (Hillers et al., 2020) and could serve useful for emerging Bayesian methods that invert for d*v/v* and rely on such uncertainties.

It could serve useful to explore if the same strong seasonal signal is resolvable at ASL using ambient noise as a source. Daily resolution of d*v/v* from ambient noise could help resolve smaller period signals (e.g., meteorological events) and may add evidence in support of a hydrologic or thermoelastic mechanism interpretation. Furthermore, the general consistency in our spatial variability results suggest that the array and borehole sensors are well suited for interstation cross correlation. Future d*v/v* work using small-aperture array stations at ASL sites could include single station and interstation correlation methods as well as multichannel and azimuthal analysis (Focker and Ruigrock, 2019) using ambient noise. The results shown here reveal that shallow velocity structure at ASL is broadly varying on the order of a few tenths of a percent at the ASL annually. Exploring implications of such a seasonal signal on shallow velocity structure models and its impact on data quality, not only at ASL but at GSN sites with borehole

sensors could be insightful and might provide complimentary information toward shallow crustal monitoring at GSN stations.

2.7 Conclusion

Using a small-aperture array of high-quality sensors at the ASL and a proximal (12.5 km) impulsive, repeating source we find a strong ~0.2% seasonal signal is broadly present to depths of 188 m and laterally to distances of 600 m. The precise origin of the seasonal signal cannot be determined but a hydrological mechanism emanating from either loading from intense precipitation events or poroelastic variation associated with patchy saturation is possible. Measurements of d*v/v* across ASL deviate ~ +/- 0.1%, half the magnitude of the d*v/v* signal, ~0.2%, indicating clear spatial resolvability in the presence of strong seasonal signals. Therefore, arrays with station spacings < 600 m are well suited for interstation d*v/v* measurement. However, small scale spatial variability is present which could be ambiguously small signals of unknown origin or could be coming from very local changes in structure between stations. Attributing these small-scale variations to local site differences would indicate d*v/v* measurements are sensitive to structure on order of 100's of meters in the 4-12 Hz frequency band. These results could serve useful for emerging techniques such as d*v/v* from cultural noise in similar frequency bands and inversion techniques that require approximations of spatial uncertainty.

2.8 Data and resources

Data and Resources

All seismic data used in this study is available at the IRIS Data Management Center under network code GS: https://doi.org/10.7914/SN/GS and IU: https://doi.org/10.7914/SN/IU. All code used for making figures in this paper will be freely available at: https://github.com/jwilgus/Z_dvv. We relied heavily on the Python library ObsPy (Megies et al., 2011).

The facilities of IRIS Data Services, and specifically the IRIS Data Management Center, were used for access to waveforms, related metadata, and/or derived products used in this study. IRIS Data Services are funded through the Seismological Facilities for the Advancement of Geoscience and EarthScope (SAGE) Proposal of the National Science Foundation under Cooperative Agreement EAR-1261681.

Global Seismographic Network (GSN) is a cooperative scientific facility operated jointly by the Incorporated Research Institutions for Seismology (IRIS), the United States Geological Survey (USGS), and the National Science Foundation (NSF), under Cooperative Agreement EAR-1261681.

2.9 Acknowledgements

We thank Alicia Hotovec-Ellis and Helle Pedersen for early reviews of the abstract of this work as well as Frederik Simons and Bill Harbert for useful discussions at the SAGE-GAGE workshop. We also thank Chengxin Jiang for helpful comments and discussion.

References

Aki, K. (1969). Analysis of the seismic coda of local earthquakes as scattered waves. *Journal of Geophysical Research*, **74**(2), 615-631. https://doi.org/10.1029/JB074i002p00615.

Aki, K., & Chouet, B. (1975). Origin of coda waves: source, attenuation, and scattering effects. *Journal of Geophysical Research*, **80**(23), 3322-3342. https://doi.org/10.1029/JB080i023p03322.

Albuquerque Seismological Laboratory (ASL)/USGS. (1980). *US Geological Survey Networks* [Data set]. International Federation of Digital Seismograph Networks. https://doi.org/10.7914/SN/GS

Albuquerque Seismological Laboratory (ASL)/USGS. (1988). *Global Seismograph Network - IRIS/USGS* [Data set]. International Federation of Digital Seismograph Networks. https://doi.org/10.7914/SN/IU

Almagro Vidal, C., Zaccarelli, L., Pintori, F., Bragato, P. L., & Serpelloni, E. (2021). Hydrological effects on seismic-noise monitoring in karstic media. *Geophysical Research Letters*, **48**(15), e2021GL093191. https://doi.org/10.1029/2021GL093191.

Anthony, R. E., Ringler, A. T., Wilson, D. C., Zebulon Maharrey, J., Gyure, G., Pepiot, A., ... & Voss, N. (2020). Installation and Performance of the Albuquerque Seismological Laboratory Small-Aperture Posthole Array. *Seismological Research Letters*, **91**(4), 2425-2437. https://doi.org/10.1785/0220200080.

Anthony, R. E., Ringler, A. T., Tanimoto, T., Matoza, R. S., De Angelis, S., & Wilson, D. C. (2022). Earth's Upper Crust Seismically Excited by Infrasound from the 2022 Hunga Tonga–Hunga Ha'apai Eruption, Tonga. Seismological Research Letters. https://doi.org/10.1785/0220220252

Anthony, R. E., Ringler, A. T., & Wilson, D. C. (2022b). Seismic Background Noise Levels across the Continental United States from USArray Transportable Array: The Influence of Geology and Geography. *Bulletin of the Seismological Society of America*, **112**(2), 646-668. https://doi.org/10.1785/0120210176.

Anthony, R. E., Watzak, J., Ringler, A. T., & Wilson, D. C. (2022). Characteristics, relationships and precision of direct acoustic-to-seismic coupling measurements from local explosions. Geophysical Journal International, 230(3), 2019-2035. https://doi.org/10.1093/gji/ggac154

Aster, R. C., Shearer, P. M., & Berger, J. (1990). Quantitative measurements of shear wave polarizations at the Anza seismic network, southern California: Implications for shear wave splitting and earthquake prediction. *Journal of Geophysical Research: Solid Earth*, **95**(B8), 12449-12473. https://doi.org/10.1029/JB095iB08p12449.

Aster, R. C., & Shearer, P. M. (1991). High-frequency borehole seismograms recorded in the San Jacinto Fault zone, Southern California Part 2. Attenuation and site effects. *Bulletin of the Seismological Society of America*, **81**(4), 1081-1100. https://doi.org/10.1785/BSSA0810041081.

Astiz, L., Eakins, J. A., Martynov, V. G., Cox, T. A., Tytell, J., Reyes, J. C., ... & Vernon, F. L. (2014). The Array Network Facility seismic bulletin: Products and an unbiased view of United States seismicity. *Seismological Research Letters*, **85**(3), 576-593. https://doi.org/10.1785/0220130141.

Barajas, A., Margerin, L., & Campillo, M. (2022). Coupled body and surface wave sensitivity kernels for coda-wave interferometry in a three-dimensional scalar scattering medium. Geophysical Journal International, 230(2), 1013-1029.https://doi.org/10.1093/gji/ggac091

Beman, J. E., Ritchie, A. B., & Galanter, A. E. (2019). Water-level data for the Albuquerque Basin and adjacent areas, central New Mexico, period of record through September 30, 2017 (No. 1113). US Geological Survey. [Scholar]

Ben-Zion, Y., & Leary, P. (1986). Thermoelastic strain in a half-space covered by unconsolidated material. *Bulletin of the Seismological Society of America*, ***76***(5), 1447-1460. https://doi.org/10.1785/BSSA0760051447.

Birch, F. (1960). The velocity of compressional waves in rocks to 10 kilobars: 1. *Journal of Geophysical Research*, **65**(4), 1083-1102. https://doi.org/10.1029/JZ065i004p01083.

Bonilla, L. F., & Ben-Zion, Y. (2021). Detailed space–time variations of the seismic response of the shallow crust to small earthquakes from analysis of dense array data. *Geophysical Journal International*, *225*(1), 298-310. https://doi.org/10.1093/gji/ggaa544

Bowen, B. M. (1996). Rainfall and climate variation over a sloping New Mexico plateau during the North American monsoon. *Journal of Climate*, **9**(12), 3432-3442. https://doi.org/10.1175/1520-0442(1996)009<3432:RACVOA>2.0.CO;2.

Brenguier, F., Campillo, M., Hadziioannou, C., Shapiro, N. M., Nadeau, R. M., & Larose, E. (2008). Postseismic relaxation along the San Andreas fault at Parkfield from continuous seismological observations. *Science*, **321**(5895), 1478-1481. https://doi.org/10.1126/science.1160943.

Brenguier, F., Rivet, D., Obermann, A., Nakata, N., Boué, P., Lecocq, T., ... & Shapiro, N. (2016). 4-D noise-based seismology at volcanoes: Ongoing efforts and

perspectives. *Journal of Volcanology and Geothermal Research*, **321**, 182-195. https://doi.org/10.1016/j.jvolgeores.2016.04.036.

Busby, R. W., & Aderhold, K. (2020). The Alaska transportable array: As built. *Seismological Society of America*, **91**(6), 3017-3027.https://doi.org/10.1785/0220200154.

Campillo, M., & Paul, A. (2003). Long-range correlations in the diffuse seismic coda. *Science*, **299**(5606), 547-549.https://doi.org/10.1126/science.1078551.

Chapman, D. S., & Harris, R. N. (1993). Repeat temperature measurements in borehole GC-1, northwestern Utah: Towards isolating a climate-change signal in borehole temperature profiles. Geophysical research letters, 20(18), 1891-1894. https://doi.org/10.1029/93GL01877

Clarke, D., Zaccarelli, L., Shapiro, N. M., & Brenguier, F. (2011). Assessment of resolution and accuracy of the Moving Window Cross Spectral technique for monitoring crustal temporal variations using ambient seismic noise. *Geophysical Journal International*, **186**(2), 867-882. https://doi.org/10.1111/j.1365-246X.2011.05074.x.

Clements, T., & Denolle, M. A. (2018). Tracking groundwater levels using the ambient seismic field. *Geophysical Research Letters*, **45**(13), 6459-6465. https://doi.org/10.1029/2018GL077706.

Clements, T., & Denolle, M. A. (2023). The Seismic Signature of California's Earthquakes, Droughts, and Floods. *Journal of Geophysical Research: Solid Earth*, e2022JB025553. https://doi.org/10.1029/2022JB025553

Connell, S. D. (2001). Stratigraphy of the Albuquerque Basin, Rio Grande Rift, central New Mexico: A progress report. *Stratigraphy and Tectonic Development of the Albuquerque Basin, Central Rio Grande Rift. Field-Trip Guidebook for the Geological Society of America, Mini-Papers: Socorro, New Mexico, New Mexico Bureau of Mines and Mineral Resources*, A1-A27. [Scholar].

Dai, S., Wuttke, F., & Santamarina, J. C. (2013). Coda wave analysis to monitor processes in soils. *Journal of Geotechnical and Geoenvironmental engineering*, **139**(9), 1504-1511. http://dx.doi.org/10.1061/(ASCE)GT.1943-5606.0000872

De Plaen, R. S., Cannata, A., Cannavo', F., Caudron, C., Lecocq, T., & Francis, O. (2019). Temporal changes of seismic velocity caused by volcanic activity at Mt. Etna revealed by the autocorrelation of ambient seismic noise. *Frontiers in Earth Science*, **6**, 251. https://doi.org/10.3389/feart.2018.00251.

Díaz, J., Ruiz, M., Sánchez-Pastor, P. S., & Romero, P. (2017). Urban seismology: On the origin of earth vibrations within a city. *Scientific Reports*, **7**(1), 1-11. http://dx.doi.org/10.1061/(ASCE)GT.1943-5606.0000872.

Donaldson, C., Winder, T., Caudron, C., & White, R. S. (2019). Crustal seismic velocity responds to a magmatic intrusion and seasonal loading in Iceland's Northern Volcanic Zone. *Science advances*, *5*(11), eaax6642. https://doi.org/10.1126/sciadv.aax6642.

Doody, C. D., Ringler, A. T., Anthony, R. E., Wilson, D. C., Holland, A. A., Hutt, C. R., & Sandoval, L. D. (2018). Effects of thermal variability on broadband seismometers: Controlled experiments, observations, and implications. *Bulletin of the*

Seismological Society of America, **108**(1), 493-502. https://doi.org/10.1785/0120170233.

Feng, K. F., Huang, H. H., Hsu, Y. J., & Wu, Y. M. (2021). Controls on Seasonal Variations of Crustal Seismic Velocity in Taiwan Using Single-Station Cross-Component Analysis of Ambient Noise Interferometry. *Journal of Geophysical Research: Solid Earth*, **126**(11), e2021JB022650. https://doi.org/10.1029/2021JB022650.

Fokker, E. B., & Ruigrok, E. N. (2019). Quality parameters for passive image interferometry tested at the Groningen network. *Geophysical Journal International*, *218*(2), 1367-1378. https://doi.org/10.1093/gji/ggz228

Fores, B., Champollion, C., Mainsant, G., Albaric, J., & Fort, A. (2018). Monitoring saturation changes with ambient seismic noise and gravimetry in a karst environment. *Vadose Zone Journal*, **17**(1), 1-12. https://doi.org/10.2136/vzj2017.09.0163.

Froment, B., Campillo, M., Roux, P., Gouedard, P., Verdel, A., & Weaver, R. L. (2010). Estimation of the effect of nonisotropically distributed energy on the apparent arrival time in correlations. *Geophysics*, *75*(5), SA85-SA93. https://doi.org/10.1190/1.3483102.

Froment, B., Campillo, M., Chen, J. H., & Liu, Q. Y. (2013). Deformation at depth associated with the 12 May 2008 Mw 7.9 Wenchuan earthquake from seismic ambient noise monitoring. *Geophysical Research Letters*, **40**(1), 78-82. https://doi.org/10.1029/2012GL053995.

Gao, S. S., Silver, P. G., Linde, A. T., & Sacks, I. S. (2000). Annual modulation of triggered seismicity following the 1992 Landers earthquake in California. *Nature*, **406**(6795), 500-504. https://doi.org/10.1038/35020045.

Garambois, S., Voisin, C., Romero Guzman, M. A., Brito, D., Guillier, B., & Réfloch, A. (2019). Analysis of ballistic waves in seismic noise monitoring of water table variations in a water field site: added value from numerical modelling to data understanding. Geophysical Journal International, 219(3), 1636-1647. https://doi.org/10.1093/gji/ggz391

Gradon, C., Brenguier, F., Stammeijer, J., Mordret, A., Hindriks, K., Campman, X., ... & Chmiel, M. (2021). Seismic Velocity Response to Atmospheric Pressure Using Time-Lapse Passive Seismic Interferometry. *Bulletin of the Seismological Society of America*, **111**(6), 3451-3458. https://doi.org/10.1785/0120210069.

Grêt, A., Snieder, R., & Özbay, U. (2006). Monitoring in situ stress changes in a mining environment with coda wave interferometry. *Geophysical Journal International*, **167**(2), 504-508. https://doi.org/10.1111/j.1365-246X.2006.03097.x.

Hable, S., Sigloch, K., Barruol, G., Stähler, S. C., & Hadziioannou, C. (2018). Clock errors in land and ocean bottom seismograms: high-accuracy estimates from multiple-component noise cross-correlations. *Geophysical Journal International*, **214**(3), 2014-2034. https://doi.org/10.1093/gji/ggy236.

Hadziioannou, C., Larose, E., Coutant, O., Roux, P., & Campillo, M. (2009). Stability of monitoring weak changes in multiply scattering media with ambient noise

correlation: Laboratory experiments. *The Journal of the Acoustical Society of America*, **125**(6), 3688-3695.https://doi.org/10.1121/1.3125345.

Hotovec-Ellis, A. J., Gomberg, J., Vidale, J. E., & Creager, K. C. (2014). A continuous record of intereruption velocity change at Mount St. Helens from coda wave interferometry. *Journal of Geophysical Research: Solid Earth*, **119**(3), 2199-2214. https://doi.org/10.1002/2013JB010742.

Hotovec-Ellis, A. J., Shiro, B. R., Shelly, D. R., Anderson, K. R., Haney, M. M., Thelen, W. A., ... & Johanson, I. A. (2022). Earthquake-Derived Seismic Velocity Changes During the 2018 Caldera Collapse of Kīlauea Volcano. *Journal of Geophysical Research: Solid Earth*, **127**(2), e2021JB023324. https://doi.org/10.1029/2021JB023324.

Hillers, G., & Ben-Zion, Y. (2011). Seasonal variations of observed noise amplitudes at 2–18 Hz in southern California. *Geophysical Journal International*, **184**(2), 860-868. https://doi.org/10.1111/j.1365-246X.2010.04886.x.

Hillers, G., Campillo, M., & Ma, K. F. (2014). Seismic velocity variations at TCDP are controlled by MJO driven precipitation pattern and high fluid discharge properties. *Earth and Planetary Science Letters*, **391**, 121-127. https://doi.org/10.1016/j.epsl.2014.01.040.

Hillers, G., Ben-Zion, Y., Campillo, M., & Zigone, D. (2015). Seasonal variations of seismic velocities in the San Jacinto fault area observed with ambient seismic noise. *Geophysical Journal International*, **202**(2), 920-932. https://doi.org/10.1093/gji/ggv151.

Hutt, C. R., Ringler, A. T., & Gee, L. S. (2017). Broadband seismic noise attenuation versus depth at the Albuquerque Seismological Laboratory. *Bulletin of the Seismological Society of America*, **107**(3), 1402-1412. https://doi.org/10.1785/0120160187.

Illien, L., Andermann, C., Sens-Schönfelder, C., Cook, K. L., Baidya, K. P., Adhikari, L. B., & Hovius, N. (2021). Subsurface moisture regulates Himalayan groundwater storage and discharge. *AGU Advances*, *2*(2), e2021AV000398. https://doi.org/10.1029/2021AV000398

Isaksen, K., Mühll, D. V., Gubler, H., Kohl, T., & Sollid, J. L. (2000). Ground surface-temperature reconstruction based on data from a deep borehole in permafrost at Janssonhaugen, Svalbard. Annals of Glaciology, 31, 287-294. https://doi.org/10.3189/172756400781820291

James, S. R., Knox, H. A., Abbott, R. E., & Screaton, E. J. (2017). Improved moving window cross-spectral analysis for resolving large temporal seismic velocity changes in permafrost. *Geophysical Research Letters*, **44**(9), 4018-4026. https://doi.org/10.1002/2016GL072468.

James, S. R., Knox, H. A., Abbott, R. E., Panning, M. P., & Screaton, E. J. (2019). Insights into Permafrost and Seasonal Active-Layer Dynamics from Ambient Seismic Noise Monitoring. *Journal of Geophysical Research: Earth Surface,* **124**(7), 1798-1816. https://doi.org/10.1029/2019JF005051.

Jiang, C., & Denolle, M. A. (2020). NoisePy: A new high-performance python tool for ambient-noise seismology. *Seismological Research Letters*, **91**(3), 1853-1866. https://doi.org/10.1785/0220190364.

Jones, M. C., Ampleford, D. J., Cuneo, M. E., Hohlfelder, R., Jennings, C. A., Johnson, D. W., ... & Porter, J. L. (2014). X-ray power and yield measurements at the refurbished Z machine. *Review of Scientific Instruments*, **85**(8), 083501. https://doi.org/10.1063/1.4891316.

Kim, D., & Lekic, V. (2019). Groundwater variations from autocorrelation and receiver functions. *Geophysical Research Letters*, **46**(23), 13722-13729. https://doi.org/10.1029/2019GL084719.

Knight, R., Dvorkin, J., & Nur, A. (1998). Acoustic signatures of partial saturation. *Geophysics*, **63**(1), 132-138. https://doi.org/10.1190/1.1444305.

Lecocq, T., Caudron, C., & Brenguier, F. (2014). MSNoise, a python package for monitoringseismic velocity changes using ambient seismic noise. *Seismological Research Letters*, **85**(3), 715-726. https://doi.org/10.1785/0220130073.

Li, J., Song, X., Yang, Y., Li, M., Li, J., & Li, Y. (2021). Strong seasonal variations of seismic velocity in eastern margin of Tibetan Plateau and Sichuan Basin from ambient noise interferometry. *Journal of Geophysical Research: Solid Earth*, **126**(11), e2021JB02260 https://doi.org/10.1029/2021JB022600.

Liu, C., Aslam, K., & Daub, E. (2020). Seismic velocity changes caused by water table fluctuation in the New Madrid seismic zone and Mississippi embayment. *Journal of Geophysical Research: Solid Earth*, **125**(8), e2020JB019524. https://doi.org/10.1029/2020JB019524.

Lobkis, O. I., & Weaver, R. L. (2001). On the emergence of the Green's function in the correlations of a diffuse field. *The Journal of the Acoustical Society of America*, *110*(6), 3011-3017. https://doi.org/10.1121/1.1417528

Mayor, J., Margerin, L., & Calvet, M. (2014). Sensitivity of coda waves to spatial variations of absorption and scattering: radiative transfer theory and 2-D examples. *Geophysical Journal International*, **197**(2), 1117-1137. https://doi.org/10.1093/gji/ggu046.

Matzen, M. K., Sweeney, M. A., Adams, R. G., Asay, J. R., Bailey, J. E., Bennett, G. R., ... & Yu, E. P. (2005). Pulsed-power-driven high energy density physics and inertial confinement fusion research. *Physics of Plasmas*, **12**(5), 055503. https://doi.org/10.1063/1.1891746.

Margerin, L., Planès, T., Mayor, J., & Calvet, M. (2016). Sensitivity kernels for coda-wave interferometry and scattering tomography: theory and numerical evaluation in two-dimensional anisotropically scattering media. *Geophysical Journal International*, **204**(1), 650-666. https://doi.org/10.1093/gji/ggv470.

Megies, T., M. Beyreuther, R. Barsch, L. Krischer, and J. Wassermann (2011). ObsPy – What can it do for data centers and observatories? *Annals of Geophysics*, **54**, 47-58. https://doi.org/10.4401/ag-4838.

Meier, U., Shapiro, N. M., & Brenguier, F. (2010). Detecting seasonal variations in seismic velocities within Los Angeles basin from correlations of ambient seismic

noise. *Geophysical Journal International*, **181**(2), 985-996. https://doi.org/10.1111/j.1365-246X.2010.04550.x.

Mi, B., Xia, J., Tian, G., Shi, Z., Xing, H., Chang, X., ... & Zhang, H. (2022). Near-surface imaging from traffic-induced surface waves with dense linear arrays: an application in the urban area of Hangzhou, China. *Geophysics*, **87**(2), B145-B158. https://doi.org/10.1190/geo2021-0184.1.

Moore, S.V., Hutt, C.R., Anthony, R.E., Ringler, A.T., Alejandro, A. & Wilson, D.C. (2018) A Collection of historic antique photos at the Albuquerque Seismological Laboratories, *Seismological Research Letters*, **90**(2A), 765-773, https://doi.org/10.1785/0220180267.

Mordret, A., Mikesell, T. D., Harig, C., Lipovsky, B. P., & Prieto, G. A. (2016). Monitoring southwest Greenland's ice sheet melt with ambient seismic noise. *Science advances*, **2**(5), e1501538. https://doi.org/10.1126/sciadv.1501538.

Mordret, A., Courbis, R., Brenguier, F., Chmiel, M., Garambois, S., Mao, S., ... & Hollis, D. (2020). Noise-based ballistic wave passive seismic monitoring–Part 2: surface waves. Geophysical Journal International, 221(1), 692-705. https://doi.org/10.1093/gji/ggaa016

Nakai, J. S., Sheehan, A. F., & Bilek, S. L. (2017). Seismicity of the rocky mountains and Rio Grande Rift from the EarthScope Transportable Array and CREST temporary seismic networks, 2008–2010. *Journal of Geophysical Research: Solid Earth*, **122**(3), 2173-2192. https://doi.org/10.1002/2016JB013389.

Niu, F., Silver, P. G., Daley, T. M., Cheng, X., & Majer, E. L. (2008). Preseismic velocity changes observed from active source monitoring at the Parkfield SAFOD drill site. *Nature*, **454**(7201), 204-208. https://doi.org/10.1038/nature07111

Oakley, D. O., Forsythe, B., Gu, X., Nyblade, A. A., & Brantley, S. L. (2021). Seismic ambient noise analyses reveal changing temperature and water signals to 10s of meters depth in the critical zone. *Journal of Geophysical Research: Earth Surface*, **126**(2), e2020JF005823. https://doi.org/10.1029/2020JF005823

Obermann, A., Froment, B., Campillo, M., Larose, E., Planès, T., Valette, B., ... & Liu, Q. Y. (2014). Seismic noise correlations to image structural and mechanical changes associated with the Mw 7.9 2008 Wenchuan earthquake. *Journal of Geophysical Research: Solid Earth*, **119**(4), 3155-3168. https://doi.org/10.1002/2013JB010932.

Obermann, A., & Hillers, G. (2019). Seismic time-lapse interferometry across scales. In Advances in geophysics (Vol. 60, pp. 65-143). Elsevier. https://doi.org/10.1016/bs.agph.2019.06.001

Obermann, A., Planes, T., Larose, E., Sens-Schönfelder, C., & Campillo, M. (2013). Depth sensitivity of seismic coda waves to velocity perturbations in an elastic heterogeneous medium. *Geophysical Journal International*, **194**(1), 372-382. https://doi.org/10.1093/gji/ggt043.

Pimienta, L., Quintal, B., & Caspari, E. (2021). Hydro-mechanical coupling in porous rocks: hidden dependences to the microstructure?. *Geophysical Journal International*, **224**(2), 973-984 https://doi.org/10.1093/gji/ggaa497.

Pinzon-Rincon, L., Lavoué, F., Mordret, A., Boué, P., Brenguier, F., Dales, P., ... & Hollis, D. (2021). Humming trains in seismology: an opportune source for probing the shallow crust. Seismological Research Letters, 92(2A), 623-635. https://doi.org/10.1785/0220200248

Poupinet, G., Ellsworth, W. L., & Frechet, J. (1984). Monitoring velocity variations in the crust using earthquake doublets: An application to the Calaveras Fault, California. *Journal of Geophysical Research: Solid Earth*, **89**(B7), 5719-5731. https://doi.org/10.1029/JB089iB07p05719.

Prawirodirdjo, L., Ben-Zion, Y., & Bock, Y. (2006). Observation and modeling of thermoelastic strain in Southern California Integrated GPS Network daily position time series. *Journal of Geophysical Research: Solid Earth*, **111**(B2). https://doi.org/10.1029/2005JB003716.

Qiu, H., Hillers, G., & Ben-Zion, Y. (2020). Temporal changes of seismic velocities in the San Jacinto Fault zone associated with the 2016 M w 5.2 Borrego Springs earthquake. *Geophysical Journal International*, **220**(3), 1536-1554. https://doi.org/10.1093/gji/ggz538.

Reasenberg, P., & Aki, K. (1974). A precise, continuous measurement of seismic velocity for monitoring in situ stress. Journal of Geophysical Research, 79(2), 399-406. https://doi.org/10.1029/JB079i002p00399

Riahi, N., & Gerstoft, P. (2015). The seismic traffic footprint: Tracking trains, aircraft, and cars seismically. *Geophysical Research Letters*, **42**(8), 2674-2681. https://doi.org/10.1002/2015GL063558.

Richter, T., Sens-Schönfelder, C., Kind, R., & Asch, G. (2014). Comprehensive observation and modeling of earthquake and temperature-related seismic velocity changes in northern Chile with passive image interferometry. Journal of Geophysical Research: Solid Earth, 119(6), 4747-4765. https://doi.org/10.1002/2013JB010695

Ringler, A. T., Steim, J., Wilson, D. C., Widmer-Schnidrig, R., & Anthony, R. E. (2020). Improvements in seismic resolution and current limitations in the Global Seismographic Network. *Geophysical Journal International*, **220**(1), 508-521. https://doi.org/10.1093/gji/ggz473.

Rivet, D., Campillo, M., Shapiro, N. M., Cruz-Atienza, V., Radiguet, M., Cotte, N., & Kostoglodov, V. (2011). Seismic evidence of nonlinear crustal deformation during a large slow slip event in Mexico. *Geophysical Research Letters*, **38**(8). https://doi.org/10.1029/2011GL047151.

Robertson, E. C. (1988). Thermal properties of rocks, U.S. Geol. Surv. Open-File Rept. 88-441, 106 pp. https://doi.org/10.3133/ofr88441.

Rodríguez Tribaldos, V., & Ajo-Franklin, J. B. (2021). Aquifer monitoring using ambient seismic noise recorded with distributed acoustic sensing (DAS) deployed on dark fiber. Journal of Geophysical Research: Solid Earth, 126(4), e2020JB021004. https://doi.org/10.1029/2020JB021004

Schweitzer J. Fyen J. Mykkeltveit S., and Kvaerna T. 2002. Seismic arrays, in IASPE New Manual of Seismological Observatory Practice , Bormann P. (Editor), Chapter 9, GeoForschungsZentrum Potsdam, Potsdam, Germany.

Sens-Schönfelder, C., & Wegler, U. (2006). Passive image interferometry and seasonal variations of seismic velocities at Merapi Volcano, Indonesia. *Geophysical research letters*, **33**(21). https://doi.org/10.1029/2006GL027797.

Shapiro, N. M., & Campillo, M. (2004). Emergence of broadband Rayleigh waves from correlations of the ambient seismic noise. Geophysical Research Letters, 31(7). https://doi.org/10.1029/2004GL019491

Shapiro, S. A., Khizhniak, G. P., Plotnikov, V. V., Niemann, R., Ilyushin, P. Y., & Galkin, S. V. (2015). Permeability dependency on stiff and compliant porosities: a model and some experimental examples. *Journal of Geophysics and Engineering*, *12*(3), 376-385. https://doi.org/10.1088/1742-2132/12/3/376.

Sheng, Y., Mordret, A., Sager, K., Brenguier, F., Boué, P., Rousset, B., ... & Ben-Zion, Y. (2022). Monitoring Seismic Velocity Changes Across the San Jacinto Fault Using Train-Generated Seismic Tremors. Geophysical Research Letters, 49(19), e2022GL098509. https://doi.org/10.1029/2022GL098509

Silver, P. G., Daley, T. M., Niu, F., & Majer, E. L. (2007). Active source monitoring of cross-well seismic travel time for stress-induced changes. *Bulletin of the Seismological Society of America*, **97**(1B), 281-293. https://doi.org/10.1785/0120060120.

Sinars, D. B., Sweeney, M. A., Alexander, C. S., Ampleford, D. J., Ao, T., Apruzese, J. P., ... & Sandoval, D. (2020). Review of pulsed power-driven high energy density physics research on Z at Sandia. *Physics of Plasmas*, **27**(7), 070501. https://doi.org/10.1063/5.0007476.

Snieder, R., Grêt, A., Douma, H., & Scales, J. (2002). Coda wave interferometry for estimating nonlinear behavior in seismic velocity. *Science*, **295**(5563), 2253-2255. https://doi.org/10.1126/science.1070015.

Snieder, R. (2004). Extracting the Green's function from the correlation of coda waves: A derivation based on stationary phase. *Physical review E*, *69*(4), 046610. https://doi.org/10.1103/PhysRevE.69.046610

Snieder, R. (2006). The theory of coda wave interferometry. *Pure and Applied Geophysics*, **163**(2), 455-473. https://doi.org/10.1007/s00024-005-0026-6.

Snieder, R., Wapenaar, K., & Larner, K. (2006). Spurious multiples in seismic interferometry of primaries. *Geophysics*, ***71***(4), SI111-SI124. https://doi.org/10.1190/1.2211507.

Stairs, R. K., Schmandt, B., Townsend, J. P., & Wang, R. (2023). The Seismic Signature of a High-Energy Density Physics Laboratory and Its Potential for Measuring Time-Dependent Velocity Structure. *Seismological Research Letters*. https://doi.org/10.1785/0220220283

Stehly, L., Campillo, M., & Shapiro, N. M. (2006). A study of the seismic noise from its long-range correlation properties. *Journal of Geophysical Research*, **111**(B10). https://doi.org/10.1029/2005JB004237.

Taira, T. A., Nayak, A., Brenguier, F., & Manga, M. (2018). Monitoring reservoir response to earthquakes and fluid extraction, Salton Sea geothermal field, California. *Science advances*, **4**(1), e1701536. https://doi.org/10.1126/sciadv.1701536.

Taylor, G., & Hillers, G. (2020). Estimating temporal changes in seismic velocity using a Markov chain Monte Carlo approach. *Geophysical Journal International*, **220**(3), 1791-1803. https://doi.org/10.1093/gji/ggz535.

Tsai, V. C. (2011). A model for seasonal changes in GPS positions and seismic wave speeds due to thermoelastic and hydrologic variations. *Journal of Geophysical Research: Solid Earth*, **116**(B4). https://doi.org/10.1029/2010JB008156.

Ueno, T., Saito, T., Shiomi, K., Enescu, B., Hirose, H., & Obara, K. (2012). Fractional seismic velocity change related to magma intrusions during earthquake swarms in the eastern Izu peninsula, central Japan. *Journal of Geophysical Research: Solid Earth*, **117**(B12). https://doi.org/10.1029/2012JB009580.

VanDecar, J. C., & Crosson, R. S. (1990). Determination of teleseismic relative phase arrival times using multi-channel cross-correlation and least squares. *Bulletin of the Seismological Society of America*, **80**(1), 150-169. https://doi.org/10.1785/BSSA0800010150.

Vernon, F. L., Pavlis, G. L., Owens, T. J., McNamara, D. E., & Anderson, P. N. (1998). Near-surface scattering effects observed with a high-frequency phased array at Pinyon Flats, California. *Bulletin of the Seismological Society of America*, **88**(6), 1548-1560. https://doi.org/10.1785/BSSA0880061548.

Wang, Q. Y., Brenguier, F., Campillo, M., Lecointre, A., Takeda, T., & Aoki, Y. (2017). Seasonal crustal seismic velocity changes throughout Japan. *Journal of Geophysical Research: Solid Earth*, **122**(10), 7987-8002 https://doi.org/10.1002/2017JB014307.

Wang, Q. Y., Campillo, M., Brenguier, F., Lecointre, A., Takeda, T., & Hashima, A. (2019). Evidence of changes of seismic properties in the entire crust beneath Japan after the M w 9.0, 2011 Tohoku-oki earthquake. *Journal of Geophysical Research: Solid Earth*, **124**(8), 8924-8941. https://doi.org/10.1029/2019JB017803.

Wang, Q. Y., & Yao, H. (2020). Monitoring of velocity changes based on seismic ambient noise: A brief review and perspective. *Earth and Planetary Physics*, **4**(5), 532-542. https://doi.org/10.26464/epp2020048.

Wegler, U., Lühr, B. G., Snieder, R., & Ratdomopurbo, A. (2006). Increase of shear wave velocity before the 1998 eruption of Merapi volcano (Indonesia). *Geophysical Research Letters*, **33**(9). https://doi.org/10.1029/2006GL025928.

Wegler, U., & Sens-Schönfelder, C. (2007). Fault zone monitoring with passive image interferometry. *Geophysical Journal International*, **168**(3), 1029-1033. https://doi.org/10.1111/j.1365-246X.2006.03284.x.

Yang, C., Niu, F., Daley, T. M., & Taira, T. A. (2019). Continuous measurement of stress-induced travel-time variations at SAFOD. *Seismological Research Letters*, **90**(1), 212-218. https://doi.org/10.1785/0220180080.

Yang, Z., Yuan, C., & Denolle, M. A. (2022). Detecting Elevated Pore Pressure due to Wastewater Injection Using Ambient Noise Monitoring. *The Seismic Record*, **2**(1), 38-49. https://doi.org/10.1785/0320210036.

Yuan, C., Bryan, J., & Denolle, M. (2021). Numerical comparison of time-, frequency-and wavelet-domain methods for coda wave interferometry. *Geophysical Journal International*, **226**(2), 828-846. https://doi.org/10.1093/gji/ggab140.

Zhan, Zhongwen, Victor C. Tsai, and Robert W. Clayton. (2013). "Spurious velocity changes caused by temporal variations in ambient noise frequency content." *Geophysical Journal International* **194**(3),1574-1581. https://doi.org/10.1093/gji/ggt170.

Appendix

2.A Supplementary figures

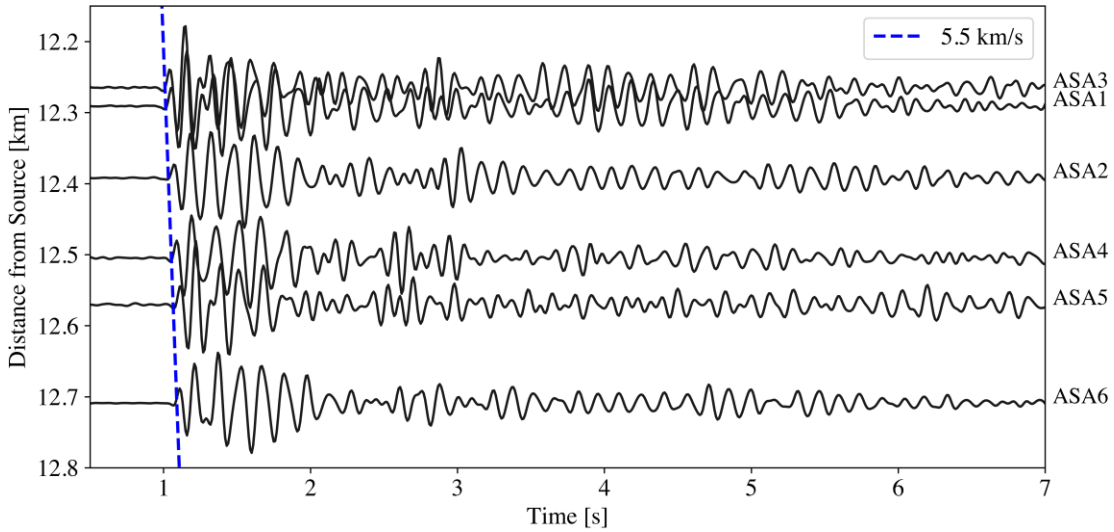

Figure S1. Z-machine event stacks. Each trace is a radial component stack of events aligned around detection times for each ASA station as labeled. Traces are placed at their respective distances from the Z-source location. The same ANMO detection times were used to request data for each station, so plotting each stack as a function of distance forms a relative moveout. Tracking the initial arrival shows an apparent velocity of ~5.5 km/s.

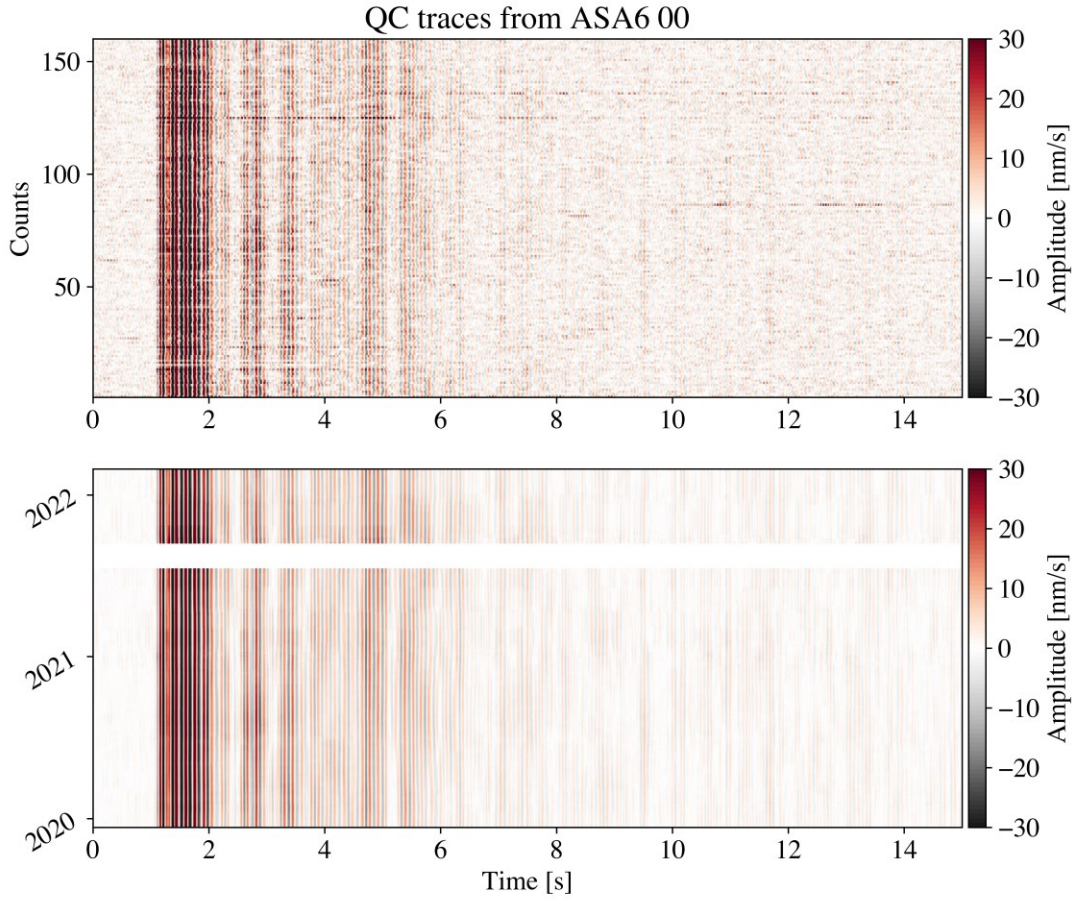

Figure S2. Top panel shows post quality control and multi-component two step alignment organized by count. Bottom panel shows post 90-day moving average organized by time from 2020 to 2022.

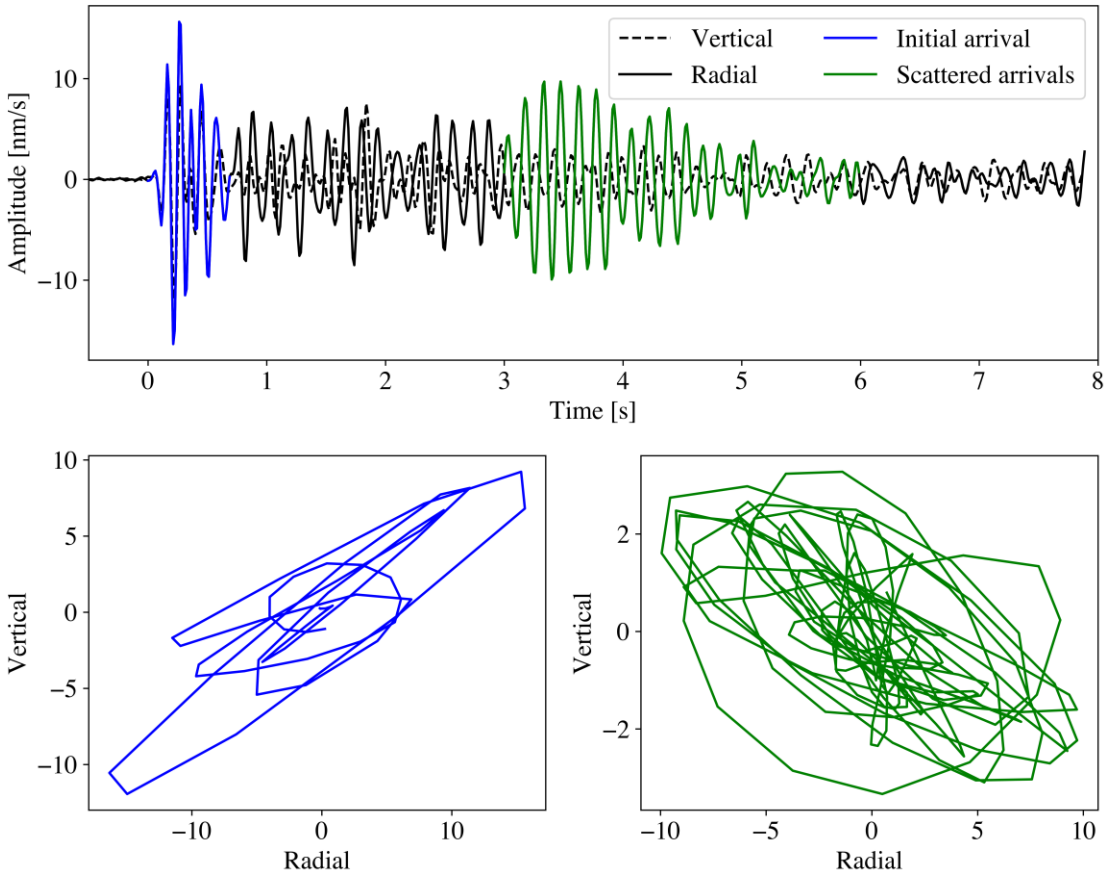

Figure S3. Particle motion of the initial impulsive ballistic arrival (blue) and later arriving coda (green) from station ANMO 10.

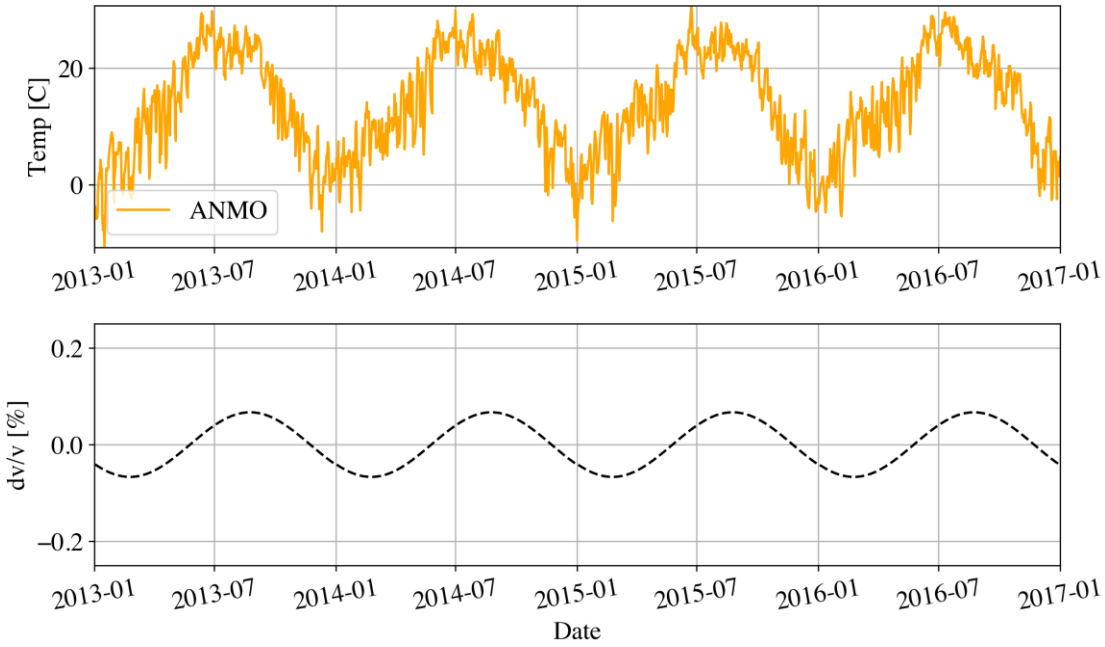

Figure S4. Surface temperature and thermoelastic modelling of d*v/v* at ASL. Top panel shows surface temperature from ANMO weather station. Bottom panel shows d*v/v* from thermoelastic strain modelled with equations from Tsai, 2011 using parameters representative of ASL (i.e., a half annual peak-to-peak mean surface temperature variation of 15° C and a depth of 0.5 m) that approximate the upper limit potential of d*v/v* amplitude.

3 Background Seismic Noise Levels Among the Caribbean Network and the Role of Station Proximity to Coastline

Authors and affiliations

Justin Wilgus[1,2]*

Adam Ringler[1]

Brandon Schmandt[2]

Robert Anthony[1]

Dave Wilson[1]

[1]U.S. Geological Survey, Albuquerque Seismological Laboratory, Albuquerque, NM, USA

[2]University of New Mexico, Department of Earth & Planetary Sciences, Albuquerque, NM, USA

∗Corresponding author

3.1 Abstract

The amplitude and frequency content of background seismic noise is highly dependent on geographic location. Understanding the characteristics and behavior of background seismic noise as a function of location can inform approaches to improve network performance and increase earthquake detection capabilities. Here we calculate power spectral density (PSD) estimates in one-hour windows for over 15 years of vertical component data from the nine-station Caribbean network (CU) and look at background noise within the 0.05-300 s period range. We describe the most discernable first order signals observed at the CU stations. One of the most prominent signals occurs in the 0.75-3 s band where power levels are systematically elevated and decay as a function of

proximity to coastline. Further examination of this band on 1679 contiguous US Transportable Array stations reveals the same relationship. Such a relationship with coastal distance is not observed in the 4-8 s range more typical of globally observed secondary microseisms. A simple surface wave amplitude decay model fits the observed decay well with geometric spreading as the most important factor for stations near the coast (< ~ 50 km). The model suggests that at 0.75–3 s, power levels are strongly influenced by proximity to coastline. This may be because at 0.75–3 s, power from nearshore wave action overwhelms more distant and spatially distributed secondary microseism generation. Application of this basic model indicates that a power reduction of ~25 dB can be achieved by simply installing the seismometer 25 km away from the coastline. This finding may help to inform future site locations and array design thereby improving network performance and data quality, and subsequently earthquake detection capabilities.

3.2 Introduction

The field of observational seismology depends on the accurate measurement of both the amplitude and arrival time of energy across the entire seismic frequency band. Seismic records with high noise can compromise our ability to measure ground motion and obscure our ability to record other signals of interest (Steim, 2015). Estimating the power spectral density (PSD) of seismic timeseries is a convenient way to look at background noise across the entire frequency band.

At short periods (e.g., <1 s), low background noise levels are important for reducing local earthquake magnitude detection thresholds (Wang et al., 2020; Wilson et

al., 2021; 0.04 s to 1 s). Yet, the noise levels at these frequencies can be dominated by cultural and environmental signals (Anthony et al, 2018; Marcillo & Carmichael, 2018; Smith & Tape, 2019; Lecocq et al., 2020; Anthony et al., 2022). At intermediate periods (∼1-20 s), noise levels can limit our ability to detect teleseismic earthquakes. Station noise levels at these periods are often dominated by the secondary and primary microseisms that emanate from ocean wave-wave and wave-continental shelf interactions, respectively (Gutenberg, 1936; Longuet-Higgins, 1950; Gualtieri et al., 2020). These signals are routinely used as a source for observational studies of the lithosphere (Sabra et al., 2005; Moschetti et al., 2007; Lin et al., 2008). At longer periods (>30 s), the minimum of Earth's background noise levels is limited by Earth hum which is the excitation of Earth's natural frequencies from atmospheric disturbances (Webb et al., 2008; Maurya et al., 2019) and large earthquakes. These long period excitations are quite useful for interrogating Earth's deep interior, such as the core (Dziewonski & Gilbert 1971; Robson & Romanowicz, 2019). These are just a few examples to demonstrate the important interplay between background noise levels and seismic signals of interest across the inherently broadband seismic wavefield.

There are several studies that demonstrate 1) the impact cultural activities, seasonal weather patterns, and other phenomena can have on seismic background noise levels (Peterson, 1993; McNamara & Buland, 2004; Lecocq et al., 2020; Anthony et al., 2022; Ringler et al. 2023) and 2) the importance of trying to understand and mitigate the impact of environmental noise sources on seismic records (Doody et al. 2018; Dybing et al., 2019; Ringler et al., 2020a; Janiszewski et al., 2023). Such work requires understanding

the physical processes generating the seismic noise (Holcomb, 1998; Shapiro et al., 2006; Rhie & Romanowicz, 2004; McNamara et al., 2011; Tsai et al., 2011; Koper & Burlacu, 2015; Anthony et al., 2018; Fan et al., 2019; Diaz et al., 2023a) but can also be motivated by a goal of improving quality of ground motion records by isolating stations from these known sources. The USArray Transportable Array (TA, Meltzer et al., 1999) stations in the contiguous US (L48; Busby et al., 2018) and Alaska (Busby et al., 2020) provided a large amount of data, with uniform installations, which allowed for a better understanding of background noise levels as a function of geographic location (Anthony et al., 2022; Ringler et al., 2023). In the L48, geography, cultural activity, and material in which sensor is deployed (local geology) appear to play the largest role in background noise levels. In Alaska, fluctuations in sea ice and the magnetic field (Ringler et al., 2020b) influence background noise recordings, while lack of cultural activity relative to the L48 produces significantly lower noise levels at periods below $\sim$1 s. The differences between these studies highlight the regional and site-specific variation that can exist in background noise. Here, we use the approaches taken in Anthony et al. (2022) and Ringler et al. (2023) to assess the background noise levels of the Albuquerque Seismological Laboratory (ASL)/U.S. Geological Survey (2006) Caribbean Seismic Network (CU, Figure 1) which makes up a component of the Global Seismographic Network (GSN).

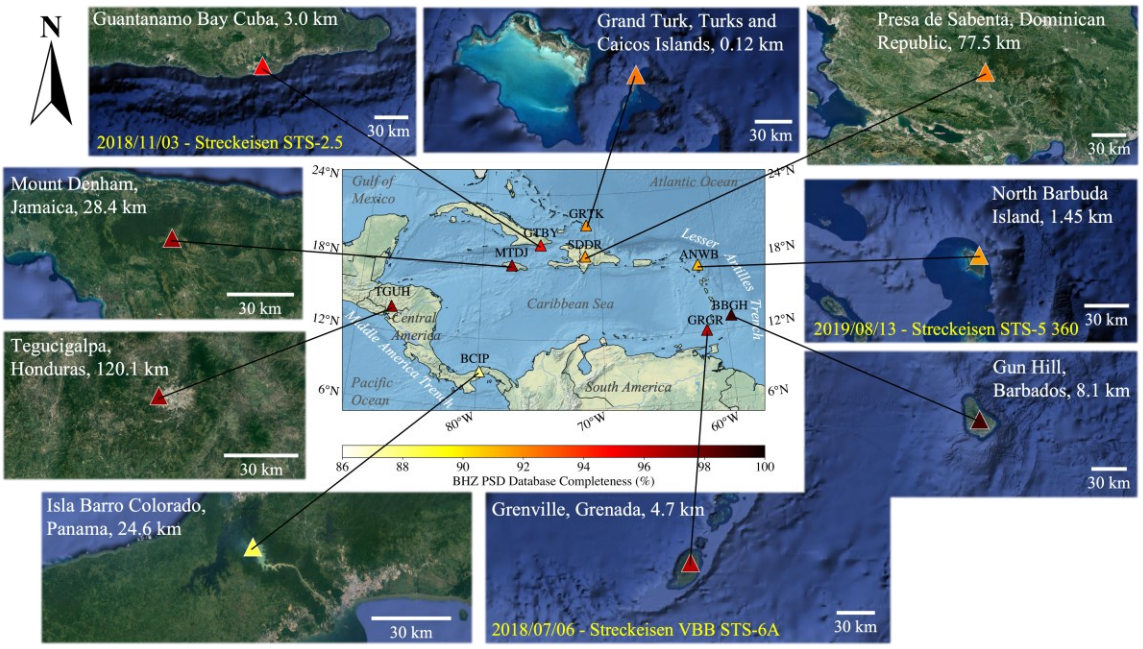

Figure 1. Relief map of CU network region, data completeness, and satellite imagery of each station. Each triangle in the center inset is a seismic station labeled by name. The color of each triangle represents completeness of data as a percentage since the deployment of each station. The location and distance to the nearest beach are noted in the upper left in white. Every station initially hosted a Streckeisen STS-2 seismic sensor, but a few have since been upgraded which is noted in yellow on the satellite image. The Caribbean Sea and Gulf of Mexico are labeled accordingly as well as major subduction trenches (Middle America and Lesser Antilles), geographic regions (Central and South America), and oceans (Atlantic and Pacific).

The Caribbean region, roughly defined here as the area within and surrounding the Caribbean Plate, differs from Alaska and the lower 48 in that it is comprised mainly of ocean (Caribbean Sea) rather than land mass, and is bounded by active tectonics and plate boundaries (Middle America and lesser Antilles trench; Braszus et al., 2021), which contributes to a complex bathymetry pattern that has potential to influence the primary and secondary microseism (Gualtieri et al., 2020; Le Pape et al., 2021). Much work has been done to characterize the amplitude and source mechanisms of the primary and secondary microseisms (Ardhuin et al., 2015; Koper & Burlacu, 2015). However, the

relative contribution of nearshore energy from local sea and direct breaking beach waves to seismic noise levels has not been explored in as much detail. Direct breaking beach waves generate short period (∼0.06–0.2 s) and intermediate period (1–10 s) energy which can be exacerbated during storms (Gutenberg, 1958; Bromirski, et al., 2005 Poppeliers & Mallinson, 2015). During a nominal storm event (15 m/s wind speeds and 4 m wave heights) energy from apparent direct crashing beach waves demonstrated a peak power near ∼ –100 dB (rel. 1 $(m/s)^2$/Hz) at ∼1 s period 50 m off the coast of North Carolina (Poppeliers & Mallinson, 2015). Such local beach energy shares overlap with the frequency content of teleseismic body waves (∼1–15 s, Bormann et al., 2013; Benz & Herrmann, 2014). Importantly, seismic stations typically have relatively low noise around 1 s period due to a "noise trough" between shorter period cultural noise and longer-period (∼3 to 10 s, Ardhuin et al., 2015) secondary microseisms (Anthony et al., 2022). Therefore, shorter period energy generated by breaking swell could compromise the fidelity of teleseismic body wave observations at near-coastal seismic stations. Furthermore, although a peak period of 1 s (apparent beach energy) would share some overlap with distant generated secondary microseism peak period (Gutenberg, 1958), it is lower than what is observed on average globally (∼5 s; Peterson, 1993) and lower than what might be physically possible for secondary microseism generation mechanisms (Kedar et al., 2008; Ardhuin et al., 2011; Ardhuin et al., 2015).

The CU network was initially developed to aid in Tsunami warnings (McNamara et al, 2006) and was incorporated into the GSN for geologic hazard monitoring, which is particularly important in tectonically active, high seismic hazard regions such as the

Caribbean (McCann, 1985; Shedlock, 1999; DesRoches et al., 2011; McNamara et al., 2016; Torpey Zimmerman et al., 2022; Cordrie et al., 2022). The CU has since evolved to serve as a multi-use observatory for research and outreach. Background noise analysis of the Caribbean region using the CU network provides an opportunity to characterize and better understand the dominant signals in this this unique, high seismic hazard geographic region and examine the relationship between power and station proximity-to-coastline.

3.3 Data and methods

The CU consists of 9 broadband 3 component Streckeisen STS-2 seismometers that are recorded on Quanterra Q330 HR digitizers. Most stations were initially deployed in a vault similar to L48 TA but using a smaller footprint (Figure S1 in Appendix 3.A; Busby et al., 2020). Stations were deployed between 2006 and 2007 and have been continuously recording with occasional downtime (Figure 1). Stations GTBY (Guantanamo Bay, Cuba), ANWB (North Barbuda Island), and GRGR (Grenville, Grenada) all received sensor updates between 2018 and 2019.

While there are numerous seismic stations in the Caribbean region many are lower quality Raspberry Shake citizen science sensors (Anthony et al., 2019) or are limited in temporal resolution (e.g., specific scientific targeted deployments). Some higher quality long-term monitoring networks in the Caribbean include the Geological Survey network in Haiti and Puerto Rico (PR; installed by the USGS), the Caribbean Netherlands Network (NA), West Indies French Seismic Network (WI), and the Eastern

Caribbean Seismograph Network (TR), but are limited by their specific locations relative to the Caribbean region. Perhaps the most substantial seismic entity in the Caribbean is the intergovernmental coordination group on Tsunami and other Coastal Hazards Early Warning System for the Caribbean and Adjacent Regions (CARIBE-EWS) to which > 100 seismic stations from nearly every Caribbean nation contribute (McNamara et al., 2016). Numerous networks with varying seismic sensor types and deployment styles contribute data to CARIBE-EWS including networks operated by ASL, such as the CU and three GSN stations in the region (SDV, Santo Domingo, Venezuela; SJG San Juan, Puerto Rico; TEIG Tepich, Yucatan, Mexico). For the purposes of this work we focus strictly on examining performance of a region-specific network in a unique geographic location, the CU, of similar sensors and installations in diversely localized settings.

To calculate PSDs through time we follow the general methodology of McNamara and Buland (2004) but omit any smoothing or binning of the PSD estimates (Anthony et al., 2020). We use the exact same processing parameters as Anthony et al. (2022) and Ringler et al. (2023), calculating PSDs every hour with a half overlapping (30 minute) window step. We divide each hour of data into 14 sub-segments with 75% overlap and implement the Welch method (Welch, 1967), i.e., employing the discrete Fourier transform to each sub-window and taking the average, to attain PSD estimates for each window. The instrument response is then removed, and the results are converted to dB relative to 1 $(m/s^2)^2$/Hz. We apply this approach to all available (through Jan. 1st 2023) broadband vertical channel BHZ data which is recorded at 40 samples-per-second and focus on the 0.05–300 s band. As a quality control step, we do

not calculate the PSD if less than 90% of the data is available for each one-hour segment.

3.4 Results

Regular maintenance of the CU network has resulted in fairly consistent uptime for each of the CU stations. Data completeness is above 90% for all stations except for BCIP (∼86%; Isla Barro Colorado, Panama) which experienced extended downtime between 2020 and 2021 during which COVID-19 restrictions limited travel for on-site station maintenance (Figure 1).

Figure 2 shows plots of PSD probability density functions (PDF) for each CU station. To first order, background noise levels of the CU stations demonstrate a wide range of variability between stations. This is particularly true at periods below ∼4 s (Figure 2). There are many features within the background noise of each CU station that could be described. Here we focus on characterizing a few of the most prominently discernable features. We then attempt to identify a few anthropogenic and physical mechanisms that could be contributing to the observed signals, and subsequently explore how such signals could impact network performance and data quality.

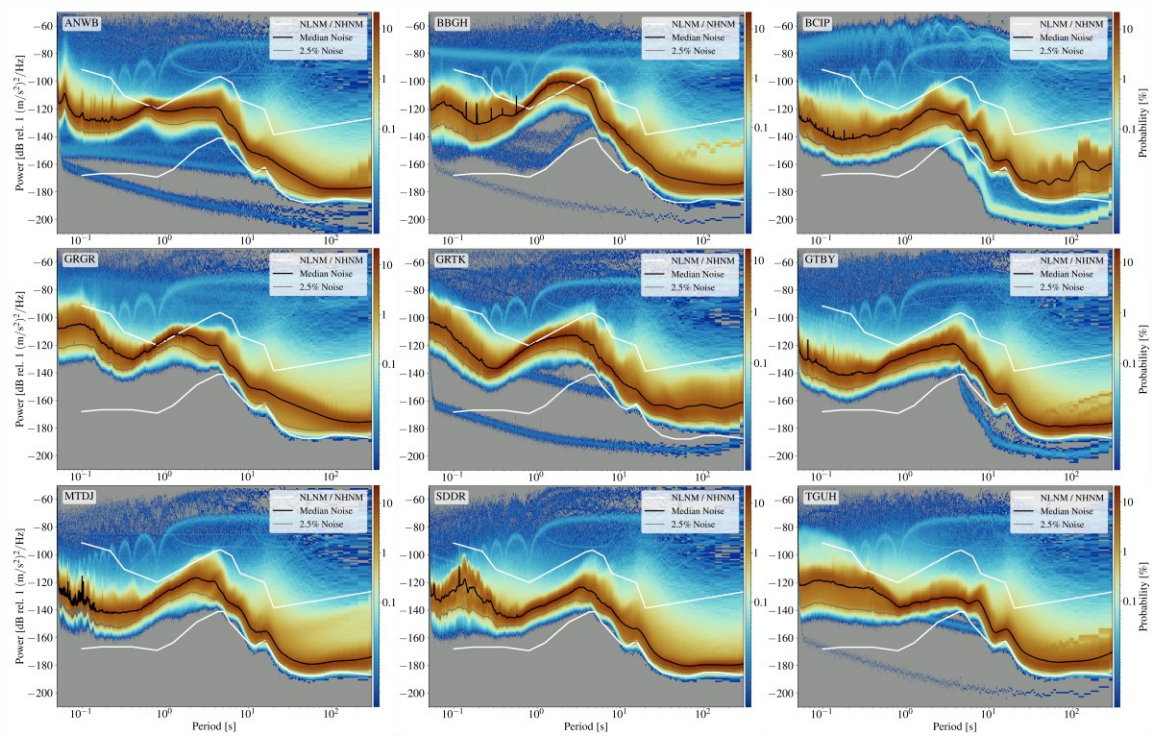

Figure 2. Power spectral density (PSD) probability densities of every other PSD for each CU station. Color bars show probability density in percent. Each station is labeled in the upper left-hand corner of each panel. Every station has a different number of total PSDs and therefore a unique, albeit similar, colorbar range. The Peterson (1993) New Low-/High-Noise Model (NLNM/NHNM) models are shown in each panel as white lines. Median and 2.5th percentile from all PSDs for each station are shown as black and green lines respectively.

The highest density regions (> ~1%) and the median PSD for each station generally fall within the Peterson (1993) New Low-/High-Noise Model (NLNM/NHNM) range except within the ~0.75–4 s period band where stations ANWB, BBGH (Gun Hill, Barbados), GRGR, and GRTK (Grand Turk, Turks and Caicos Islands) show elevated power above the NHNM (Figure 2). At the shortest periods of the spectrum (< ~1 s) individual station PSD PDFs demonstrate a wide range of variability in power. In particular, stations MTDJ (Mount Denham, Jamaica), SDDR (Persa de Sabenta, Dominican Republic), and TGUH (Tegucigalpa, Honduras) demonstrate intriguing power characteristics in the short period range below 1 s. Station MTDJ shows an ensemble of elevated power peaks in the 0.06

to 0.15 s range with the largest median power level peak of ~ –115 dB focused around 0.1 s. Station TGUH shows broad (no major peaks) and consistently elevated power below ~ 0.5 s with a wide power level distribution between ~ –140 and –110 dB. This wide power range is further demonstrated by the ~20 dB difference between the median and the 2.5th percentile noise levels. Lastly, station SDDR shows a single large, elevated power peak between 0.07 and 0.3 s. The maximum peak occurs at ~0.15 s where it demonstrates a wide range of power with the highest density power regions between ~ –140 and –100 dB.

Within the primary and secondary microseism range, relative power between stations ranges between ~ –120 and –140, and ~ –145 to –165 dB, respectively (Figure 2). In terms of power the primary and secondary microseism period range show more agreement between CU stations than at shorter and longer periods (Figure 2 and 3). However, the shape and prominence of the secondary and primary microseism peaks are still somewhat variable. Station TGUH shows pronounced primary and secondary microseism peaks, whereas such peaks are non-existent or obscured on stations GRTK and BBGH.

At long periods (~ 50–300 s) median CU station power levels range between ~ –180 and –170 dB, except for stations of BCIP and GRTK which demonstrate elevated power levels in the range of ~ –165 to –160 dB.

The most variable and elevated power levels, when examining station and network medians, occur in the 0.75–3 s band. This consistently elevated power is clearly demonstrated when comparing the median power of all CU stations with the median

power of all L48 TA stations (Figure 3) and occurs below the typical secondary microseism peaks and within range of typical teleseismic event spectra (~1–15 s). Explaining this elevated power signal is an important focus of the discussion.

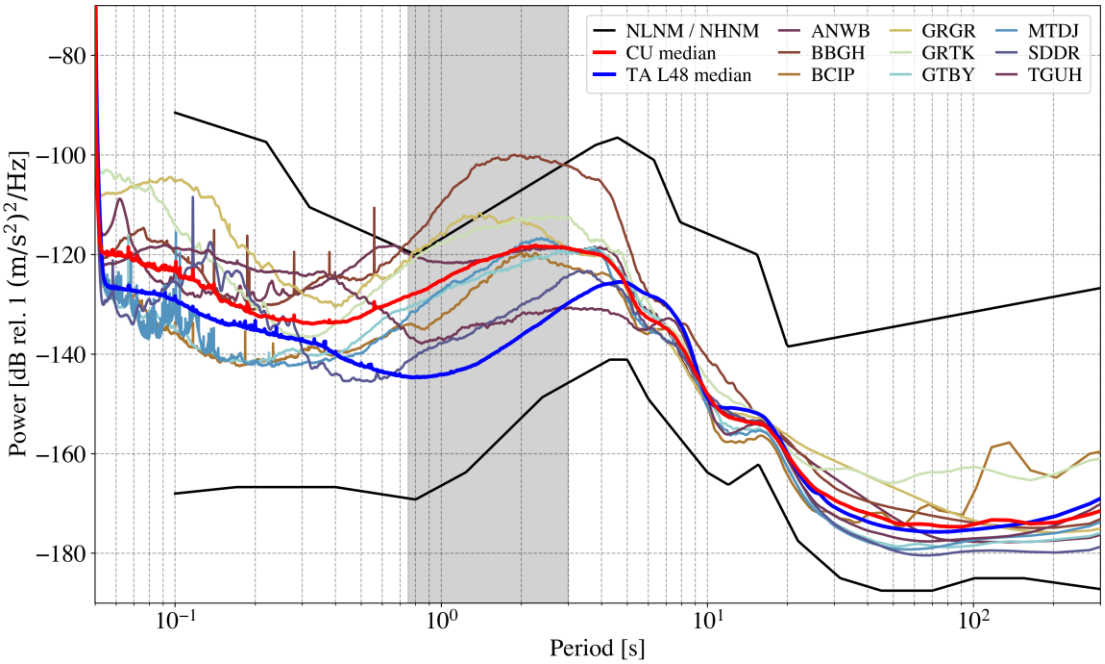

Figure 3. Median station and network PSD estimates. The Peterson (1993) New Low-/High-Noise Models (NLNM/NHNM) are shown as black lines and median power for the entire CU, TA L48 networks are show as bold red and blue lines respectively. Individual CU stations are shown as thin lines in a range of colors shown in legend. Transparent gray region shows 0.75-3 s range.

3.5 Discussion

Cultural activity can influence background noise levels in a variety of ways (Schippkus et al., 2020) and may best explain the notable high frequency signals on CU

stations MTDJ, SDDR, and TGUH. Station MTDJ is located at a radar facility and activity associated with operations at the site are likely contributing to observed high frequency signals. Station TGUH is located on the outskirts of Tegucigalpa, a city with a population of 1.3 million. We interpret the wide distribution of power at high frequencies to arise from diverse, metropolitan specific, cultural activity that likely experiences large diurnal variations as seen in the PSDs through time (Figure S2 in Appendix 3.A). Lastly, station SDDR is located at a dam and water utility plant. Operations associated with this facility are also likely contributing to the distinct high frequency signal here. Release and restriction of water through the dam may correspond to higher and lower power levels within the signal respectively. This pattern can be seen when looking at the PSDs through time and is punctuated by sharp changes in power within the signal (Figure S3 in Appendix 3.A). Overall, CU stations maintain a high level of short period noise independent of known anomalous cultural sources as demonstrated when comparing the CU and TA median (Figure 3). In fact, stations with no easily identifiable cultural noise sources can have higher noise levels than those with known cultural sources (i.e., MTDJ, SDDR, and TGUH; Figure 3) demonstrating the important role environmental factors such as wind and the lithology the seismic station is emplaced in (Anthony et al., 2022) might play in noise levels at short periods (Rindraharisaona et al., 2023).

Within the primary and secondary microseism band both individual CU station power and CU and TA L48 network median power demonstrate general consistency and less variability, relative to the rest of the spectrum. This is perhaps to be expected considering the primary and secondary microseism band are excited globally within

oceans and therefore share similarity in their records and character over long periods of time (Bensen et al., 2008 fig. 10).

The most discernable signal at long periods occurs in the form of similarly elevated power at stations BCIP and GRTK (Figure 2, 3). This elevated power has been previously documented at station BCIP located along the Panama Canal and was attributed to cargo ship or wind-lake driven seiching (McNamara et al., 2011). Station GRTK is located on Grand Turk which is a very small island but is situated proximal to an expansive, somewhat sheltered, and shallow bay (Figure 1) with potential to generate wind-driven seiching (Stevens & Lawrence, 1997). Since windspeeds fluctuate seasonally in the Caribbean we might expect a seasonal pattern in seiching as well which could explain the wide range of power demonstrated in the PSD for GRTK and seasonality in PSDs through time at long periods (Figure S4 in Appendix 3.A).

The rest of the discussion is focused on one of the most prominent patterns within CU PSDs, systematic elevated power levels in the 0.75–3 s period band. Examination of the TA L48 PSDs in the same period band reveals a relationship between power and proximity to coastline (Figure 4). The median power of all L48 stations within 50 km of the beach is similarly elevated in the 0.75–3 s period band, in agreement with observations from CU stations, and reflects similar shape and character as the CU median power curve (Figure 4). This pattern and character is not seen on the median from the subset of stations > 50 km from the coastline.

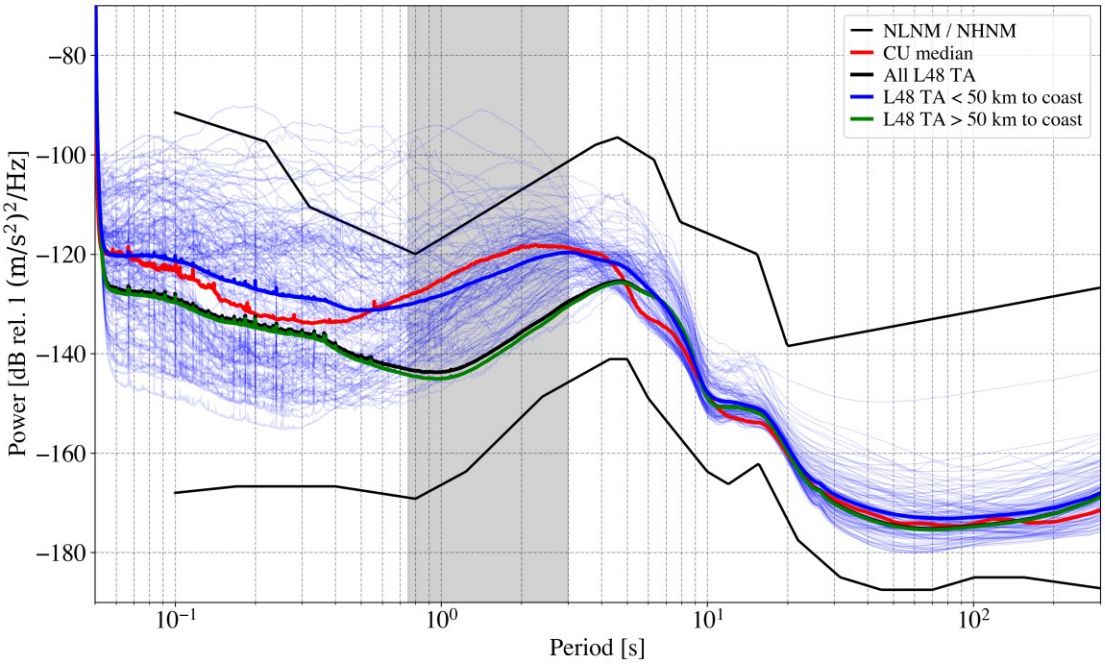

Figure 4. Median network power of the CU and TA L48 and median power of TA L48 stations whose distance to beach is within and over 50 km. The Peterson (1993) New Low-/High-Noise Model (NLNM/NHNM) are shown as black lines. Median CU network power is shown as a thick red line. Median power of all TA L48 stations is shown as a thick black line while the median power of stations within and over 50 km are shown as thick blue and green lines respectively. Thin blue lines show median power level of each station within 50 km to beach that compose the thick blue median curve. Transparent gray region shows 0.75-3 s range.

The power levels in this 0.75–3 s band also appear to decay as a function of proximity to coastline on the L48 and CU stations (Figure 5, 6). This decay is not present in the 4–8 s band that is more representative of the secondary microseism (Figure 5).

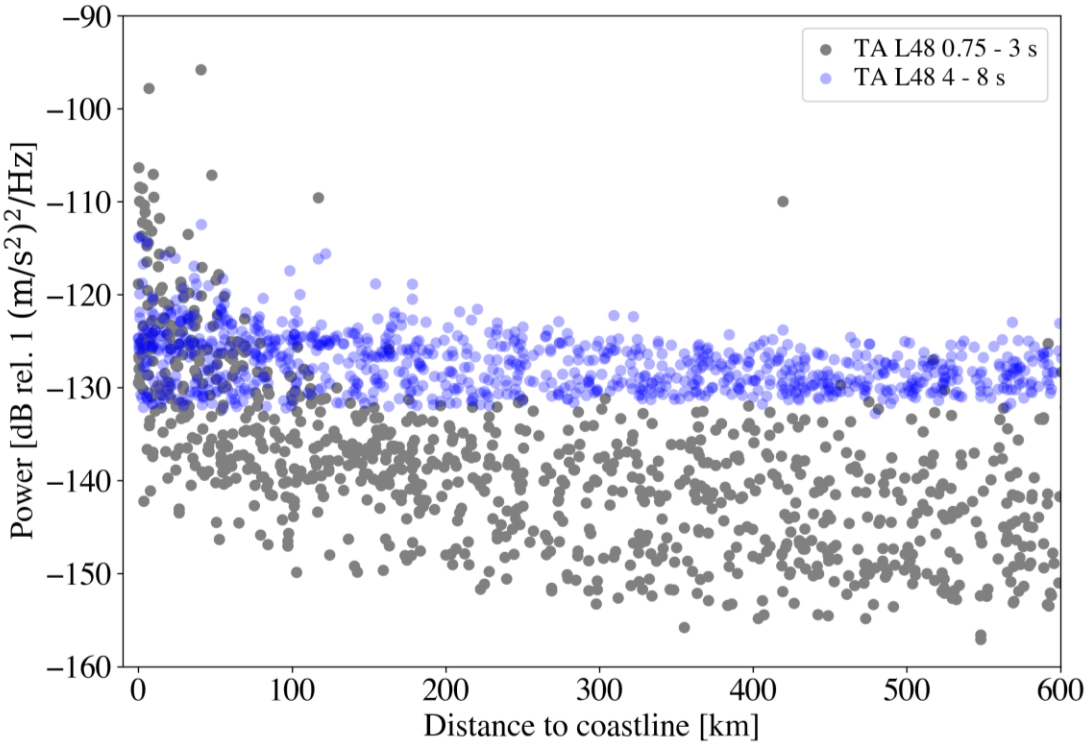

Figure 5. Observed power as a function of distance for two different periods bands on the L48. Gray dots show mean 0.75-3 s power from each TA L48 station median power curve. Transparent blue dots show mean 4-8 s power from each TA L48 station median power curve.

We found the observed decay could be described with simple Rayleigh wave attenuation from a point source using equation (1):

$$A(x) = A_0^{\left(-\frac{\omega x}{2cQ}\right)}\left(\frac{1}{\sqrt{x}}\right)$$

Where *A* is amplitude, x is distance from the point source, ω is angular frequency, *c* is velocity, and Q is the quality factor, which is the ratio of the energy stored over energy dissipated per cycle. The end term, $1/\sqrt{x}$, describes geometric spreading of a circularly propagating surface wave. Upon testing a range of possible values for Q (Magrini et al., 2021) it becomes apparent that geometric spreading accounts for a large component of the decay at short distances while intrinsic attenuation controls the slope of the decay playing a larger role at longer distances (Figure 6). Note that to compare PSDs that are in

units of $(m/s^2)^2/Hz$ we apply a 1-octave integration after removing the density scaling of 1/Hz. The amplitude (A_0) serves as the coastal boundary condition. We use a starting acceleration amplitude (A_0) of ~38.75 μ m/s^2 which converts to ~ –84 dB (rel. 1 $m/s^2)^2/Hz$ and is comparable to conditions found by Poppeliers and Mallinson, (2015) during a nominal storm (~ –100 dB) once converted to PSD in terms of acceleration, ~ –89.5 dB (rel. 1 $m/s^2)^2/Hz$. Application of this model to all CU and TA L48 stations adopting, a Q value of 2000, a velocity of 1.5 km/s and a 1.875 s Rayleigh wave (middle of the range) generally fit the observations well near the coastlines of the contiguous US (Figure 7). Predicted power from the model also provides reasonable fits to the observations in much of the intermountain west, the east coast of the US, as well as most stations within the CU network.

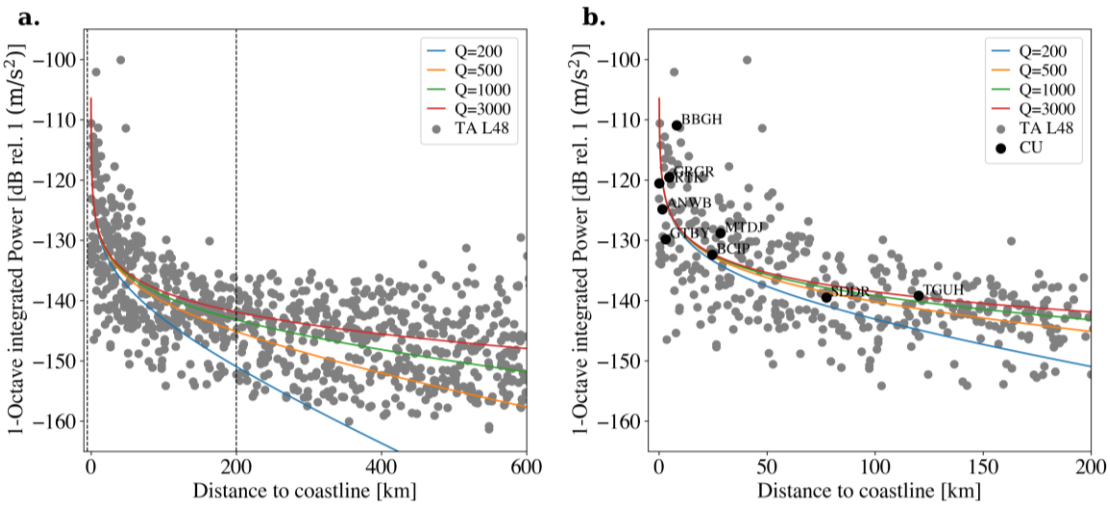

Figure 6. Observed power in the 0.75-3 s range as a function of distance plotted against a simple surface wave power decay model. a) gray dots show mean 0.75-3 s power from each TA L48 station median power curve. Decay curves are shown as colored lines corresponding to Q value used in the model. Black dashed lines show distance extent plotted in panel b. b) same as a, but includes median 0.75-3 s power from each CU station median power curve (black dots), and zoomed in to show detail. CU stations are labeled. Since CU distances were measured manually, we measured to nearest beach rather strictly adhering to coastline. We did this to avoid sheltered bays and inlets where beach

energy is subdued such as the Gulf of Fonseca near TGUH, and Guantanamo Bay near GTBY.

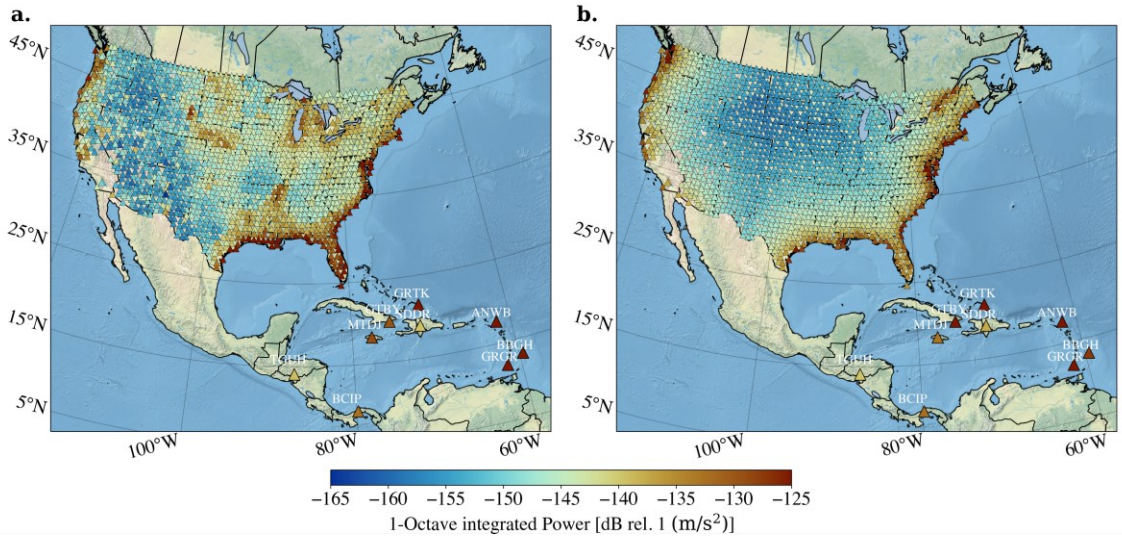

Figure 7. Maps showing observed and predicted power levels of the TA and CU networks. a) observed 0.75-3 s average station power. b) predicted power decay from a simple surface wave power decay model, eq. (1).

However, noise levels in some regions do not fit the model well. Examining residual power (observations-predictions), reveals large positive (under-prediction) discrepancies (> 15 dB) surrounding the Great Lakes shoreline, the Mississippi Embayment, stations furthest away from the coastline within the continental interior (within and south of the Williston Basin), and station BBGH in the CU network (Figure 8). High power levels in similar period bands have been previously identified within these L48 regions and have been attributed to differences in local geology, for the Mississippi embayment and Williston basin, (Koper & Burlacu, 2015; Anthony et al., 2022) and the generation of lake microseism energy for the region surrounding the great lakes shoreline (Xu et al., 2017; Anthony et al., 2018). To first order, our results agree with the results and interpretations of these previous studies. Large power residuals identify locations where local geology and differences in Q might have an outside influence on power levels, such as the

Williston Basin and Mississippi Embayment. However, it is important to note that certain basin geometries can drive frequency dependent surface wave amplification leading to local variability in Q sensitivity (Bowden and Tsai, 2017; Koper and Burlacu, 2018; Diaz et al., 2023b).

Local geology and differences in Q could also explain anomalously elevated power at BBGH, which is a coral island with marine strata dominated surface geology, relative to stations ANWB and GRGR, which are both volcanic islands dominated by volcanic surface geology (Figure 8; French & Schenk, 2004). But the ability for residual power from our model to identify locations where local geology might play a large role in power level diminishes with increasing station-to-coastline distance. This is because the largest station-to-coastline distances are within the continental interior where multiple coastlines at similar distances would likely be contributing to the observed power. Our simple single point source model should therefore be expected to underpredict power and thus create large positive power residuals (Figure 6a). The low predicted power, ∼ -150 dB, and high residual power, > 15 dB, in much of Nebraska (south of Williston Basin) may be an example of this scenario and could therefore be a non-physical artifact from a model shortcoming (Figure 7, 8). It should be noted that such low power near the NLNM in the 0.75-3 s band is observed at GSN station MAKZ (Makanchi, Kazakhstan) and AAK (Ala Archa, Kyrgyzstan). Both stations are located near the center of the Asian continent and have very large (> 2000 km) station-to-coastline distances in nearly all directions where significant power decay, up to -35 dB, is observed at short periods (Li et al., 2022). In any case the model presented here appears most relevant near the coast (Figure 6, 7).

It has been demonstrated that local geology can heavily influence background noise levels around the period band 0.75-3s (Anthony et al., 2022; Rindraharisaona et al., 2022; Smith et al., 2023. However, variations in the nearshore source power can also significantly influence observed power levels in the 0.75-3 s period range (Gutenberg, 1958; Bromirski et al., 2005; Anthony et al., 2018; Baker et al., 2019). The period range of the anomalously elevated power observed on the CU stations and those L48 stations nearest the coast, ~0.75-3 s, is below typical distant ocean generated secondary microseism peaks and is more indicative of nearshore generated energy (Bromirski et al., 2005; Koper & Burlacu, 2015). Koper and Burlacu (2015) found local geology to be more important than proximity to coastline in generating high power levels observed on the TA L48 stations. However, the model presented here suggests that at 0.75-3 s, power levels at stations closest to the beach are more influenced by proximity to coastline. This may be because at 0.75-3 s, power from nearshore wave action and microseism can be more energetic on stations near the coast (Bromirski et al., 2005; Ardhuin et al., 2011; Anthony et al., 2018;). This is further demonstrated by the lack of power decay in the 4–8 s band (Figure 5). Application of this model to the Great Lakes region would be an extension of this reasoning and would serve to provide better fits to the observations and decrease the high residual power for that region in our map (Figure 8). However, the power of the starting amplitude (A_0) would likely be lower than –84 dB (Figure 7). Fitting the model to regionally subset data could help characterize variations in apparent source power associated with different regions (e.g., Great Lakes, east coast US, west coast US, GSN

island sites) and time periods, due to storm activity (Gutenberg, 1958; Sufri et al., 2014; Poppeliers & Mallinson, 2015).

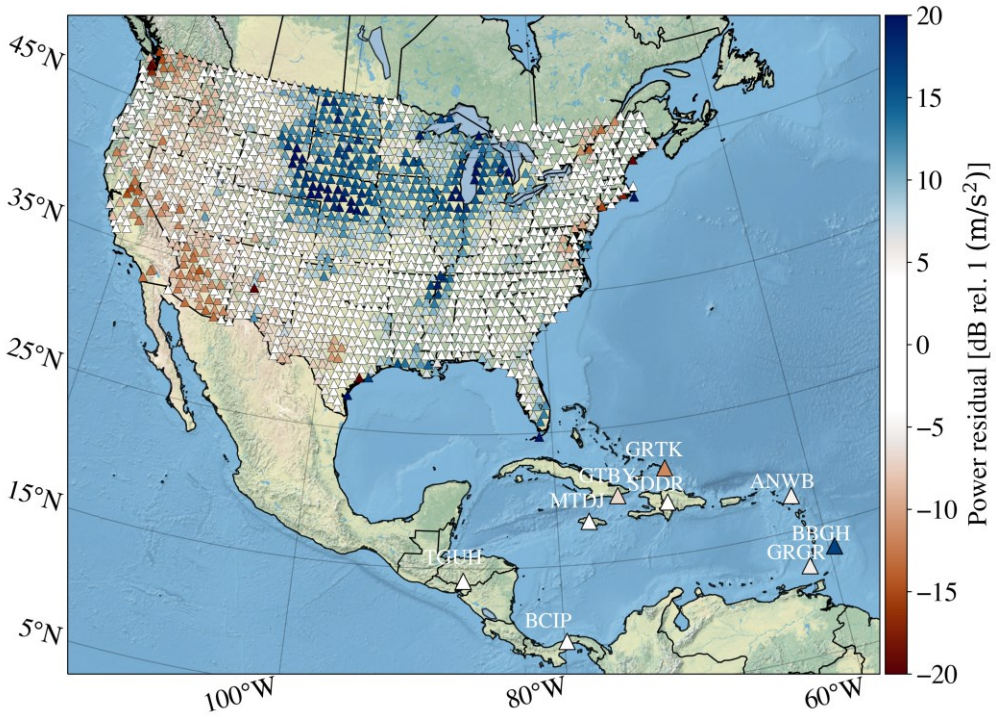

Figure 8. Map showing difference in power between observations and predictions shown in Figure 6.

Regardless of source, the empirically observed decay provides valuable information on the relationship with distance. The 0.75–3 s period range is important for teleseismic event detection, so reducing unnecessary elevated power in this range is of interest. Our model provides quantitative predictions of power decay at a given distance from coastline and indicates that a power reduction of 25 dB can be achieved by simply installing the seismometer 25 km from the coastline. This result could serve informative for island sites which play a critical role in global monitoring and detection efforts but

often display pervasively elevated background noise levels (Peterson et al., 1993; Ringler et al., 2023).

Exact spectral peaks of the supposed nearshore energy remain unknown and will depend on location and mechanics of the source. Work toward an objective approach to determine an accurate choice in period range could serve useful but may be complicated by non-systematic overlap of multiple sources with unknown spectral peaks. Observations of elevated network and station median power signals that approach and sometimes exceed the NHNM informed our focus on the 0.75–3 s band here. However, the relationship between power levels and station proximity to coastline may also hold true for shorter period energy. A dense (< 1 km) transect of stations orthogonal to the coast with a high sampling rate could serve useful to further investigate this relationship at shorter periods and capture high frequency energy that may otherwise decay too rapidly to be detected by large TA interstation distances. A global survey across GSN stations to explore the extent to which this relationship could explain elevated background noise levels at island sites could also be an informative avenue of research. Such studies could prove useful in determining the extent to which power levels in the 0.75–3 s band (and potentially shorter) could impede local and teleseismic event detection and could serve to verify and refine the model we present here.

3.6 Conclusion

We calculated PSDs to determine background noise levels of the CU network in the Caribbean and described the most discernable first order signals observed within 0.05–300 s range. Power levels in the 0.75–3 s band are systematically elevated on the CU stations as well as L48 stations near the coastline and appear to decay as a function of proximity to coastline. This empirically derived relationship is well modeled with a simple surface wave amplitude decay with geometric spreading being the most important factor at stations near the coast (< ~50 km). This rudimentary model provides predictions of power decay with distance from coastline and indicates that a power reduction of ~25 dB can be achieved by simply installing the seismometer 25 km away from the coastline. This finding may help to inform future site locations and array design thereby improving network performance and data quality.

3.7 Data and Resources

All seismic data used in this study is available at the IRIS Data Management Center under network codes CU and TA. All scripts used for making figures in this paper are freely available at: https://github.com/jwilgus/Caribbean_noise_SRL. We relied heavily on the Python library ObsPy (Megies et al., 2011). The associated supplemental material includes figures that show the small footprint vault installation style of many CU stations and power spectral density through time for stations TGUH, SDDR, and GRTK.

The facilities of IRIS Data Services, and specifically the IRIS Data Management Center, were used for access to waveforms, related metadata, and/or derived products

used in this study. IRIS Data Services are funded through the Seismological Facilities for the Advancement of Geoscience and EarthScope (SAGE) Proposal of the National Science Foundation under Cooperative Agreement EAR-1261681.

Global Seismographic Network (GSN) is a cooperative scientific facility operated jointly by the Incorporated Research Institutions for Seismology (IRIS), the United States Geological Survey (USGS), and the National Science Foundation (NSF), under Cooperative Agreement EAR-1261681.

Any use of trade, product, or firm names is for descriptive purposes only and does not imply endorsement by the U.S. Government.

3.8 Acknowledgements

We thank ASL field technicians and local affiliates responsible for deployment and maintenance of the CU network. This work benefited from discussions with Tyler Storm.

References

Albuquerque Seismological Laboratory/U.S. Geological Survey (2006). Caribbean Network, International Federation of Digital Seismograph Networks. https://doi.org/10.7914/SN/CU

Anthony, R. E., Ringler, A. T., & Wilson, D. C. (2018). The widespread influence of Great Lakes microseisms across the midwestern United States revealed by the 2014 polar vortex. Geophysical Research Letters, 45(8), 3436-3444. https://doi.org/10.1002/2017GL076690

Anthony, R. E., Ringler, A. T., Wilson, D. C., & Wolin, E. (2019). Do low-cost seismographs perform well enough for your network? An overview of laboratory tests and field observations of the OSOP Raspberry Shake 4D. Seismological Research Letters, 90(1), 219-228. https://doi.org/10.1785/0220180251

Anthony, R. E., Ringler, A. T., Wilson, D. C., Bahavar, M., & Koper, K. D. (2020). How processing methodologies can distort and bias power spectral density estimates of seismic background noise. Seismological Research Letters, 91(3), 1694-1706. https://doi.org/10.1785/0220190212

Anthony, R. E., Ringler, A. T., & Wilson, D. C. (2022). Seismic background noise levels across the Continental United States from USArray transportable array: The influence of geology and geography. Bulletin of the Seismological Society of America, 112(2), 646-668. https://doi.org/10.1785/0120210176

Ardhuin, F., Gualtieri, L., & Stutzmann, E. (2015). How ocean waves rock the Earth: Two mechanisms explain microseisms with periods 3 to 300 s. Geophysical Research Letters, 42(3), 765-772. https://doi.org/10.1002/2014GL062782

Ardhuin, F., Stutzmann, E., Schimmel, M., & Mangeney, A. (2011). Ocean wave sources of seismic noise. Journal of Geophysical Research: Oceans, 116(C9). https://doi.org/10.1029/2011JC006952

Baker, M. G., Aster, R. C., Anthony, R. E., Chaput, J., Wiens, D. A., Nyblade, A., ... & Stephen, R. A. (2019). Seasonal and spatial variations in the ocean-coupled ambient wavefield of the Ross Ice Shelf. Journal of Glaciology, 65(254), 912-925. https://doi.org/10.1017/jog.2019.64

Benz, H. M., & Herrmann, R. B. (2014). Rapid estimates of the source time function and M w using empirical Green's function deconvolution. Bulletin of the Seismological Society of America, 104(4), 1812-1819. https://doi.org/10.1785/0120130325

Bowden, D. C., & Tsai, V. C. (2017). Earthquake ground motion amplification for surface waves. Geophysical Research Letters, 44(1), 121-127. https://doi.org/10.1002/2016GL071885

Bormann, P., Wendt, S., & DiGiacomo, D. (2013). Seismic sources and source parameters. In New Manual of Seismological Observatory Practice 2 (NMSOP2) (pp. 1-259). Deutsches GeoForschungsZentrum GFZ. https://doi.org/10.2312/GFZ.NMSOP-2_ch3

Braszus, B., Goes, S., Allen, R., Rietbrock, A., Collier, J., Harmon, N., ... & Wilson, M. (2021). Subduction history of the Caribbean from upper-mantle seismic imaging and plate

reconstruction. Nature communications, 12(1), 4211. https://doi.org/10.1038/s41467-021-24413-0

Bromirski, P. D., Duennebier, F. K., & Stephen, R. A. (2005). Mid-ocean microseisms. Geochemistry, Geophysics, Geosystems, 6(4). https://doi.org/10.1029/2004GC000768

Busby R. W. Woodward R. L. Hafner K. A. Vernon F. L., and Frassetto A. M. (2018). The Design and Implementation of EarthScope's USArray Transportable Array in the Conterminous United States and Southern Canada, doi: https://doi.org/10.5281/zenodo.3758247.

Busby, R. W., and K. Aderhold (2020). The Alaska Transportable Array: As built, Seismological Research Letters, 91, 6, 3017-3027. https://doi.org/10.1785/0220200154

Cordrie, L., Feuillet, N., Gailler, A., Biguenet, M., Chaumillon, E., & Sabatier, P. (2022). A Megathrust earthquake as source of a Pre-Colombian tsunami in Lesser Antilles: Insight from sediment deposits and tsunami modeling. Earth-Science Reviews, 228, 104018. https://doi.org/10.1016/j.earscirev.2022.104018

DesRoches, R., Comerio, M., Eberhard, M., Mooney, W., Rix, G., J. Overview of the 2010 Haiti Earthquake. Earthquake Spectra. 2011;27(1_suppl1):1-21. https://doi.org/10.1193/1.3630129

Diaz, J., Ruiz, M., Udina, M., Polls, F., Martí, D., & Bech, J. (2023a). Monitoring storm evolution using a high-density seismic network. Scientific Reports, 13(1), 1853. https://www.nature.com/articles/s41598-023-28902-8

Díaz, J., Ventosa, S., Schimmel, M., Ruiz, M., Macau, A., Gabàs, A., ... & Vergés, J. (2023b). Mapping the basement of the Cerdanya Basin (eastern Pyrenees) using seismic ambient noise. Solid Earth, 14(5), 499-514. https://se.copernicus.org/articles/14/499/2023

Doody, C. D., Ringler, A. T., Anthony, R. E., Wilson, D. C., Holland, A. A., Hutt, C. R., & Sandoval, L. D. (2018). Effects of Thermal Variability on Broadband Seismometers: Controlled Experiments, Observations, and Implications. Bulletin of the Seismological Society of America, 108(1), 493-502. https://doi.org/10.1785/0120170233

Dybing, S. N., Ringler, A. T., Wilson, D. C., & Anthony, R. E. (2019). Characteristics and Spatial Variability of Wind Noise on Near-Surface Broadband Seismometer. Bulletin of the Seismological Society of America, 109(3), 1082-1098. https://doi.org/10.1785/0120180227

Dziewonski, A. M., & Gilbert, F. (1971). Solidity of the inner core of the Earth inferred from normal mode observations. Nature, 234(5330), 465-466. https://doi.org/10.1038/234465a0

Fan, W., McGuire, J. J., de Groot-Hedlin, C. D., Hedlin, M. A., Coats, S., & Fiedler, J. W. (2019). Stormquakes. Geophysical Research Letters, 46(22), 12909-12918. https://doi.org/10.1029/2019GL084217

French, C. D., & Schenk, C. J. (2004). Map showing geology, oil and gas fields, and geologic provinces of the Caribbean region (No. 97-470-K). US Geological Survey. https://doi.org/10.3133/ofr97470K

Gualtieri, L., Bachmann, E., Simons, F. J., & Tromp, J. (2020). The origin of secondary microseism Love waves. Proceedings of the National Academy of Sciences, 117(47), 29504-29511. https://doi.org/10.1073/pnas.2013806117

Gutenberg, B. (1936). On microseisms. Bulletin of the Seismological Society of America, 26(2), 111-117. https://doi.org/10.1785/BSSA0260020111

Gutenberg, B. (1958). Microseisms. In Advances in geophysics (Vol. 5, pp. 53-92). Elsevier. https://doi.org/10.1016/S0065-2687(08)60075-8

Holcomb, L. G. (1998). Spectral structure in the Earth's microseismic background between 20 and 40 seconds. Bulletin of the Seismological Society of America, 88(3), 744-757. https://doi.org/10.1785/BSSA0880030744

IRIS Transportable Array (2003). USArray Transportable Array, International Federation of Digital Seismograph Networks. https://doi.org/107914/SN/TA

Janiszewski, H. A., Eilon, Z., Russell, J. B., Brunsvik, B., Gaherty, J. B., Mosher, S. G., ... & Coats, S. (2023). Broad-band ocean bottom seismometer noise properties. Geophysical Journal International, 233(1), 297-315. https://doi.org/10.1093/gji/ggac450

Kedar, S., Longuet-Higgins, M., Webb, F., Graham, N., Clayton, R., & Jones, C. (2008). The origin of deep ocean microseisms in the North Atlantic Ocean. Proceedings of the Royal Society A: Mathematical, Physical and Engineering Sciences, 464(2091), 777-793. https://doi.org/10.1098/rspa.2007.0277

Koper, K. D., & Burlacu, R. (2015). The fine structure of double-frequency microseisms recorded by seismometers in North America. Journal of Geophysical Research: Solid Earth, 120(3), 1677-1691. https://doi.org/10.1002/2014JB011820

Le Pape, F., Craig, D., & Bean, C. J. (2021). How deep ocean-land coupling controls the generation of secondary microseism Love waves. Nature Communications, 12(1), 2332. https://doi.org/10.1038/s41467-021-22591-5

Lecocq, T., Hicks, S. P., Van Noten, K., Van Wijk, K., Koelemeijer, P., De Plaen, R. S., ... & Xiao, H. (2020). Global quieting of high-frequency seismic noise due to COVID-19 pandemic lockdown measures. Science, 369(6509), 1338-1343. https://doi.org/10.1126/science.abd2438

Li, X., Xu, Y., Xie, C., & Sun, S. (2022). Global characteristics of ambient seismic noise. Journal of Seismology, 26(2), 343-358. https://doi.org/10.1007/s10950-021-10071-8

Lin, F. C., Moschetti, M. P., & Ritzwoller, M. H. (2008). Surface wave tomography of the western United States from ambient seismic noise: Rayleigh and Love wave phase velocity maps. Geophysical Journal International, 173(1), 281-298. https://doi.org/10.1111/j.1365-246X.2008.03720.x

Longuet-Higgins, M. (1950). A theory of the origin of microseisms, Philosophical Transactions of the Royal Society of London – Series A: Mathematical and Physical Sciences, 243, 857, 1–35. https://doi.org/10.1098/rsta.1950.0012

Magrini, F., Boschi, L., Gualtieri, L., Lekić, V., & Cammarano, F. (2021). Rayleigh-wave attenuation across the conterminous United States in the microseism frequency band. Scientific reports, 11(1), 10149. https://doi.org/10.1038/s41598-021-89497-6

Marcillo, O. E., & Carmichael, J. (2018). The detection of wind-turbine noise in seismic records. Seismological Research Letters, 89(5), 1826-1837. https://doi.org/10.1785/0220170271

Maurya, S., Taira, T. A., & Romanowicz, B. (2019). Location of seismic "hum" sources following storms in the north pacific ocean. Geochemistry, Geophysics, Geosystems, 20(3), 1454-1467. https://doi.org/10.1029/2018GC008112

McCann, W. R. (1985). On the earthquake hazards of Puerto Rico and the Virgin Islands. Bulletin of the Seismological Society of America, 75(1), 251-262. https://doi.org/10.1785/BSSA0750010251

McNamara, D. E., & Buland, R. P. (2004). Ambient noise levels in the continental United States. Bulletin of the seismological society of America, 94(4), 1517-1527. https://doi.org/10.1785/012003001

McNamara, D., McCarthy, J., & Benz, H. (2006). Improving earthquake and tsunami warnings for the Caribbean Sea, the Gulf of Mexico, and the Atlantic coast (No. 2006-3012). https://doi.org/10.3133/fs20063012

McNamara, D. E., Ringler, A. T., Hutt, C. R., & Gee, L. S. (2011). Seismically observed seiching in the Panama Canal. Journal of Geophysical Research: Solid Earth, 116(B4). https://doi.org/10.1029/2010JB007930

McNamara, D. E., von Hillebrandt-Andrade, C., Saurel, J. M., Huerfano, V., & Lynch, L. (2016). Quantifying 10 years of improved earthquake-monitoring performance in the Caribbean region. Seismological Research Letters, 87(1), 26-36. https://doi.org/10.1785/0220150095

Megies, T., Beyreuther, M., Barsch, R., Krischer, L., & Wassermann, J. (2011). ObsPy–What can it do for data centers and observatories? Annals of Geophysics, 54(1), 47-58. https://doi.org/10.4401/ag-4838

Meltzer, A., Rudnick, R., Zeitler, P., Levander, A., Humphreys, G., Karlstrom, K., ... & van der Hilst, R. D. (1999). The USArray initiative. Geological Society of America Today, 9, 8-10. https://dspace.library.uu.nl/handle/1874/7578

Moschetti, M. P., Ritzwoller, M. H., & Shapiro, N. M. (2007). Surface wave tomography of the western United States from ambient seismic noise: Rayleigh wave group velocity maps. Geochemistry, Geophysics, Geosystems, 8(8). https://doi.org/10.1029/2007GC001655

Peterson, J. (1993). Observations and modeling of seismic background noise (Vol. 93, pp. 1-95). Reston, VA, USA: US Geological Survey. https://doi.org/10.3133/ofr93322

Poppeliers, C., & Mallinson, D. (2015). High-frequency seismic noise generated from breaking shallow water ocean waves and the link to time-variable sea states. Geophysical Research Letters, 42(20), 8563-8569. https://doi.org/10.1002/2015GL066126

Rhie, J., & Romanowicz, B. (2004). Excitation of Earth's continuous free oscillations by atmosphere–ocean–seafloor coupling. Nature, 431(7008), 552-556. https://doi.org/10.1038/nature02942.

Rindraharisaona, E. J., Réchou, A., Fontaine, F. R., Barruol, G., Stamenoff, P., Boudevillain, B., ... & Delcher, E. (2022). Seismic signature of rain and wind inferred from seismic

data. Earth and Space Science, 9(10), e2022EA002328. https://doi.org/10.1029/2022EA002328

Ringler, A. T., Steim, J., Wilson, D. C., Widmer-Schnidrig, R., & Anthony, R. E. (2020a). Improvements in seismic resolution and current limitations in the Global Seismographic Network. Geophysical Journal International, 220(1), 508-521. https://doi.org/10.1093/gji/ggz473

Ringler, A. T., Anthony, R. E., Wilson, D. C., Claycomb, A. C., & Spritzer, J. (2020b). Magnetic field variations in Alaska: Recording space weather events on seismic stations in Alaska. Bulletin of the Seismological Society of America, 110(5), 2530-2540. https://doi.org/10.1785/0120200019

Ringler, A.T., Anthony, R.E., Aderhold, K., Busby, R.W., Frassetto, A., Tanimoto T., Wilson D.C. (2023). Perspectives on Transportable Array Alaska Background Noise Levels, in press.

Ringler, A. T., Anthony, R. E., Aster, R. C., Ammon, C. J., Arrowsmith, S., Benz, H., ... & Yeck, W. (2022). Achievements and prospects of global broadband seismographic networks after 30 years of continuous geophysical observations. Reviews of Geophysics (1985), 60(3). https://doi.org/10.1029/2021rg000749

Robson, A. J., & Romanowicz, B. (2019). New normal mode constraints on bulk inner core velocities and density. Physics of the Earth and Planetary Interiors, 295, 106310. https://doi.org/10.1016/j.pepi.2019.106310

Sabra, K. G., Gerstoft, P., Roux, P., Kuperman, W. A., & Fehler, M. C. (2005). Extracting time-domain Green's function estimates from ambient seismic noise. Geophysical research letters, 32(3). https://doi.org/10.1029/2004GL021862

Schippkus, S., Garden, M., & Bokelmann, G. (2020). Characteristics of the ambient seismic field on a large-N seismic array in the Vienna basin. Seismological Society of America, 91(5), 2803-2816. https://doi.org/10.1785/0220200153

Shapiro, N. M., Ritzwoller, M. H., & Bensen, G. D. (2006). Source location of the 26 sec microseism from cross-correlations of ambient seismic noise. Geophysical research letters, 33(18). https://doi.org/10.1029/2006GL027010

Shedlock, K. M. (1999). Seismic hazard map of North and Central America and the Caribbean. https://doi.org/10.4401/ag-3786

Smith, K., & Tape, C. (2019). Seismic noise in central Alaska and influences from rivers, wind, and sedimentary basins. Journal of Geophysical Research: Solid Earth, 124(11), 11678-11704. https://doi.org/10.1029/2019JB017695

Smith, K., Tape, C., & Tsai, V. C. (2023). Seismic response of Nenana sedimentary basin, central Alaska. Bulletin of the Seismological Society of America, 113(2), 762-781. https://doi.org/10.1785/0120220160

Steim J. M. (2015). Theory and observations-Instrumentation for global and regional seismology, in Treatise on Geophysics , Second Ed., Schubert G. (Editor), Elsevier, Oxford, United Kingdom, 29–78.

Stevens, C. L., & Lawrence, G. A. (1997). Estimation of wind-forced internal seiche amplitudes in lakes and reservoirs, with data from British Columbia, Canada. Aquatic Sciences, 59, 115-134. https://doi.org/10.1007/BF02523176

Sufri, O., Koper, K. D., Burlacu, R., & de Foy, B. (2014). Microseisms from superstorm Sandy. Earth and Planetary Science Letters, 402, 324-336. https://doi.org/10.1016/j.epsl.2013.10.015

Tsai, V. C., & McNamara, D. E. (2011). Quantifying the influence of sea ice on ocean microseism using observations from the Bering Sea, Alaska. Geophysical Research Letters, 38(22). https://doi.org/10.1029/2011GL049791

Torpey Zimmerman, M., Shen-Tu, B., Shabestari, K., & Mahdyiar, M. (2022). A comprehensive hazard assessment of the Caribbean Region. Bulletin of the Seismological Society of America, 112(2), 1120-1148. https://doi.org/10.1785/0120210157

Wang, R., Schmandt, B., Zhang, M., Glasgow, M., Kiser, E., Rysanek, S., & Stairs, R. (2020). Injection-induced earthquakes on complex fault zones of the Raton Basin illuminated by machine-learning phase picker and dense nodal array. Geophysical Research Letters, 47(14), e2020GL088168. https://doi.org/10.1029/2020GL088168

Webb, S. C. (2008). The Earth's hum: the excitation of Earth normal modes by ocean waves. Geophysical Journal International, 174(2), 542-566. https://doi.org/10.1111/j.1365-246X.2008.03801.x

Welch, P. D. (1967). The use of fast Fourier transform for the estimation of power spectra: A method based on time averaging over short, modified Periodograms, *IEEE Transactions on Audio and Electroacoustics*, **AU-15**, 70-73. https://doi.org/10.1109/TAU.1967.1161901

Wilson, D. C, E. Wolin, W. L. Yeck, R. E. Anthony, and A. T. Ringler (2021). Modeling seismic network detection thresholds using production picking algorithms, Seismological Research Letters, 93, 1, 149-160, DOI:10.1785/0220210192. https://doi.org/10.1785/0220210192

Xu, Y., Koper, K. D., & Burlacu, R. (2017). Lakes as a source of short-period (0.5–2 s) microseisms. Journal of Geophysical Research: Solid Earth, 122(10), 8241-8256. https://doi.org/10.1002/2017JB014808

Appendix

3.A Supplementary figures

Figure S1. Photographs of station ANWB showing small footprint vault installation style.

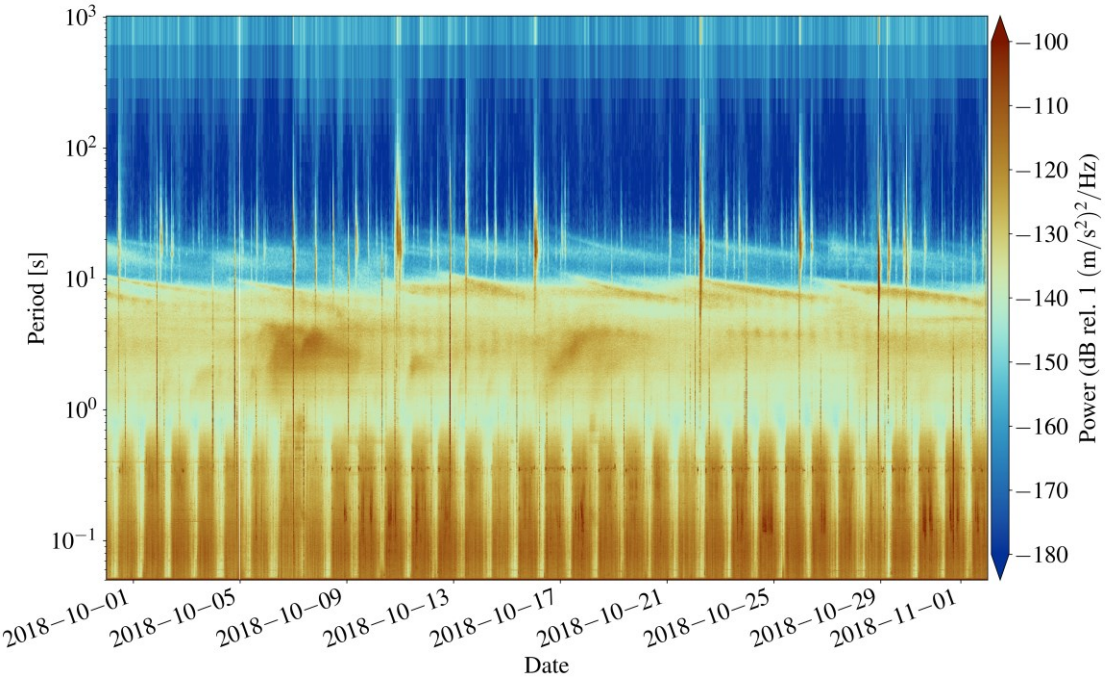

Figure S2. Power spectral density for ~1 month of time in 2018 for station TGUH.

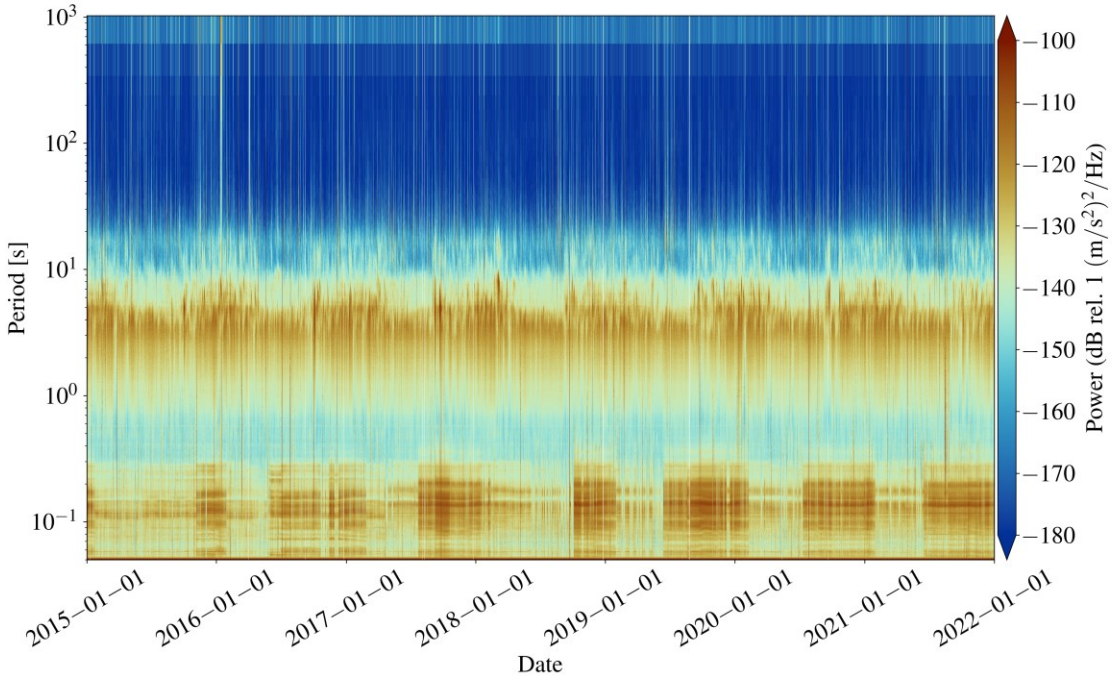

Figure S3. Power spectral density over a span of 7 years for station SDDR.

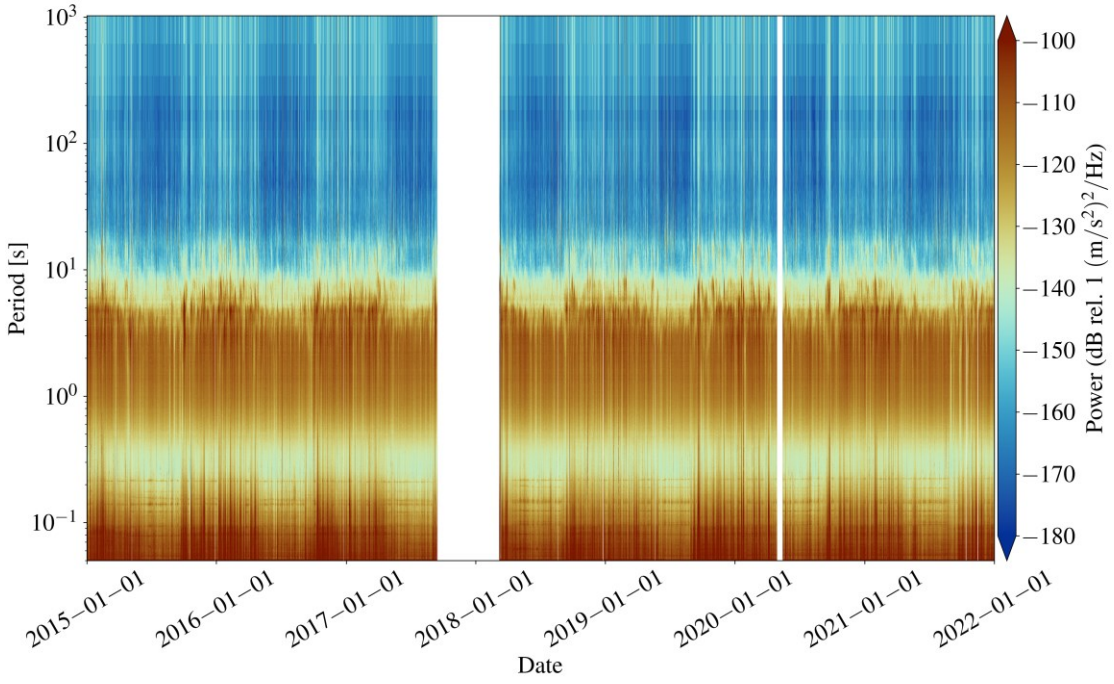

Figure S4. Power spectral density over a span of 7 years for station GRTK.